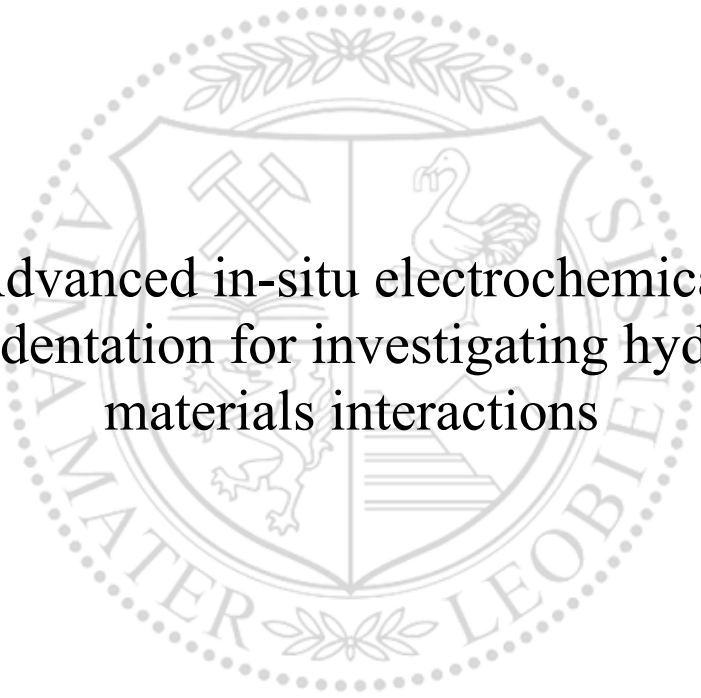




Chair of Physical Metallurgy and Metallic Materials

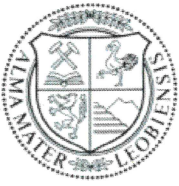
Doctoral Thesis



Advanced in-situ electrochemical
nanoindentation for investigating hydrogen-
materials interactions

Dipl.-Ing. Anna Sophie Ebner

November 2021



MONTANUNIVERSITÄT LEOBEN

www.unileoben.ac.at

AFFIDAVIT

I declare on oath that I wrote this thesis independently, did not use other than the specified sources and aids, and did not otherwise use any unauthorized aids.

I declare that I have read, understood, and complied with the guidelines of the senate of the Montanuniversität Leoben for "Good Scientific Practice".

Furthermore, I declare that the electronic and printed version of the submitted thesis are identical, both, formally and with regard to content.

Date 09.11.2021

A handwritten signature in blue ink, reading 'Anna Sophie Ebner', written over a horizontal line.

Signature Author
Anna Sophie Ebner

The authors gratefully acknowledge the financial support under the scope of the COMET program within the K2 Center “Integrated Computational Material, Process and Product Engineering (IC-MPPE)” (Project No 859480). This program is supported by the Austrian Federal Ministries for Climate Action, Environment, Energy, Mobility, Innovation and Technology (BMK) and for Digital and Economic Affairs (BMDW), represented by the Austrian research funding association (FFG), and the federal states of Styria, Upper Austria and Tyrol. The computational results presented have been achieved using the Vienna Scientific Cluster (VSC).

Danksagung

An erster Stelle möchte ich mich bei jener Person bedanken, die es mir ermöglicht hat in ihrer Arbeitsgruppe meine Dissertation zu verfassen. Meiner Betreuerin Verena Maier-Kiener sei für die ausgezeichnete Betreuung und die hochkarätigen fachlichen Diskussionen gedankt. Liebe Verena, danke, dass du mir in den letzten Jahren zu jeder Uhrzeit und in allen Anliegen zur Seite gestanden bist, sei es bei technischen Problemen mit dem Nanoindenter oder beim Einreichprozess der ersten Veröffentlichungen. Du bist für mich ein großes Vorbild, wie du zusätzlich zu deinen Aufgaben als Mutter noch die Betreuung deiner Arbeitsgruppe und deiner Dissertanten hervorragend meisterst.

Auch meinem Mentor, Reinhard Pippan, möchte ich herzlich danken. Die Schlussfolgerungen meiner wissenschaftlichen Arbeiten haben sehr von seinem umfassenden Wissen zur Wasserstoffversprödung profitiert und bei den Diskussionen mit ihm konnte ich mein fachliches Wissen erweitern.

Ein Dankeschön gilt auch Helmut Clemens, der mir nicht nur die Möglichkeit gab diese Arbeit an seinem Lehrstuhl durchzuführen, sondern der auch jedes Manuskript in Windeseile übers Wochenende korrigiert und so die Einhaltung aller Fristen möglich gemacht hat.

Besonderen Dank möchte ich auch an Steffen Brinckmann aussprechen. Er ist mir vor allem zu Beginn der Arbeit beim Design und der technischen Umsetzung immer mit Rat und Tat zur Seite gestanden. Ohne seine Hilfe wäre ich bei der Implementierung des Aufbaus verzweifelt. An dieser Stelle möchte ich mich auch bei Alexander Leitner bedanken, der bei der anschließenden Umsetzung und den Lötarbeiten unterstützte.

Für den reibungslosen und erfolgreichen Ablauf des Projektes möchte ich mich auch bei Vsevolod Razumovskiy vom Materials Center Leoben bedanken, der für alle organisatorischen Anliegen immer ein offenes Ohr hatte. Auch Ernst Plesiutchnig und Andreas Keplinger sei für die fachliche Unterstützung von Seiten voestalpine Böhler Edelstahl gedankt.

Des Weiteren möchte ich mich bei den Mitarbeitern des Lehrstuhls Metallkunde bedanken, welche mit ihrer Arbeit einen reibungslosen Ablauf ermöglichten. Vor allem möchte ich mich bei unserem Sekretariat, mit Angelika Tremmel, Regina Kranz, Susanne Strasak und Reinhilde Stopar, für die immer schnelle Hilfestellung in allen Belangen bedanken.

Auch über unseren Lehrstuhl hinaus wurde ich von den Mitarbeitern des Lehrstuhls Materialphysik tatkräftig unterstützt. Allen voran gilt ein besonderer Dank Daniel Kiener für die fachlichen Gespräche im Zuge der Kaffeepausen während meiner Messaufenthalte am ESI. Ebenso möchte ich mich bei Franz Hubner für die präzise Fertigung der elektrochemischen Zelle bedanken, sowie bei Caroline Freitag, welche mich mit ihrem Wissen bei der Elektropolierstudie unterstützte.

Nicht nur das wissenschaftliche und das organisatorische Umfeld sind für den erfolgreichen Ablauf einer Dissertation notwendig, sondern auch die kollegiale Unterstützung und der Zusammenhalt. Allen voran möchte ich meinen Kollegen der ME&H Gruppe Severin Jakob, Johann Kappacher und Maximilian Siller danken. Es hat sich durch gemeinsam besuchte Konferenzen und vor allem durch unseren Road-Trip in Texas eine großartige, über das Arbeitsverhältnis hinausreichende, Freundschaft entwickelt. Ein weiterer Dank gilt auch meinen Büro-, Dissertanten- und Arbeitskollegen, vor allem Matthias Hofinger, Andreas Landefeld, Irmgard Weißensteiner, Michael Burtscher und Dominik Gehringer, die immer mit Rat und Tat mitfühlend zur Seite standen, wenn es mal nicht so gut lief.

Ein großer Dank geht an dieser Stelle an meine Arbeitskollegin Christina Hofer, mit der sich über die letzten Jahre auch eine besonders gute Freundschaft entwickelt hat. Liebe Chrisi, danke für deine Unterstützung und deine Motivation auf den letzten Metern des Verfassens dieser Arbeit. Danke, dass du auch aus der Ferne immer aufbauende Worte für mich parat hattest, als ich selbst gerade am Verzweifeln war.

Abschließend möchte ich mich natürlich auch bei meiner gesamten Familie bedanken, die immer hinter mir steht und mich auf meinem Weg begleitet und unterstützt. Die gemeinsamen Familienwochenenden zuhause waren immer eine schöne Abwechslung zu der doch oft fordernden Arbeit. Bei diversen Spaziergängen und gutem Essen konnte ich wieder Kraft tanken. Zu guter Letzt gilt ein besonderer Dank meinem Freund Alexander, der mich nun schon seit Beginn meiner Dissertation begleitet und dabei alle Höhen und Tiefen gemeinsam mit mir erlebt hat. Danke für deine große Unterstützung und die vielen, schönen Spaziergänge und Wanderungen zusammen mit Maggie. Vielen Dank für diese gemeinsame Zeit, die besondere Kraft gibt.

Abstract

Due to the continuously increasing global energy demand and the simultaneous efforts to reduce CO₂ emissions, renewable and alternative energy sources are required in order to achieve these contrary goals. A promising candidate in the area of sustainable energy supply, whether for storage, transport or mobility, are hydrogen technologies. In order to enable a safe handling, it is essential to investigate the materials resistance against hydrogen degradation, as well as to improve and develop new alloys for future applications. Although the problem of hydrogen embrittlement in metals has been studied for many years, no consensus has been reached on the prevailing mechanisms. Furthermore, a number of component failures of nickel-base alloys, which have been attributed to hydrogen embrittlement, were reported over the years for applications in oil and gas industry. In order to shed some light on the underlying mechanisms and failure reasons, the scientific community is striving to improve existing experimental methods and to find new approaches to further develop promising material classes for application in hydrogen containing environments.

Therefore, in this PhD thesis the technique of in-situ electrochemical nanoindentation is implemented, applied and further developed through combination with advanced measurement protocols. Besides, the determination of the fundamental mechanical properties of Young's modulus and hardness, the main focus was on the investigation of the plastic deformation mechanisms. The experiments, which were conducted on the nickel-base alloy 725, showed a hydrogen-induced hardness increase for both investigated heat treatments. Furthermore, the influence of hydrogen on the strain rate dependent deformation parameters, i.e. strain rate sensitivity and activation volume, could be revealed. These experiments were complemented with detailed optical evaluation of the plastically deformed zone using scanning electron microscopy as well as laser scanning confocal microscopy. As a second approach, additionally to the determination of the influence of hydrogen on the mechanical properties, a concept of segregation-based grain boundary design was developed and applied to alloy 725. This approach is based on a simulation-based prediction and the experimental verification of the grain boundary segregation by means of atom probe tomography. An extraordinary quantitative agreement of the applied methods was achieved. The gained knowledge can be used in the future for the development and improvement of nickel-base alloys.

The present work conducted with the above-mentioned methods should, therefore, contribute to a better understanding of the acting mechanisms and opens up the possibility to test the materials resistivity against hydrogen embrittlement. Furthermore, a targeted material improvement is possible to meet the high requirements for future applications under the influence of hydrogen.

Kurzfassung

Angesichts des gegenwärtig weltweit steigenden Energiebedarfs und dem gleichzeitigen Bestreben nach Verringerung der CO₂ Emissionen, ergibt sich die Notwendigkeit neue und umweltfreundliche Energieträger zu finden, damit diese beiden Ziele verwirklicht werden können. Große Hoffnung im Bereich der nachhaltigen Energieversorgung, sei es für Speicherung, Transport oder Mobilität, wird hierbei auf den Wasserstoff gesetzt. Um einen sicheren Umgang mit diesem Energieträger zu ermöglichen, ist es unerlässlich die eingesetzten Materialien auf ihre Beständigkeit unter dem Einfluss von Wasserstoff zu untersuchen. Obwohl die Problematik der Wasserstoffversprödung von Metallen schon über viele Jahre hinweg erforscht wird, wurde noch kein Konsens über die herrschenden Mechanismen erzielt. Außerdem sind in den letzten Jahren einige Schadensfälle an Einsatzkomponenten aus Nickelbasis-Legierungen in der Erdöl- und Erdgasindustrie zu verzeichnen gewesen, welche auf ein Versagen durch Wasserstoffversprödung zurückzuführen sind. Um Klarheit über die herrschenden Mechanismen und die Versagensursachen zu erlangen, ist die Wissenschaft bestrebt bestehende experimentelle Methoden zu verbessern und neue Lösungsansätze zu finden, um bestehende Materialien weiterzuentwickeln und damit weiteren Schadensfällen vorzubeugen.

In der vorliegenden Dissertation wird daher die Methode der elektrochemischen in-situ Nanoindentation implementiert, angewandt und mit vertiefenden Methoden weiterentwickelt. Neben der Ermittlung der grundlegenden mechanischen Eigenschaften von Elastizitätsmodul und Härte, stand vor allem die Untersuchung der plastischen Verformungsmechanismen im Vordergrund. Die Versuche, durchgeführt an der Nickelbasislegierung 725, zeigten einen wasserstoffinduzierten Anstieg der Härte für beide untersuchten Wärmebehandlungen. Ebenso konnte der Einfluss des Wasserstoffs auf die Verformungsparameter der Dehnratenabhängigkeit und des Aktivierungsvolumens gezeigt werden. Komplementiert wurden diese Experimente mit der optischen Evaluierung der plastisch verformten Zone mittels Rasterelektronenmikroskopie sowie konfokaler Laserscanning-Mikroskopie. Darüber hinaus wurde an obengenannter Legierung ein Konzept des segregationsbasierten Korngrenzdesigns entwickelt. Dieses setzt sich aus einer Voraussage mittels unterschiedlicher Simulationsmethoden und der experimentellen Verifikation der Korngrenzsegregation mittels Atomsonden-Tomographie zusammen. Es konnte eine außerordentlich gute, quantitative Übereinstimmung der verwendeten Methoden erreicht werden, welche in Zukunft für die Entwicklung und Verbesserung von anderen Nickelbasis-Legierungen eingesetzt werden kann.

Die obengenannten Methoden sollen dazu beitragen, ein besseres Verständnis der ablaufenden Mechanismen zu erlangen, sowie die Möglichkeiten eröffnen, Materialien auf ihre Beständigkeit zu prüfen und gezielte Optimierungen durchzuführen, um den hohen Anforderungen für den zukünftigen Einsatz unter dem Einwirken von Wasserstoff gerecht zu werden.

Content

1. MOTIVATION AND AIM OF THE THESIS.....	1
2. STATE OF THE ART	3
2.1. HYDROGEN-MATERIAL INTERACTION	3
2.1.1. <i>Hydrogen uptake and diffusion.....</i>	<i>6</i>
2.1.2. <i>Hydrogen embrittlement mechanisms.....</i>	<i>9</i>
2.2. NICKEL-BASE SUPERALLOYS	13
2.2.1. <i>Microstructure and fundamental properties</i>	<i>13</i>
2.2.2. <i>Interactions with hydrogen.....</i>	<i>14</i>
2.3. GRAIN BOUNDARY SEGREGATION	18
2.4. NANOINDENTATION	25
2.4.1. <i>Conventional Nanoindentation.....</i>	<i>25</i>
2.4.2. <i>Advanced nanoindentation methods.....</i>	<i>27</i>
2.4.3. <i>Electrochemical nanoindentation</i>	<i>31</i>
3. IMPLEMENTATION OF THE ELECTROCHEMICAL SETUP	36
3.1. THE NANOINDENTATION PLATFORM.....	36
3.2. CELL DESIGN	37
3.3. IMPLEMENTATION.....	39
3.4. TIP AND TIP CALIBRATION	41
3.5. ELECTROCHEMICAL CHARGING.....	43
3.6. TESTING PROCEDURE AND CHALLENGES	46
4. SUMMARY OF THE PUBLICATIONS	50
4.1. PUBLICATION LIST	51
4.2. INFLUENCE OF HYDROGEN ON STANDARD NANOMECHANICAL PROPERTIES OF A NICKEL-BASE ALLOY (PUBL. A)	53
4.3. INFLUENCE OF HYDROGEN ON PLASTIC DEFORMATION PARAMETERS OF A NICKEL-BASE ALLOY (PUBL. B)	55
4.4. GRAIN BOUNDARY ENGINEERING WITH ATOM PROBE TOMOGRAPHY AND DENSITY FUNCTIONAL THEORY (PUBL. C)...	57
5. CONCLUSIONS AND OUTLOOK.....	60
6. REFERENCES	62
7. PUBLICATIONS.....	71
PUBLICATION A	72
PUBLICATION B.....	95
PUBLICATION C.....	123

Abbreviations

AIDE	adsorption-induced dislocation emission
APT	atom probe tomography
bcc	body-centred cubic
cLR	constant load rate
CSM	continuous stiffness measurement
cSR	constant strain rate
DFT	density functional theory
EBSD	electron backscatter diffraction
fcc	face-centred cubic
FIB	focused ion beam
GB	grain boundary
GBE	grain boundary engineering
hcp	hexagonal-closed packed
HE	hydrogen embrittlement
HEA	high entropy alloy
HEDE	hydrogen-enhanced decohesion
HELP	hydrogen-enhanced localized plasticity
IG	intergranular
IPF	inverse pole figure
LSCM	laser scanning confocal microscope
Ni	nickel
ROI	region of interest
SE	secondary electron
SEM	scanning electron microscopy
SSRT	slow strain rate tensile test
TG	transgranular
TKD	transmission Kikuchi diffraction

1. Motivation and aim of the thesis

As a result of the ongoing industrialisation, the global energy demand is constantly increasing and the necessity for renewable and alternative energy sources becomes more and more important. Furthermore, the effort for reduction of CO₂ emission in order to retard the global climate change is inevitable. The aim for "affordable and clean energy" is also established in the Sustainable Development Goals of the United Nations [1]. Therefore, not only countries and industry, but also science is called upon to contribute to achieve these goals.

A major role in the field of sustainable energy supply is given to hydrogen. The use of hydrogen for energy storage and for unsophisticated energy transport will make an important contribution towards replacing or at least minimizing the use of fossil fuel in the future. One of the greatest challenges, however, will be the safe handling of the large amount of hydrogen. For this purpose, it is essential to develop reliable materials that are suitable for application in hydrogen containing environments and can withstand the harsh chemical and mechanical exposure during service. The problem of hydrogen embrittlement (HE) in metals was first discovered in 1875 by William H. Johnson [2]. This author showed a dramatic reduction of the mechanical properties in iron and steel when exposed to acidic solution under formation of hydrogen. This was the initiation for research on HE in science and industry, which continued for almost 150 years until now. Although research is already conducted for many years no consensus is reached on the acting mechanisms during HE. The scientific community is therefore continuously developing new methods for investigating and improving existing material classes or even to develop new promising ones.

One material class with auspicious properties for the use in hydrogen environments, which is already widely used in high temperature, aerospace and oil and gas applications, are nickel-base alloys. Due to their versatile alloy composition and their complex microstructure, which can be tuned through different heat treatments, they show excellent chemical and mechanical resistance. Nevertheless, some failure cases, which were attributed to HE [3,4], are reported from the oil and gas industry. In order to avoid these damages in the future and to further investigate this class of materials regarding their applicability in the field of hydrogen storage and transport, versatile methods for probing the mechanical properties will be essential

for future research. Since the acting embrittlement mechanisms take place on a local microstructural scale the investigation methods have to be adapted to this size regime. For the local investigation of mechanical properties, such as hardness and Young's modulus, nanoindentation has been established over the last years and already found its way into research of HE.

Consequently, the main objective of this work was therefore to implement a setup, which allows the investigation of the mechanical properties of different materials by means of nanoindentation under the influence of hydrogen charging. In addition to the basic mechanical characterisation, advanced methods should be developed to gain fundamental knowledge about the acting mechanisms of plastic deformation. The nickel-base alloy 725 was chosen as model material for this purpose, as it is of great relevance for future applications and material suppliers. In addition to the method development and the mechanical characterisation, an approach of segregation-based grain boundary (GB) design was proposed. It works as a pioneering method for material development based on targeted modification of the chemical composition using simulation-based predictions and experimental confirmations.

This work will help to gain a better understanding on the acting HE mechanisms by providing advanced experimental methods. Furthermore, it opens up the possibility of a segregation-based grain boundary engineering (GBE) approach, which can be used in future to develop materials more resistant to HE.

2. State of the art

The intention of this section is to give an overview of all necessary pre-knowledge to the attached publications in Part II of this thesis and is divided into four parts.

For the understanding and investigation of materials degradation caused by hydrogen, the basics for hydrogen interaction, uptake and diffusion are essential requirements for deeper comprehension. Therefore, the first section will give a detailed view on these hydrogen-material interactions. Furthermore, the proposed mechanisms for the embrittlement itself are briefly described in the section 2.1. The material class of nickel-base alloys is briefly introduced in section 2.2, as it was the mainly investigated material during this thesis. Chapter 2.3 includes the principles of atom probe tomography (APT), which was used in Publication C. At last, the basics of nanoindentation will be described in section 2.4 as a framework for the implementation of the electrochemical setup.

2.1. Hydrogen-material interaction

Depending on the materials class and the application field of the component the time in which hydrogen uptake occurs can vary. A rough classification of the phenomenon can be made by distinguishing the source where the hydrogen comes from. Hydrogen, which is already dissolved in the matrix prior to loading can be ascribed to internal hydrogen embrittlement (IHE). This type of hydrogen uptake can occur during the fabrication process of a component. Throughout the metallurgical processing, e.g. melting the solubility of hydrogen is much higher than for the solid, and therefore must be controlled and monitored carefully during production [5,6]. Also during the fabrication process, including welding and machining, hydrogen can be introduced in the material. Furthermore, surface treatments like pickling, carbonizing or electroplating are possible sources for hydrogen uptake [7]. Thus, this internal hydrogen is therefore already present before the component gets into service.

In contrast the external hydrogen embrittlement, also known as hydrogen environment/environmental embrittlement (HEE), is attributed to hydrogen uptake from a hydrogen containing environment surrounding the material or component during service. This hydrogen environment may be a partial pressure of gaseous hydrogen during storage or

transportation or it can originate from corrosion in acidic environments or even cathodic protection. Especially the cathodic protection plays an important role in offshore fields, where it is used to protect components in subsea applications from corrosion.

All influencing factors on the severity of HE can be grouped into three main sections, which are schematically illustrated in Fig. 2-1. The root cause is the material susceptibility itself. Two further parts contributing to the HE phenomenon are the environmental condition as well as mechanical loading. For HE all three conditions must coexist.

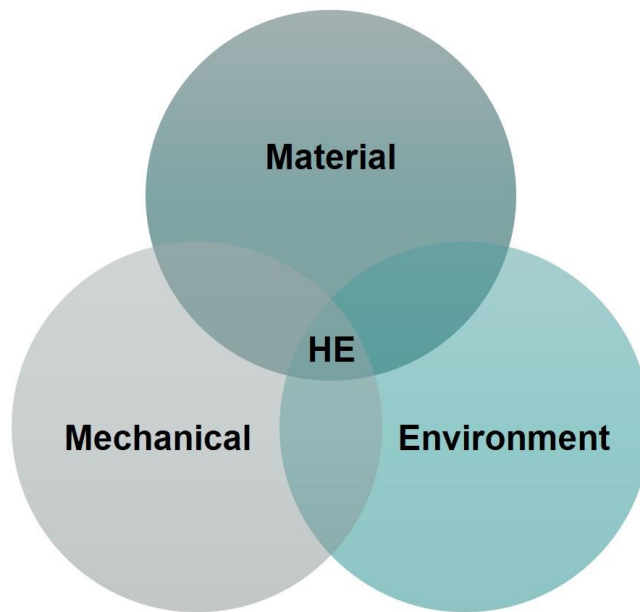


Fig. 2-1: Influencing variables on HE

Material

The material susceptibility to HE depends on a variety of parameters. Beside crystal structure and diffusion behaviour also the microstructure and material strength are important parameters. Overall an increasing strength comes along with an increased susceptibility to HE [8]. Nevertheless, it must be distinguished between the different sources of hydrogen. For example, high-strength martensitic steels (yield strength > 1400 MPa) are extremely susceptible to IHE, whereas in comparison ferritic steels (yield strength < 750 MPa) even with high hydrogen concentrations up to ~10 ppm are still quite resistant. In comparison to steels with body-centred cubic (bcc) crystal structure, materials with face-centred cubic (fcc) structure show less or even no susceptibility to IHE. For HEE the same assumption regarding susceptibility and strength can

be drawn. Only nickel-base alloys are an exception; although a good resistance against IHE is present lots of failures are reported, which occurred in service and can be attributed to external hydrogen and HEE [4,3].

Environment

As previously mentioned the source of hydrogen can be classified into internal and external hydrogen, but can be further divided, because the exact origin of the hydrogen can have great influence on the characteristics of the HE [9]. IHE is mostly introduced by chemical solutions, which are used for preparing the surface for cleaning, pickling or coating. Especially for electroplating hydrogen adsorption is reported by Figueroa et al. [7] during corrosion of the sacrificial metal coating. Furthermore, welding, especially in moist atmosphere, can promote the failure due to IHE [10]. This absorption of internal hydrogen, however, can be minimized by careful process control.

Several works have investigated the divergent behaviour of metallic materials when exposed to different types of hydrogen. For example, Symons et al. [6] compared the degree of embrittlement of a nickel-base alloy X-750 for the case of internal and external HE. The differences in characteristic fracture distance explained the changes in susceptibility to HE and could be related to de-cohesion and hydrogen-enhanced plasticity. More recent work conducted by Zhao et al. [11] compared the changes in nanomechanical properties gained by nanoindentation of a high entropy alloy (HEA), which was exposed to gaseous and electrochemical charging. Whereas, the electrochemical charging showed significant hardness increases, the changes for gaseous charging remained invariant. This was attributed to the different H distributions induced by the charging methods. Especially the influence of hydrogen gas will gain more and more importance in the future, since the use of hydrogen as an energy source and carrier is planned to increase over the next years.

Mechanical

This section contains all aspects of mechanical and internal stress contributions. Beside the external loading in monotonic or cyclic regime, also the internal stress contributions can have influence on the severity of HE. Overall, all types of tensile stresses promote the uptake of hydrogen, e.g. macroscopic tensile loading or residual tensile stresses. Furthermore, high

hydrostatic stress concentration at the crack tip, vacancies or dislocation cores increase the hydrogen concentration, confirming the importance of stresses on the HE phenomenon. [9]

2.1.1. Hydrogen uptake and diffusion

The first step towards HE is apparently the uptake and absorption of hydrogen into the susceptible material. This process depends on the already mentioned way in which hydrogen is supplied, internal or external. And as a consequence the occurring surface reactions can evolve differently.

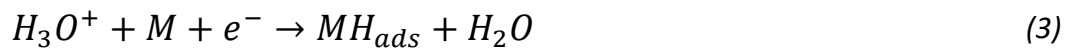
As a result of its size, molecular hydrogen gas can only enter into the metal, when it is in molten state during the metallurgical process, and provides internal hydrogen after dissociating during solidification and remain as mono-atomic solute. For absorption into a solid metal, the H_2 must be dissociated on the surface, before entering. According to Sieverts law [12], the hydrogen dissolved into a metal is proportional to the hydrogen partial pressure P_{H_2} at equilibrium:



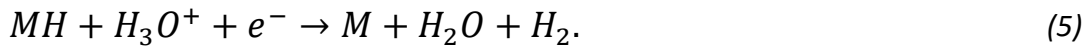
$$C = KP_{H_2}^{1/2}, \quad (2)$$

where K is a constant and is the C solubility of hydrogen in the metal, which can depend on the application temperature [13]. Accordingly, the hydrogen partial pressure and the temperature are the two limiting factors of hydrogen absorption through pressurized hydrogen gas [14].

Electrochemical charging on the other hand is a further possible way for hydrogen to enter the metal surface. This charging method is especially important for scientific purpose since it is easy to implement in laboratory scale without the necessity of handling big amount of pressurized hydrogen gas. The process of electrolytic charging can be divided into 3 steps and is commonly known as hydrogen evolution reaction (HER) [15]. The first step is the adsorption of a hydrogen atom on the metal surface through the Volmer reaction following Eq. (3) for acidic solutions:



The following desorption of the hydrogen can be described through the Tafel or the Heyrovsky equation, where most of the hydrogen recombines and escape through the electrolyte in gaseous form. Thereby, the Tafel reaction Eq. (4) accounts for the chemical desorption, whereas the Heyrovsky reaction describes the electrochemical desorption through Eq. (5) in acidic solution:



The formation of local corrosion elements leads to hydrogen adsorption on the sample surface through the corrosion process. The amount of absorbed hydrogen depends on the severity of this corrosion attack [16].

Last possibility for the generation of adsorbed hydrogen on the metal surface is the so-called cathodic hydrogen charging, which occurs e.g. during cathodic protection and also work in neutral solutions [16]. At the cathodically polarized electrode atomic hydrogen is formed through chemical reduction and the amount of adsorbed hydrogen is proportional to the charge current density:



Regardless of the type of charging, a small amount of the adsorbed hydrogen, which does not recombine to molecular H_2 , can be absorbed through the metal surface:



To promote this entry and inhibit the recombination reaction, a recombination poison can be added to the electrolyte. The most common one for electrochemical charging of steels is CH_4N_2S (Thiourea) [17–19]. For example, with an addition of 1 g/l Thiourea, the hydrogen concentration in a high strength steel sheet can be maximized and saturates around ~ 1.5 *wppm*, in comparison to ~ 0.15 *wppm* without Thiourea [20].

As soon as a considerable amount of hydrogen is absorbed into the solid metal, diffusion starts to take place. The concentration gradient driven diffusion is described by Fick's law [21]:

$$j_D = -D \frac{dc}{dx}, \quad (8)$$

where j_D is the diffusion flux density, which states the number of atoms passing through a unit area per unit time. This flux density is proportional to the concentration gradient through the proportionality constant D , which is called diffusion constant or diffusion coefficient. The diffusion coefficient D exhibits an exponential temperature dependence and is mainly influenced by the crystal structure and the diffusing element, which is incorporated in the activation energy Q and the pre-exponential factor D_0 :

$$D = D_0 \cdot e^{\left(-\frac{Q}{kT}\right)}, \quad (9)$$

where k represents the Boltzmann constant. In general, hydrogen diffusion at ambient temperature is around 5 times higher in magnitude for materials with bcc crystal structure, than for fcc and hexagonal closed packed (hcp) materials [22]. This is mainly due to the differences in packing fraction of the crystal structures, this results in distinct different diffusion paths. For example the hydrogen diffusion distance for bcc iron with a diffusion coefficient of $D \sim 10^{-5} \text{ cm}^2/\text{s}$ accounts for 50 μm in 1 s, whereas for nickel with $D \sim 10^{-10} \text{ cm}^2/\text{s}$ the diffusion distance is a factor 500 times smaller with only 0.1 μm . In dependence of the complexity of the microstructure the effective diffusion coefficient is moreover highly influenced by the existence of hydrogen trapping sites [9].

When considering possible sites for hydrogen, it is necessary to differentiate between sites on atomic or microstructural scale. Due to its small size hydrogen can occupy interstitial lattice sites, which are tetrahedral ones for bcc and hcp metals and octahedral ones for fcc structures. Additional to normal interstitial sites other favourable trapping sites with lower potential energy are present on the atomic scale, including vacancies, vacancies cluster, dislocation cores and/or GBs. Due to their disordered structure this sites can accumulate higher amounts of hydrogen. On the microstructural scale hydrogen furthermore gathers at precipitates, inclusions, voids and ahead of crack tips due to the high hydrostatic stress field in front of it [9]. Regarding their activation energy traps can be divided into reversible and irreversible traps [23]. For reversible traps, hydrogen can escape the trapping site, e.g. when temperature increases, and

can become mobile again. The threshold in binding energy, which separates reversible from irreversible traps, is not exactly defined in literature, since it depends on material, time and environment [22].

2.1.2. Hydrogen embrittlement mechanisms

The following section should briefly discuss the most common HE mechanisms, which were proposed over several years of research and are schematically depicted in Fig. 2-2. Different research groups have focused on individual mechanisms, which they supported with firm conviction. Even though the proposed mechanisms have different approaches, overlaps are possible [8]. It strongly depends on the investigated material, environment and the used experimental approach, which mechanism can explain the findings in the best way. Moreover, it is also possible to use more than one mechanism for elucidating hydrogen-related material degradation [24,25].

Hydrogen-induced decohesion (HEDE)

Based on early works by Pfeil [26] and Troiano [27], the decohesion hypothesis was born, which involves the preference of the weakening of interatomic bonds by tensile separation over slip-induced deformation. This mechanism, which is illustrated in Fig. 2-2a, was further developed and got popular by the works of Oriani [28] and Gerberich [29]. The main point is the reduction of cohesive energy at specific regions in the crystal lattice, exhibiting a higher hydrogen concentration due to hydrostatic stress fields, which especially occur at sharp crack tips [30]. The experimental validation of this proposed model is still missing, since no techniques can investigate these interactions on an atomic scale. Therefore, most research was done through density functional theory (DFT) calculations or cohesive zone models [31–33].

Hydrogen-enhanced localized plasticity (HELP)

A mechanism, which seems to be controversial when talking about embrittlement is the HELP mechanism, which is schematically depicted in Fig. 2-2b. It proposed, that the failure occurs due to plastic deformation by hydrogen increasing the dislocation mobility.

The first reference in literature can be found in the work of Beachem [34], whose experiments showed tear ridges and pronounced dimples on fracture surfaces of steel suffered

from HE. This author postulated that the dislocation activity is promoted by hydrogen and it allows the dislocation to move and multiply at lower applied stresses. This first investigations were only based on post-mortem analysis of the fracture surface and were not able to describe the acting processes themselves. First experimental validation was achieved by the research group of Birnbaum, Robertson and Sofronis [35–37] in the 1980s by conducting in-situ deformation experiments in a transmission electron microscope (TEM). This allowed the first real time observation of dislocation movement in a gaseous hydrogen environment for different materials as iron [36], nickel [35] and aluminium [37]. They concluded that hydrogen lowers the required stress for dislocation motion, furthermore it enhances the dislocation activity, increases the dislocation source activation and thus favours a localized deformation through micro-void formation [38]. Later on the hydrogen shielding effect was proposed by Birnbaum and Sofronis [38,39], with which they explained the promoted dislocation motion.

Although, the experimental observations strongly support the HELP mechanism, contradictory research was published, experimental as well as by simulation approaches. Atomistic simulation done by Song and Curtin [40,41] disproved the shielding effect of hydrogen in iron and even suggested a reduced dislocation mobility according to solute drag theory [42]. Furthermore, it was pointed out for bcc metals, that the hydrogen concentration, which is needed for softening effects of HELP mechanism, are not realistic [43]. On the experimental side, micro-cantilever experiments by Deng et al. [44] proposed hydrogen-reduced dislocation mobility, which is quite the opposite to HELP mechanism. Nevertheless, HELP mechanism is still one of the most cited and proposed mechanisms over the last decades of research in the fields of HE.

Adsorption-induced dislocation emission (AIDE)

The AIDE mechanism, which was firstly reported by Lynch [45] is shown in Fig. 2-2c. It is the most complex one of the three described mechanisms and combines basic principles of both, HEDE and HELP mechanism. Based on the first experiments of Clum [46] with field ion microscopy, he suggested that adsorbed hydrogen at the crack tip surface might facilitate dislocation nucleation. With his further works Lynch [47,48] tried to address the missing explanation with fractographic observations, on how this eased dislocation emission can lead to embrittlement.

The emission of dislocations at the crack tip includes the nucleation as well as the movement of dislocations away from the crack tip. The nucleation itself gets facilitated through the adsorbed hydrogen at the surface of the crack tip. For the nucleation a dislocation core and a surface step must develop by shearing of atoms over several atomic distances. This shearing requires a separation of the interatomic bonds, which are weakened by the adsorbed hydrogen similar to the HEDE mechanism. In ductile fracture mode, the main crack propagation arises from micro-void formation and coalescence, since interatomic bonds at the crack tip are strong and therefore it is favourable in contrast to crack growth directly from the crack tip by intersecting dislocations. In the presence of adsorbed hydrogen, the emission from the crack tip is facilitated and the crack growth occurs directly on suitable inclined slip planes. Nevertheless, also nucleation and growth of voids ahead of the crack tip inside the plastic zone occur and contribute to the crack growth. These micro-voids can sharpen the crack tip leading to small crack tip opening angles. This coalescence occurs at lower strains and result in a smaller dimple size compared to fracture in inert environment [9].

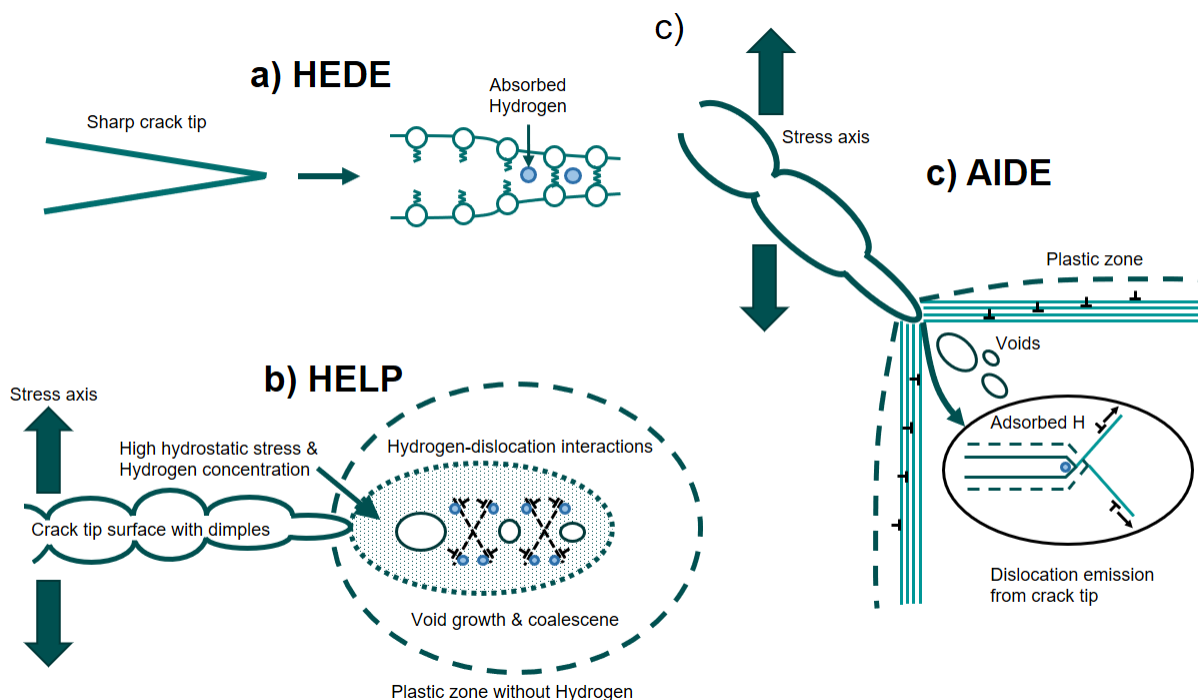


Fig. 2-2: Schematic drawings of most known HE mechanism: a) HEDE, b) HELP and c) AIDE, redrawn from [9].

As mentioned in the beginning of this section, HE is a complex phenomenon and the occurring deformation process cannot be explained by a single mechanism to fit all observed results. Experiments at different length scale, with critical scrutinized discussion can help to improve the understanding and shed more light on the acting mechanisms.

2.2. Nickel-base superalloys

The class of nickel-base superalloys was originally designed for high temperature application in the 1950s due to their excellent performance against chemical and mechanical degradation [49]. They were primarily used for jet engines and gas turbines, where temperature can reach up to 1000 °C. Despite these high temperatures the material must withstand mechanical loading and must further exhibit a good creep resistance in aggressive environment. Especially, coal-fired hot gases contain a high amount of Sulphur, which can lead to a severe corrosion attack.

Later on, the suitability of this alloy class was also discovered for applications in the oil and gas industry in the 1960s. Well bore components are often made out of nickel-base superalloys due to their before mentioned characteristic properties. During exploitation high pressure, high temperature and when dealing with “sour” fields also considerable amounts of H₂S are present. Furthermore, cathodic protection is often used for corrosion control for subsea applications in marine waters. In both cases, hydrogen can be generated at the surface and surrounding and subsequently interacts with the material. Therefore, especially precipitation hardened nickel-base alloys are a promising material class for hydrogen-related applications [50].

The next sections should briefly summarize the physical metallurgical basics and the consequential properties. Furthermore, the importance of GB segregation and corresponding experimental and simulation-based evaluation methods for its characterization are described.

2.2.1. Microstructure and fundamental properties

In general, nickel-base super alloys can be divided into solid-solution strengthened and precipitation strengthened alloys. For high performance application the precipitation hardened alloy modification is the most commonly used. A broad range of alloys, as e.g. Inconel 718, 725, 709, Nimonic 90, X-750 is commercially available on the market and offered by different material suppliers. The microstructure of this alloys comprises of the following features [49]:

- the γ -matrix,
is a solid solution phase with fcc crystal structure. Beside nickel as main element it contains a high amount of solid-solution elements such as Mo, Fe, Cr and W or other alloying elements.
- the intermetallic γ' phase
is one of the two main strengthening phases. It has an ordered fcc $L1_2$ crystal structure and precipitates in coherent spherical or cuboidal shape. The chemical composition according to the phase diagram is Ni_3Al .
- the intermetallic γ'' phase
is the second strengthening precipitate with a bcc tetragonal crystal structure. Its stoichiometric composition is Ni_3Nb and it has a preferential role in Fe and Nb containing alloys (as 718 and 725). The shape of the precipitates is of a disc-shaped morphology with diameter around 50 nm and thickness of approx. 10 nm.
- carbides and borides
can occur, depending on the C and B content in the respective alloy. The most common have the following stoichiometric composition MC , M_6C , $M_{23}C_6$ and M_3B_2 , where M is a metal atom e.g. Cr, Mo or Ti.
- the unwanted topological closed packed phases (TCP)
can have complex crystal structures. Some examples are the μ -, σ - or the recently discovered F-phase [51]. Due to their detrimental embrittling nature at GBs this phases are tried to be avoided for better mechanical performance.

This unique phase constellation is responsible for the characteristic mechanical properties, whereas the mechanical performance is mainly attributed to the strengthening phases γ' and γ'' . The good chemical resistance is obtained through the high chromium content.

2.2.2. Interactions with hydrogen

First experiments on the HE resistance of nickel-base alloys were already conducted in 1970 by Walter et al. [52]. The following paragraphs should give a brief overview of the state-of-the-art regarding nickel-base alloys and their performance against HE. Beside some basic information about hydrogen diffusion also the fracture process will be described.

Hydrogen diffusion in nickel-base alloys

To better understand the behaviour of hydrogen in nickel-base alloys the diffusion properties must be accounted. As already mentioned in section 2.1.1 the diffusion coefficient for fcc crystal structure is comparable low, even for such a small element like atomic hydrogen.

In order to demonstrate this low diffusion behaviour, Fig. 2-3 shows the diffusion path x over time t for the temperature of 50°C estimated through the equation for the Einstein mean diffusion length:

$$x = \sqrt{2Dt}, \quad (10)$$

with D as the effective hydrogen diffusion coefficient derived by Jebaraj et al. [53] by means of permeation experiments. The effective hydrogen diffusion coefficient is strongly influenced by the material condition and heat treatments. When comparing the diffusion length for a charging of 4 hours, which is later on used in this thesis as pre-charging time, the estimated values are 42 μm for pure nickel, 19 μm for solution annealed (SA) 718 sample and only 12 μm for the precipitation hardened (PH) state. For comparison, in permeation experiments on recrystallized Armco iron (bcc) with the calculated diffusion coefficient a diffusion length of 13 mm could be reached in the same time [54].

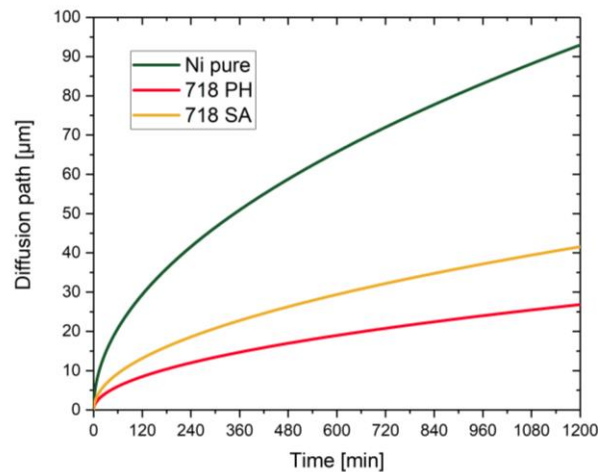


Fig. 2-3: Diffusion path at 50°C for hydrogen in nickel and nickel-base alloy 718 for solution annealed (SA) and precipitation hardened condition (PH).

With this diffusion behaviour in mind, the charging times must be adapted for the different materials and experiments. As nanoindentation only tests the first few micrometres, short charging times can be realized for such experiments [55], and also fcc material as alloy 718 and 725 can be tested without tremendous time efforts. In contrast, in-situ slow strain rate tensile tests on the same material require a pre-charging time of 18 h [56].

Fracture of nickel-base alloys under hydrogen influence

As already mentioned in the motivation of this thesis in section 1, in the past a couple of failure cases on nickel-base components in the oil and gas industry have occurred and are presented in literature [4,3]. The reason was often found in the hydrogen-assisted cracking (HAC), which is related to the susceptibility to HE. The main failure modes in nickel-base alloys can be divided into intergranular (IG) and transgranular (TG) crack propagation.

IG cracking

Various failure cases show fracture surfaces with IG appearance. GB are favourable sites for crack initiation. On the one hand the hydrogen diffusion is enhanced due to the higher disorder of atoms at the GB, and on the other hand also higher local hydrogen concentrations can be reached. An example for an IG crack propagation in alloy 725 is depicted in Fig. 2-4, where Lu et al. [56,57] compared the cracking behaviour of alloy 718 and 725 with slow strain rate tensile test (SSRT) in hydrogen charged and uncharged condition.

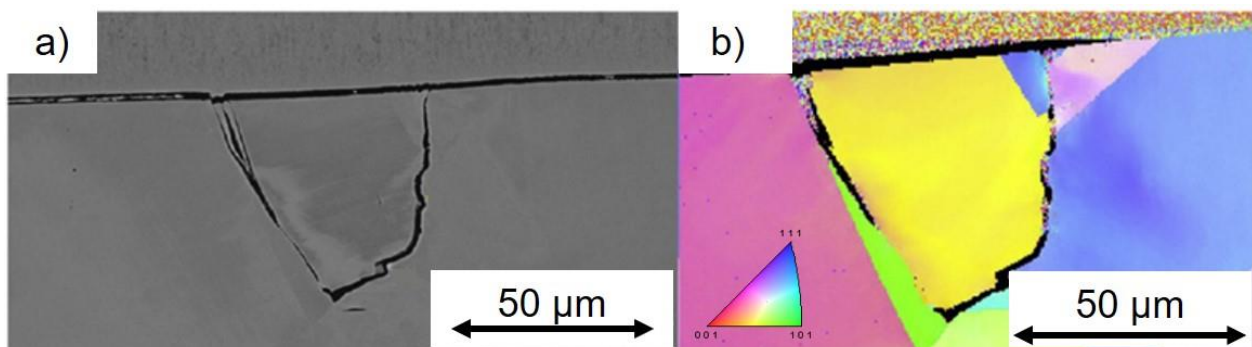


Fig. 2-4: Example for IG in alloy 725; a) scanning electron microscopy (SEM) picture; b) inverse pole figure (IPF) map from electron backscatter diffraction (EBSD), adapted from ref. [56].

Also previous publications, already reported the IG cracking for alloy 718, starting with tensile tests on notched and unnotched sample conducted by Liu et al. [58,59]. Beside the loss of

reduction of area, which was chosen to quantify the susceptibility to HE, they found a deleterious effect of the presence of the δ phase. This influence of the δ phase was confirmed by various other researchers through SSRT. Demetriou et al. [60] saw that especially coarse δ phase can assist the IG cracking, by promoting micro-crack formation. Furthermore, the interface between γ - matrix and δ phase can accumulate higher hydrogen concentration due to local stresses and promote the crack initiation [61]. In general, all types of precipitates and phases which are present at the GB have unfavourable influence on the resistance against HE, e.g. the recently discovered F-phase [56,62].

Additionally, to precipitates at the GBs, also the type of GBs has a big influence on the HE susceptibility. For nickel-base alloy 725 it was found by Seita et al. [63], that coherent twin boundary are most susceptible to crack initiation in the presence of hydrogen. In contrast, Hanson et al. [64] have focused on the GB type with highest resistance and found boundaries with low-index plane (low Miller index facet e.g. {001}, {011}, or {111} of at least one neighbouring grain) show the best performance. Furthermore, Lu et al. [57] proposed the STRONG (Slip Transfer Resistance of Neighbouring Grains) model, which states that GBs with a low ability for dislocation transmission are more prone to HE.

TG cracking

Beside IG cracking along the GB also TG cracking occurred in some of the before mentioned studies. TG cracking was mainly observed at slip band intersections and was associated with shear localization due to HELP [57,61]. Coherent precipitates promote planar slip on slip planes which are easy to glide, e.g. {111} for fcc materials. Hydrogen further impede the cross-slip of dislocations by lowering the stacking fault energy and therefore additionally enhances planar slip. By accumulation of hydrogen at crack tips or slip bands the combination with plastic deformation leads to vacancy formation and subsequently TG cracking [65].

This literature review elucidated, that beside of the embrittling character also plastic deformation plays an important role in the failure mechanisms for HE. Nevertheless, GBs and their strength are still essential research field for improving material resistance against HE. Beside avoiding unfavourable phases, also the reinforcement of GB through, e.g. segregating elements,

is a possible solution approach. Therefore, in the next section GB segregation is examined from theoretical and experimental points of view.

2.3. Grain boundary segregation

The mechanical properties of polycrystalline materials are highly influenced by the characteristics of the GBs. Therefore, grain boundary engineering (GBE) became popular method for tailoring material properties over the last decades. Different approaches are available to e.g. enhance strength, improve corrosion resistance or to reduce the sensitivity to HE. On the one hand the GB type can be deliberately influenced by increasing the fraction of low-angle GBs or special GBs (e.g. twin boundaries, Σ boundaries). On the other hand a chemical approach can be chosen by controlling the chemical composition at the GB by solute segregation [66–68].

Publication C of this thesis deals with segregation-based GBE, and uses the simulation-based approach of DFT to verify the experimental data of APT and vice versa. The next paragraphs will introduce the necessary fundamentals of GB segregation.

Equilibrium and grain boundary segregation

Equilibrium segregation denotes the accumulation of foreign atoms with high mismatch and low solubility in the bulk to energetic preferable sites, which exhibit a higher distortion than the matrix as e.g. GBs, to reduce the energy of the alloy system. If the energy can be reduced via this thermodynamically preferred process, a thin layer of alloying or impurity elements segregates to the GB. In contrast to GB precipitates, where a second phase is formed, for GB segregation the elements are present in solid solution, and this consequently leads to changes of the chemical composition when compared to the matrix [69,70].

Such segregation processes can be described through different model approaches. The most noted is the Langmuir-McLean isotherm, which is based on classical thermodynamic approaches and describes the formation of a monolayer of the segregating element [71]. For more complex tasks as multilayer or solute-solute segregation the models by Seah and Hondros [72] or the Fowler-Guttman [73,74] model can be consulted. Especially for technical relevant multicomponent systems not only one segregation element is present, which demands the

consideration of site competition and so-called co-segregation phenomena, which was first considered by Guttman and McLean [75].

Since experimental (e.g. APT) and simulation-based (e.g. DFT) approaches operate at different scales in regards of time and length, it is necessary to keep in mind the limitations of each method when establishing a quantitative comparison. When including the before mentioned site competition and also the kinetic extension to the McLean model, the obtained segregation energies from DFT and the experimentally measured bulk composition, can be combined to compare the GB enrichment after a certain heat treatment [76,69].

Segregation characterization with atom probe tomography

For the experimental determination of the chemical composition at GBs, which enables further analysis of the segregation tendency, different experimental methods are available. These methods can be divided into surface analysis and microscopic and tomographic methods. Auger electron spectroscopy and secondary ion mass spectroscopy (SIMS) belong to the surface sensitive techniques. These two methods are not in the scope of this thesis and therefore are not discussed in detail. Nevertheless, these techniques were already successfully used in the past on nickel-base alloys [77–80].

The microscopic and tomographic methods include APT and transmission electron microscopy (TEM). TEM in combination with tools like energy disperse X-ray analysis or electron-energy loss spectroscopy (EELS) can provide the GB chemistry additionally to crystallographic information. The drawbacks of this technique are detection limits for small segregation amounts due to limited chemical sensitivity as well as a difficult sample preparation for brittle materials [69]. In contrast, APT can detect already lowest amounts of segregating element due to the high chemical and spatial resolution. The spatial resolution has an accuracy of 0.3 nm in lateral direction and 0.2 nm in depth. The chemical sensitivity lies around 10 to 20 ppm [81,82]. Therefore, this method is perfectly suitable for investigating GB segregation and was the method of choice for the experimental investigations reported in Publication C. The targeted and site-specific sample preparation for GBs by means of focused ion beam (FIB) milling is indispensable for this measurements. Therefore, the next paragraphs deal with the basics of sample preparation, measurement principle and advanced evaluation possibilities for APT.

The measurement principle of APT is schematically depicted in Fig. 2-5, and shows the required sample geometry and necessary electrode and detector. In principle the atoms of a needle-shaped sample with a tip radius of only a few 100 nm are successively separated one by one from the tip surface and are accelerated to a position-sensitive detector. For this the needle-shaped sample is cooled down to cryogenic temperatures around 20-100 K and applied with a voltage of 2-20 kV in an ultra-high vacuum chamber. The applied voltage generates an electrical field F on the apex of the sharp tip, which follows the equation,

$$F = \frac{V}{k_f R}, \quad (11)$$

and therefore is depending on the applied voltage V and the tip radius R . The field-factor k_f is responsible for accounting the tip shape and ongoing blunting during the measurement.

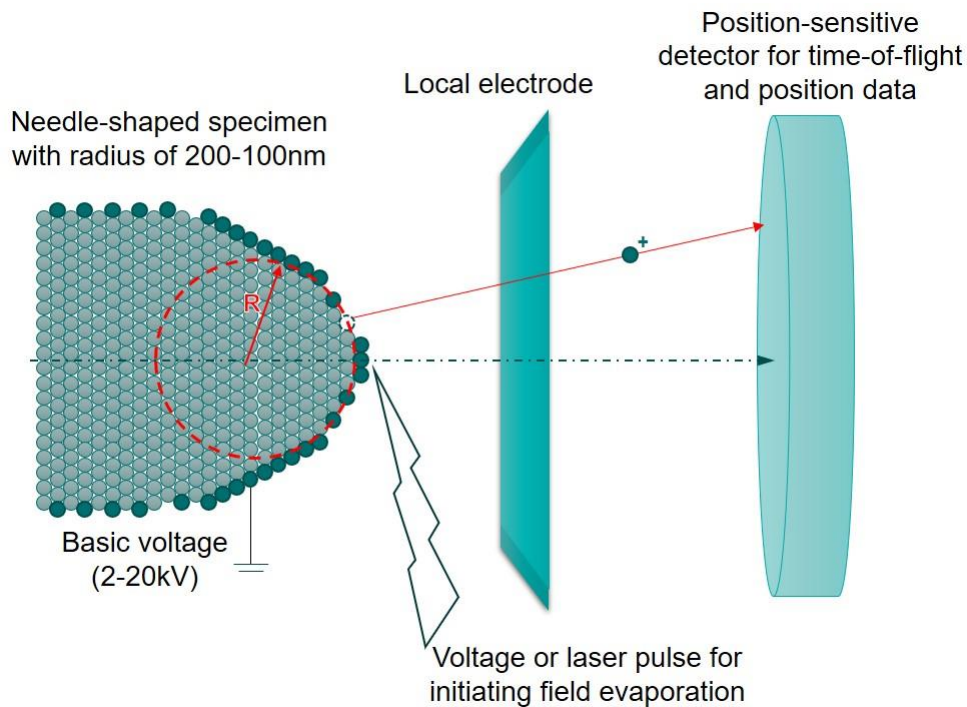


Fig. 2-5: Measurement principle of APT, redrawn from ref. [81].

Additionally, to the basic voltage periodical pulses are applied, either by voltage or laser, to emit out electrons of the surface atoms by a tunnelling process. This leaves behind positively charged ions, which can leave the sample surface and are further accelerated towards the counter

electrode and the detector. This process is called field evaporation, and is triggered by either thermal (for laser mode) or electric (for voltage mode) pulses.

Each mode has his advantages and disadvantages and must be carefully chosen for the investigated material. For the voltage mode, the sample has to be electrically conductive and fracture events are more likely especially for brittle material, due to cyclic mechanical induced stresses due to voltage pulses. The laser mode in contrast can be applied for weak or even non-conductive materials, because the field evaporation is achieved by increasing the temperature of the tip by laser pulses instead of voltage. Since the laser is directly focused on the apex of the tip the mechanical induced stresses are relatively low and fracture is less likely and qualifies this mode for fragile materials. Although, the temperature increase is induced through a sharp pulse the cooling down occurs gradually due to the confined thermal conductivity and the small cross-section of the sample [83]. This results in a loss of mass resolution and pronounced tails in the mass spectra, which is the basis for the subsequent data evaluation.

Once the ions are evaporated from the tip surface, they are accelerated toward the local electrode and are collected by a position-sensitive detector system, which provide the X and Y position for the reconstruction. The Z position is achieved from the evaporation sequence. The only missing information for a full 3D reconstruction of the tip is the chemical information of each collected ion. This is achieved through so-called time-of-flight (TOF) spectroscopy, which measures the flight time of the ion from the sample to the detector. This time depends on the mass of the ion, therefore lighter ions have a higher velocity and thus have a shorter TOF, than heavier ones. When correlating this TOF with the conservation of energy state, which imply that the potential energy ($E_{pot} = neV$) of the ion is equal to the kinetic one ($E_{kin} = \frac{mv^2}{2}$), the mass-to-charge ratio is obtained by [83]:

$$\frac{m}{n} = \frac{2eVt^2}{L^2}, \quad (12)$$

with, m and n as the mass and the charge state of the ion, e the elemental charge, V the operating voltage, t the TOF and L the real flight length. With this information the mass spectrum can be build and the assignment of the different peaks allows the assignment to the chemical species [81,84].

Over the last years the measurement devices (detectors) as well as the data analysis was further developed and improved. Nevertheless, lots of issues, which can distort the results, must be kept in mind, e.g. multiple hit detection, peak overlaps or preferential evaporation. A further drawback of this technique is the low detector efficiency (between 38 and 80%) and the small sample volume of just several hundred of nm³. Nevertheless, it is perfectly suited to for chemical investigation of GB segregation, since the chemical concentration differences occur on the scale of a few nanometres. For this a site-specific preparation method is vital, as with the classic electrochemical polishing procedure it is not possible to prepare and adjust specific boundaries. The next paragraphs will thus describe the lift-out technique in a dual beam scanning electron microscopy (SEM)/FIB workstation.

This technique was first proposed by Miller et al. [85] and further developed by Felfer et al. [86] and refined with transmission Kikuchi diffraction (TKD) by Leitner et al. [87,88]. An exemplary preparation procedure is depicted in Fig. 2-6. First of all, the preferred GB is chosen in the SEM via standard electron backscatter diffraction (EBSD) analysis as visible in Fig. 2-6a-b with secondary electron (SE) contrast and IPF image. Afterwards a lamella at the desired position is coarsely milled via FIB with high ion currents around 8 nA and afterwards lifted-out with a micro-manipulator (Fig. 2-6c-d). Right after positioning on a molybdenum-based grid with Pt-deposition the pyramidal and annular milling with probe currents around 100 pA to 3 nA can be conducted as shown in Fig. 2-6e-f. For an accurate positioning of the GB, within the first 100-200 nm of the apex of the tip, the last fine-milling steps are alternated with TKD measurements. Further details regarding the TKD procedure and the gun and detector arrangement for this analysis the reader is referred to ref. [87].

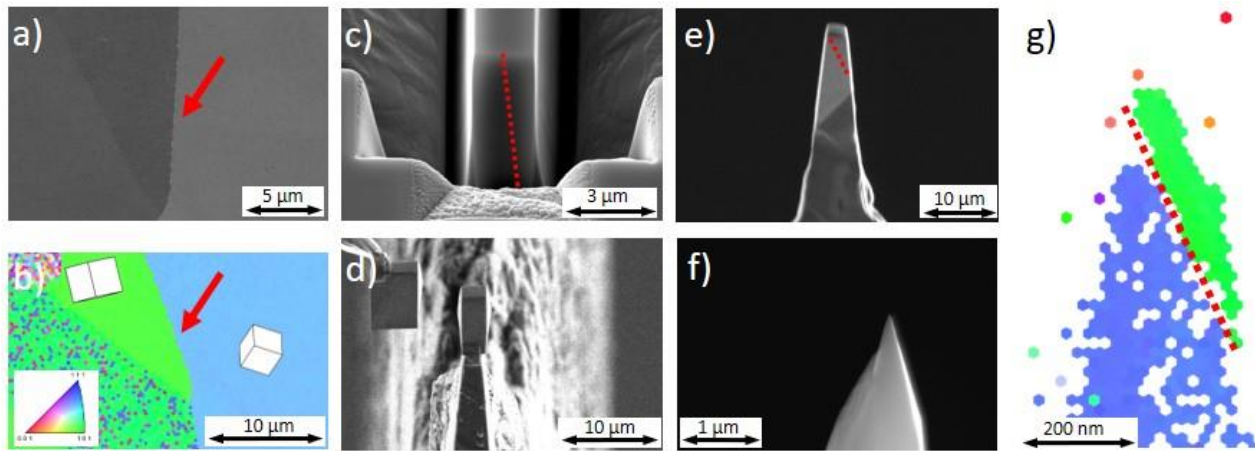


Fig. 2-6: Process route for the lift-out of an APT tip adapted from ref. [89]. For detailed explanation see text.

After successful sample preparation, APT measurement and data evaluation a cylindrical region of interest (ROI) perpendicular to the GB plane can show some first segregation tendencies in the concentration profile as shown in Fig. 2-7a-b. For a more profound and quantitative analysis the interfacial excess (IFE) evaluation based on the Gibbsian interfacial excess value initially outlined by Krakauer and Seidman [90] is a preferred method. The first application to APT data was done by Thuvander et al. [91] and Hellman et al. [92].

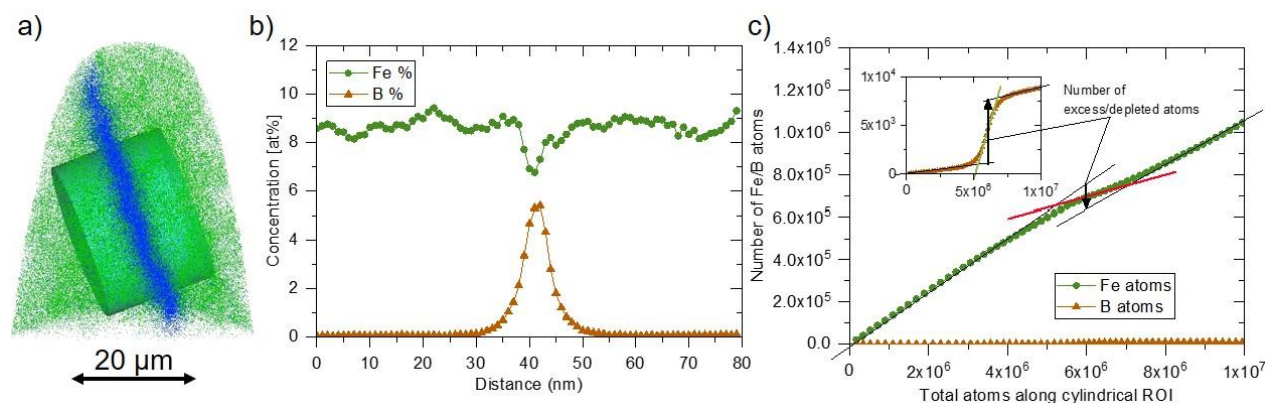


Fig. 2-7: a) Cylindrical region of interest (ROI) in APT tip with nickel and boron atoms; b) concentration profile; c) IFE analysis via ladder diagrams adapted from ref. [89].

The cylindrical ROI, which is also used for compiling a concentration profile, serves as a basis for the generation of the so-called Ladder diagram as illustrated in Fig. 2-7c. For this purpose, the ROI is divided into small segments and the number of atoms is summed up

continuously. Afterwards the number of a specific atom (y-axis) is plotted against the total number of atoms (x-axis). This leads to a linear behaviour for a non-segregating and evenly distributed element species. For an element which segregates to the GB, as boron in the example, a distinct increase in the slope of the curve is visible. In contrast a depletion is manifested in a decreasing slope, as for iron. When the number of excess or depleted atoms is related to the area of the cylinder the IFE value is obtained with atoms/nm² and can be quantitatively compared for evaluation of the GB segregation tendency.

Since HE is often related to IG failure at GBs the knowledge of segregating elements can be combined with different other investigation approaches, as for example simulation-based segregation prediction as reported in Publication C. Furthermore, these segregation tendencies can be used in future in combination with the Rice-Wang theory [93] of GB embrittlement for forecasting the influence on the cohesive strength and therefore can serve as an important tool for GB related investigations of HE [33].

2.4. Nanoindentation

Instrumented indentation testing, also known as nanoindentation, was developed from the classical hardness testing in the late 70s to the early 80s. The most popular methods of classic hardness testing such as Vickers [94] or Brinell [95] are using the diameter of the projected area of the remaining imprint as a measure for calculating the hardness, whereas the Rockwell [96] method uses the remaining penetration depth. Nanoindentation, in contrast, obtains the necessary parameters indirectly from recording the load over the penetration depth during the indentation process. The first attempt to implement such an instrumented experiment was successfully achieved by Martens et al. [97]. As a consequence, the optical measurement became now dispensable and imprints with only a few nanometres of penetration depth can be analysed to calculate the mechanical properties of small sample volumes and single microstructural features. A detailed explanation and application of this capable method will be illustrated in the following sections.

2.4.1. Conventional Nanoindentation

Generally, the testing principle is based on the indentation of a sharp, hard and stiff tip into a material. The force and penetration depth, respectively, are recorded by means of high-precision electronics during both, loading and unloading. The most commonly used geometry for the indenter tip is a so-called Berkovich pyramid, which is a three-sided pyramid illustrated in Fig. 2-8a. A typical load-displacement curve, with all necessary measurement parameters, is shown in Fig. 2-8b. This load-displacement curve can be analysed according to the method established by Oliver and Pharr [98] in the year 1992 to calculate the hardness H and the Young's modulus E from the contact depth.

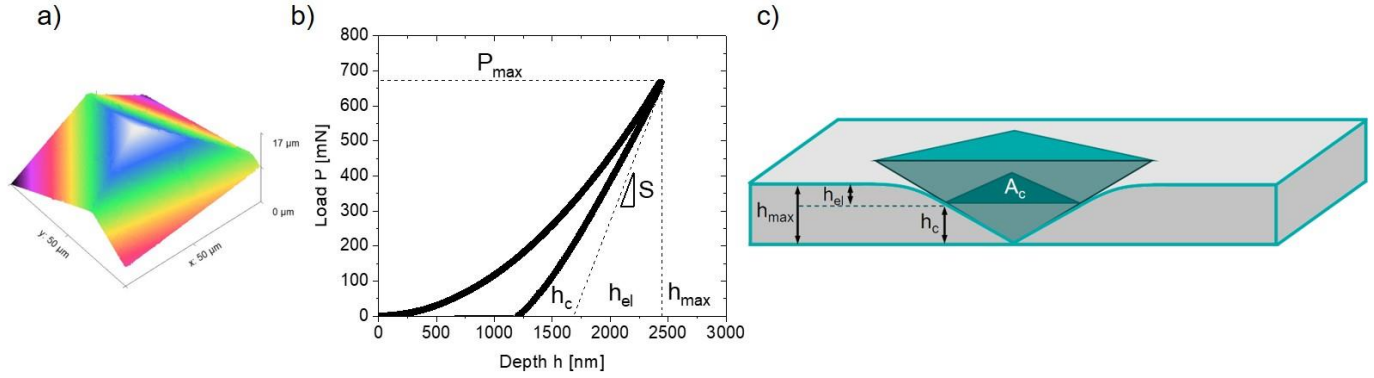


Fig. 2-8: Brief nanoindentation overview; a) laser scanning confocal microscopy (LSCM) image of the commonly used Berkovich tip; b) exemplary load-displacement curve; c) schematic tip during indentation process and surface profile under load.

The necessary parameters for this analysis, which can be directly extracted from the diagram are the maximum load P_{max} , the maximum penetration depth h_{max} as well as the contact stiffness S , at the point of unloading. The first part of the calculation to obtain hardness H and Young's modulus E is the determination of the actual contact depth h_c by subtraction of maximum depth h_{max} and the elastic recovery h_{el} .

$$h_c = h_{max} - h_{el}. \quad (13)$$

In contrast to h_{max} , which is directly visible in the load-displacement curve, the elastic recovery h_{el} is derived from Sneddon's contact model [99] for conical tip geometries and follows the equation:

$$h_{el} = \varepsilon \frac{P_{max}}{S}. \quad (14)$$

Thereby ε is a geometry factor depending on the indenter shape and account for 0.75 for a parabolic shape, like the Berkovich tip.

For obtaining the contact area A_c as a function of contact depth h_c (see Fig. 2-8 c) a calibration of the indenter geometry on a material with well-known mechanical properties is required. In most cases a fused silica sample with a Young's modulus $E = 72 \text{ GPa}$ is used due to its isotropic mechanical properties. Subsequently, the contact area A_c is described with a polynomial fit according to:

$$A_c(h_c) = a_0 h_c^2 + a_1 h_c + a_2 h_c^{1/2} + a_3 h_c^{1/4} + a_4 h_c^{1/8} + \dots, \quad (15)$$

whereas a_0 is an indenter tip dependent geometry parameter and can be correlated to the opening angle and results in a value of 24.5 for a perfect Berkovich tip. The further fitting parameters a_i account for imperfection of the tip geometry.

With the depth-independent geometry factor β , which is 1.034 for a Berkovich tip, all necessary parameters are present to calculate hardness H and the reduced modulus E_r according to equation (16) and (17) at the point of unloading:

$$H = \frac{P_{max}}{A_c(h_c)} \quad (16)$$

and

$$E_r = \frac{\sqrt{\pi}}{2\beta} \frac{S}{\sqrt{A_c(h_c)}}. \quad (17)$$

When knowing the Young's modulus E_i and Poisson's ratio ν_i of the indenter tip, as well as the Poisson's ratio of the material to be tested, the reduced modulus can be translated into Young's modulus E of the material:

$$\frac{1}{E_r} = \frac{1 - \nu^2}{E} + \frac{1 - \nu_i^2}{E_i}. \quad (18)$$

Based on this approach invented by Oliver and Pharr the nanoindentation technique has developed over the past 25-30 years and has become a versatile tool in materials science and is indispensable for testing mechanical properties at the local nanoscale.

2.4.2. Advanced nanoindentation methods

Over the years, the method has been continuously refined by both, the researchers themselves and by nanoindenter manufacturers. An important milestone was achieved when dynamic measurement protocols enabled the continuous stiffness measurement (CSM) over the indentation depth [100–103]. By overlaying a sinusoidal force signal over the continuously increasing load, every cycle of this oscillation represents a small unloading point where the stiffness can be determined by recording the displacement amplitude and the phase angle. As a

consequence, nanoindentation can be extended to a depth sensing method and therefore provides information about gradients in elastic and plastic response within the whole indentation depth. Nevertheless, this technique must be applied carefully, since unfavourable combinations of a slow CSM signal and a high E/H ratio of the investigated material can lead to significant plasticity errors, as figured out by Merle et al. [104].

Nevertheless, a broad field of advanced methods established due to the development of CSM technique, which e.g. allows to investigate thermally activated deformation processes through investigation of the strain rate dependent material response. Therefore, the method of nanoindentation strain rate jump tests introduced by Maier et al. [105], which is a relevant method for this thesis is explained in the following paragraphs.

First of all, two different loading scenarios can be defined and distinguished for an indentation experiment. The first one is applying a constant load rate (cLR) \dot{P} . For this purpose, the load P is linearly increased until a preset maximum load and the hardness and Young's modulus are calculated according to the Oliver-Pharr method in the point of unloading. The loading can be partially divided in a preset number of unloading steps. The strain rate $\dot{\epsilon}_i$ in each of this unloading points only depends on the loading time Δt for a maximum unloading of $a = 100\%$ and follows the equation:

$$\dot{\epsilon}_i = \frac{\dot{P}}{P} = \frac{1+a}{2\Delta t}. \quad (19)$$

Since the only parameter which needs to be controlled is the applied load, this method is easy to implement and controllable in most nanoindentation system. This method can also be combined with proportional unloading steps, to obtain a certain number of points within the indentation depth.

The second loading scenario are experiments with a constant strain rate (cSR). In special combination with CSM technique this loading type is perfectly suitable for investigation of plastic deformation behaviour at a constant strain rate. For this kind of tests, instead of the maximum load the maximum penetration depth and a strain rate are predefined (depending on the manufacturer). According to work of Lucas and Oliver [106] the indentation strain rate can be described:

$$\dot{\varepsilon}_i = \frac{\dot{h}}{h} = \frac{1}{2} \left(\frac{\dot{P}}{P} - \frac{\dot{H}}{H} \right) \approx \frac{1}{2} \frac{\dot{P}}{P}. \quad (20)$$

This possibility of conducting a cSR experiment with an appropriate loading protocol opens the possibility to implement the advanced nanoindentation method of strain rate jump tests [105].

The strain rate jump test is a special form of an cSR experiment with an abrupt change in the strain rate during the indentation process. This alteration in strain rate results in a corresponding jump in the recorded hardness data for a strain rate sensitive material. In contrast to the hardness, the Young's modulus should not be affected by the applied strain rate. Fig. 2-9 exemplary summarizes all important parameters applied and recorded during this testing procedure. Due to changing the strain rate in a single experiment this technique has big advantages regarding thermal drift due to reduced indentation time. Furthermore, it requires lower sample volumes and limited preparation as well as time effort compared to macroscopic experiments with, however, uniaxial stress state (like tension or compression test). Still a remaining comparability of the results is given.

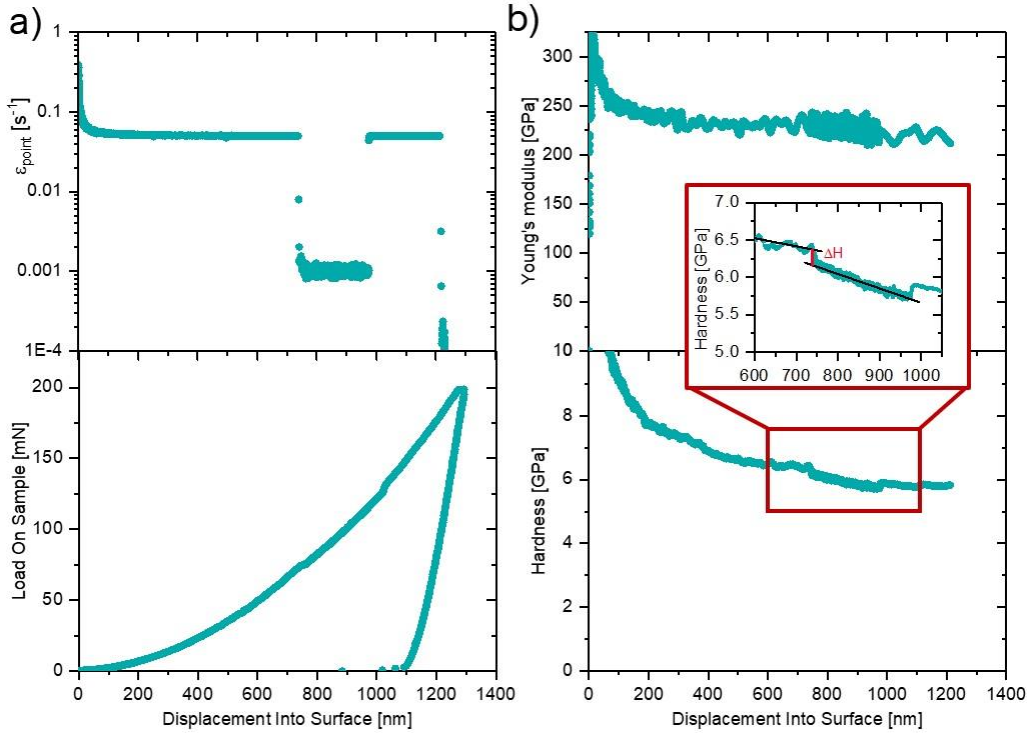


Fig. 2-9: Nanoindentation strain rate jump tests for a nickel-base alloy 725; a) applied strain rate and load-displacement curve; b) Young's modulus and hardness with insert of hardness jump in detail.

From the occurring change in hardness (see insert in Fig. 2-9b) the plastic deformation related parameters of strain rate sensitivity m and activation volume V^* can be calculated according to equation (21) and (22) and can provide essential information about the acting deformation mechanism.

$$m = \frac{\partial \ln \sigma}{\partial \ln \dot{\epsilon}} \sim \frac{\partial \ln H}{\partial \ln \dot{\epsilon}} = \frac{\partial \ln H_2 - \partial \ln H_1}{\partial \ln \dot{\epsilon}_2 - \partial \ln \dot{\epsilon}_1} \quad (21)$$

and

$$V^* = C^* \cdot \sqrt{3} \cdot k_B T \cdot \frac{\partial \ln \dot{\epsilon}}{\partial H} \sim C^* \cdot \sqrt{3} \cdot \frac{k_B T}{m \cdot H}, \quad (22)$$

whereas H_1 and H_2 are the hardness values before and after each jump, respectively. For calculation of the activation volume the constraint factor C^* with 2.8 [107], the Boltzmann constant k_B and the absolute temperature T in Kelvin are furthermore required.

The existing deformation mechanisms can be listed as follows and exhibit different ranges for strain rate sensitivity m and activation volume V^* :

- Peierls-Nabarro mechanism
- Dislocation-dislocation interaction
- Forest hardening

The acting mechanism is highly influenced by the crystal structure, grain size and temperature. Chemically pure coarse grained fcc metals are insensitive to strain rate changes and exhibit a strain rate sensitivity close to zero. This is coupled with an activation volume around $100-1000 b^3$, where b denotes the Burgers vector, and indicates plastic deformation through forest hardening [108,109]. Due to a pronounced thermally activated stress contribution at low temperatures materials with bcc crystal structure show a contrary behaviour. They exhibit a pronounced sensitivity in hardness due to strain rate changes, which is accompanied with a higher strain rate sensitivity and activation volumes between $1-10 b^3$, indicating a so-called Peierls-Nabarro mechanism [110,111], which is based on the motion of screw dislocation. The transition between those mechanisms is dominated by dislocation-dislocation interaction.

2.4.3. Electrochemical nanoindentation

Electrochemical setups

Starting in the year 2006, nanoindentation found its way into the research area of hydrogen-material interactions. Barnoush and Vehoff [112,113] introduced the first electrochemical cell, which was implemented in a Hysitron triboscope, and were able to conduct the first nanoindentation tests with in-situ charging.

The cell was designed as a top-charging concept, which means charging is performed from the same side as the nanoindentation measurement. As a consequence, indentation tests are done through the liquid electrolyte and a tip with an elongated shaft is needed. A schematic drawing of the first prototype of the electrochemical cell is shown in Fig. 2-10a. It was made out of PTFE, to ensure chemical resistance against a variety of different electrolytes and equipped with a Ag/AgCl reference electrode and a platinum wire to complement the three-electrode setup, which is needed for potentiostatic charging of the sample material. The electrolyte was

inserted with a microfill pipet. This type of setup was used for several years by different researchers and research groups [114–117].

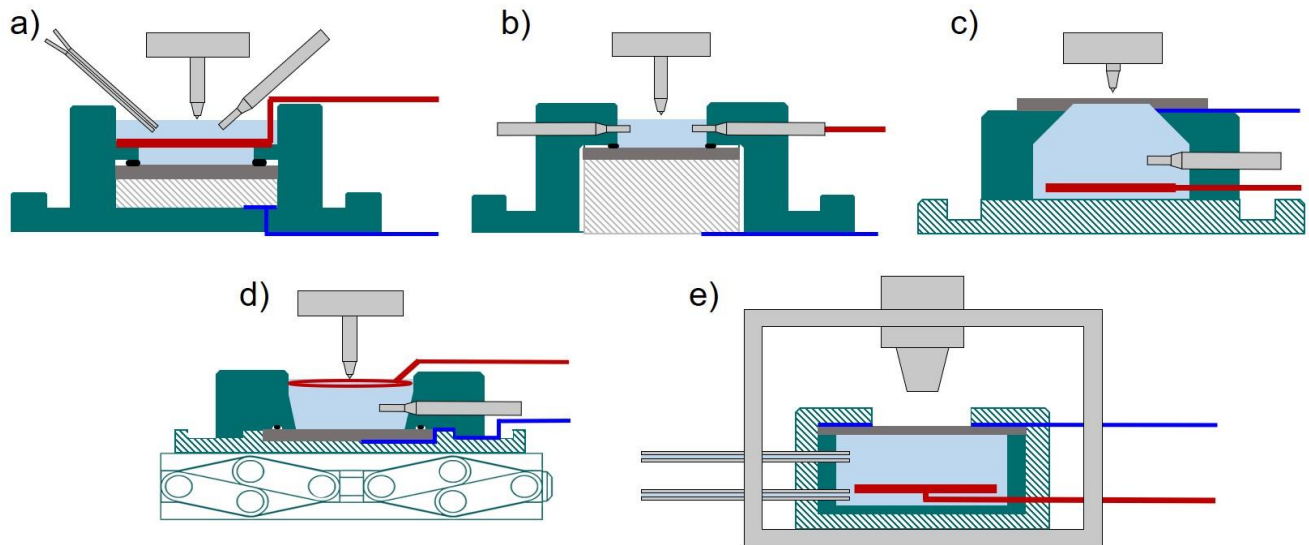


Fig. 2-10: Schematic representation of different in-situ electrochemical setups for nanoindentation; a) first top-charging approach by Barnoush et al. [112]; b) adapted top-charging for battery materials by Epler et al. [118]; c) back-side charging developed by Duarte et al. [119]; d) modified top-charging cell implemented during this thesis [55]; e) in-situ setup for application in a SEM with back-side charging by Kim et al. [120].

The first electrochemical setup, which was developed for the G200 nanoindenter platform (KLA Tencor, former Keysight Aglient) was mentioned in the thesis of Epler [118], and is depicted in Fig. 2-10b. In contrast this setup was used for studying the degradation of battery electrode materials during repeated charging cycles. Nevertheless, the concept of front-side charging stayed the same. For both of this front-side approaches the sample was mounted from below. To overcome the disadvantage of the missing movement of the stage in z-direction, a stepper motor driven lifting table was implemented. This strategy served as template for the stage built up within this thesis, which is schematically depicted in Fig. 2-10d, and is described in further detail in section 3.

Additionally, to the in-situ charging during nanoindentation efforts were made to enable the implementation of an electrochemical setup into a SEM for continuous imaging during charging and indentation, this was successfully fulfilled by Kim et al. [120]. The main difficulties

for implementation in a SEM are the necessity for absolute leakproofness for maintaining a good vacuum. Therefore a back-side charging approach was chosen and is depicted in Fig. 2-10e. For this setup the electrolyte is filled into a closed reservoir on the bottom side of the sample and investigations are made on the opposite side. Therefore, the absorbed hydrogen must diffuse through the sample to the testing surface of the sample. As a consequence, the sample thickness must be adjusted to the diffusibility of hydrogen for the tested material to guarantee practical charging time. A drawback of this modification is the reduced stiffness, due to the reduced sample thickness of a few hundred μm , which can negatively influence stiffness related nanoindentation results.

Nevertheless, similar back-side charging approaches outside the SEM (Fig. 2-10d) are still employed by different research groups. Due to the low sample thickness of 200 μm and the resulting loose in stiffness the investigations by Müller et al. [121] on pure polycrystalline focused on the analysis of the initial pop-in, which is explained later in more detail. Duarte et al. [119] provided a well elaborated comparison of the advantages and disadvantages of the front and back-side charging setups.

Analysed parameters

With all these various types of setups classical nanoindentation test can be performed to investigate the sensitivity to hydrogen charging for manifold materials. The first experiments of Barnoush [113] were conducted on a nickel single crystal with (111) orientation. The analysis focused on the pop-in, which occurs at the transition from fully-elastic to elastic-plastic deformation in the load-displacement curve visible through a sudden burst in displacement. This first few nanometres of a load-displacement curve with a pronounced pop-in is depicted in Fig. 2-11a. According to literature this pop-in can be correlated to a homogeneous dislocation nucleation (HDN) under the indenter tip in a quasi-dislocation free material [122], and its origin is schematically illustrated in Fig. 2-11b. This quasi-dislocation free condition only holds true for coarse-grained material states with a low intrinsic “defect” density (e.g. dislocation, precipitates, inclusions). If this requirements are fulfilled the pop-in load correlates with the radius R of the used tip and the maximum shear stress of the material according to:

$$\tau_{max} = 0.31 \left(\frac{6E_r^2}{\pi^3 R^2} P_{Pop-in} \right)^{1/3}, \quad (23)$$

The decrease in the pop-in load, which is attributed to the hydrogen charging is explained by Barnoush in first works [112,113] by hydrogen reducing the lattice cohesion, which results in a facilitated dislocation nucleation under the indenter tip. In his future works [25,117,123] he further proposed with his experiments, a combined HEDE and HELP mechanism, which operates by weakening of the interatomic bonds by a reduction of the shear modulus or the stacking fault energy.

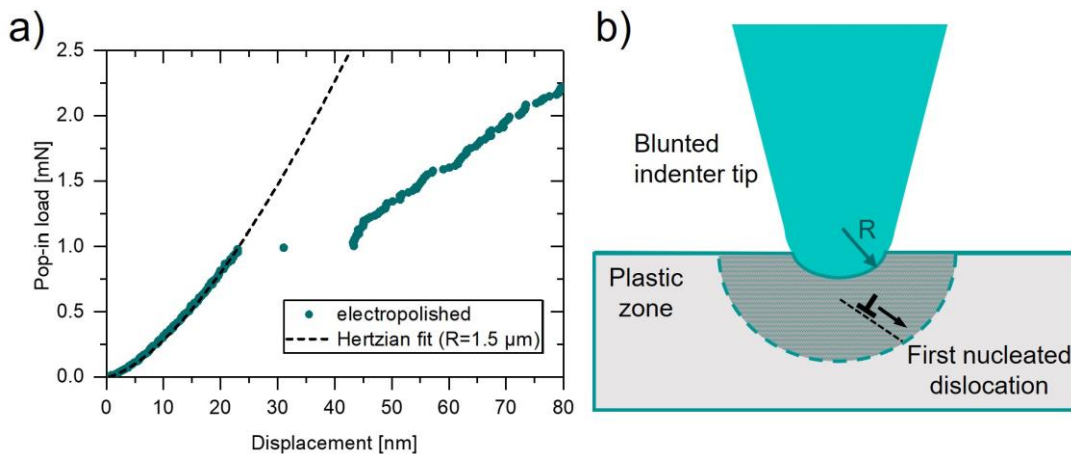


Fig. 2-11: Overview of pop-in formation; a) load-displacement curve with pronounced initial pop-in for an electro-polished nickel-base alloy with conical tip (specified radius 2 μm); b) schematic illustration of blunted indenter tip with radius R and first nucleated dislocation in the subsequently developed plastic zone.

In 2012 the parameters investigated through electrochemical nanoindentation were further extended by measurement of the hydrogen-induced hardness increase on an austenitic steel [116]. Beside the pop-in analysis this hydrogen-induced hardness increase became a fixed part of the electrochemical nanoindentation. Furthermore, the technique was applied to many different material classes e.g. nickel-base alloys [124], iron [125], steels [126,127] and also HEAs [128–130]. These measured hardness increase is explained by a decreased dislocation mobility, an increased lattice friction between dislocations and hydrogen and solid solution hardening contributions.

Further Applications

Beside the classical and its advanced evaluation methods, nanoindentation tools can also be used for micromechanical approaches for pillar and cantilever testing. Initial experiments were performed on FIB cut FeAl micro pillars [131]. Further tests on hydrogen charged bi-crystalline pillars were published by Kheradmand et al. [132] on coarse grained nickel later on in 2012. Lu et al. [133] conducted a much more profound analysis of the influence of hydrogen on the slip transfer through a GB in a nickel-base alloy 725, with detailed post-mortem investigations.

Since HE is often ascribed to brittle GB fracture micro cantilever bending can exploit the crack initiation and propagation under hydrogen influence [134,135,44]. Such micro cantilever tests were also performed by Deng et al. [136] in an environmental SEM for revisiting the hydrogen-enhanced cracking of FeAl.

3. Implementation of the electrochemical setup

Since the implementation and further development of the electrochemical setup is a main part of this thesis the following chapter should give an elaborated summary of this process. First of all, the used nanoindenter system will be introduced. Furthermore, the development of the cell design as well as the implementation process will be elucidated in further detail. Finally, the combination of electrochemical charging and nanoindentation will be highlighted and possible issues and challenges during application are discussed. The most essential contents of this process are summarized in Publication A.

3.1. The nanoindentation platform

For determination of the nanomechanical properties and the implementation of the electrochemical setup a G200 nanoindenter (KLA Tencor, Milpitas, USA) with XP head served as a platform (see Fig. 3-1a). The conventional build in XP-head can operate with the advanced CSM signal, which is described in section 2.4.2 in more detail. The CSM opens a variety of possibilities in contrast to prior cell designs incorporated in former Hysitron systems. The G200 enables indentation tests up to at least a load of 500 mN with a maximum vertical travel length of around 1.5 mm. The theoretical force resolution is stated by the manufacturer to be 50 nN, the theoretical displacement resolution with 0.01 nm, respectively. The force application is accomplished through electromagnetic induction. By measuring the capacitive change with a capacitor system, the vertical displacement can be determined with high accuracy. However, when taking into account the signal-to-noise ratio the achievable resolution is in the range of 1 nm. In general, this system belongs to the group of force controlled indenter systems, which allows an accurate performance of force and strain rate controlled methods to a given displacement. A feature, which is especially necessary for the implementation of the electrochemical cell is the excellent overall stiffness, achieved through the rigid and robust frame of the platform. Furthermore, this frame is located on a passive damping table (company: Minus-K technology), which perfectly supports the sensitive measurements through the electrolyte.

3.2. Cell design

A central part of this thesis was to create an improved electrochemical cell design for the G200 platform, with regard to the already existing systems known from literature at the beginning of this thesis [112,118]. This enhanced design must fulfil some requirements, which are briefly presented in this section. The finalized electrochemical cell is illustrated in Fig. 3-1, where b) shows the schematic drawing and c) depicts the cell inside the nanoindenter chamber.

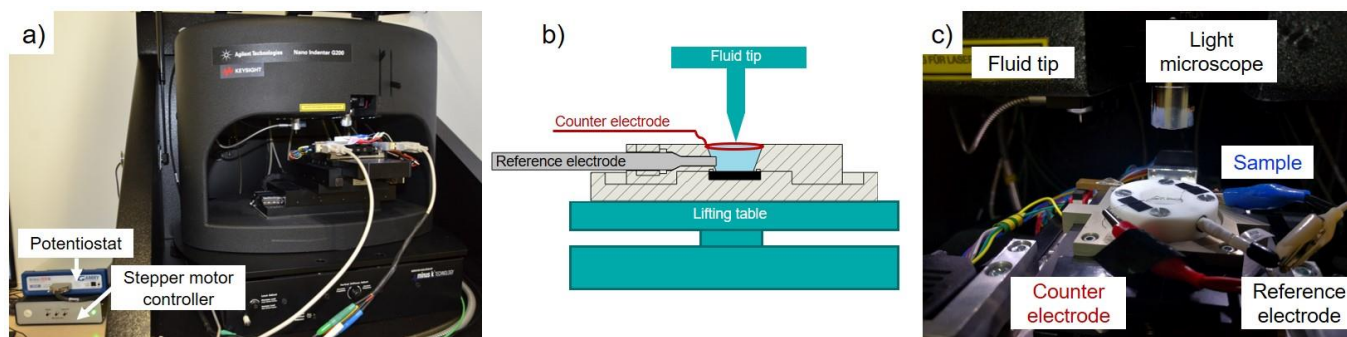


Fig. 3-1: Electrochemical nanoindentation setup; a) G200 platform; b) schematic drawing of cell design; c) photograph of cell inside the indenter chamber adapted from ref. [55].

The electrochemical cell should be designed in a manner, that the sample is completely covered by the liquid electrolyte inside the reservoir. The electrolyte reservoir itself must be deep enough to accommodate reference electrode and counter electrode, and still allowing the fluid tip with an elongated steel shaft of 11 mm to reach the sample surface. Therefore, the electrolyte reservoir resulted in a total depth of 8 mm with some clearance for the displacement of the tip. Furthermore, this low height of the reservoir allows the use of the standard objective lens, and no objective with a shortened housing is needed.

The cell itself was designed in a sandwich-like manner, where the sample is placed in between the top and the bottom plate. The top plate is made out of Teflon/PTFE, since it requires an excellent chemical resistance, but there is no need for a high stiffness. The bottom plate, in contrast, has opposite requirements, because both hardness and Young's modulus are sensitive to lacking setup stiffness. This issue was solved by machining the bottom plate out of aluminium with a higher stiffness compared to PTFE. Nevertheless, also the bottom plate must exhibit sufficient chemical resistance in case of leakage. Therefore, the aluminium plate was anodized

after machining and a basin was designed. The thin passive layer has the further advantage of electrical isolation, which is needed to prevent occurring leakage current from the potentiostat and electrodes used for the electrochemical charging.

The recess for the sample was conceptualized in a quadratic shape with an edge length of 18 mm, which brings the benefits of more simple sample cutting as compared to round sample geometries, which were used in previous cell designs [118]. If samples should be fabricated out of a solid metal piece in a round shape, the only reasonable method is wire eroding via electrical discharge machining. Since this equipment is not available in all places, the quadratic shape was considered more practical. A regular sample, which perfectly fits into the cell is depicted in Fig. 3-2. The sample thickness should be between 3 and 3.5 mm for a tight fit of the o-seal ring, which is located between sample and top plate.

For round or even irregular sample geometries a workaround was developed and the individual steps are shown in Fig. 3-2. For this purpose, the sample is cold-embedded with Epofix resin (Struers), and afterwards cut into the final shape with a convenient cut-off machine. For thin samples a screw can be applied on the backside with conductive silver paste before the embedding step to ensure a contacting possibility.

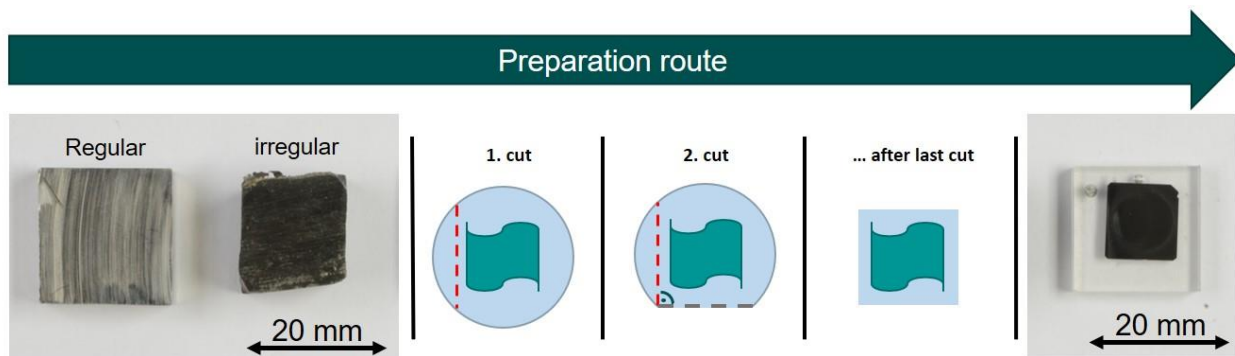


Fig. 3-2: Preparation route for irregular sample geometry. After cold embedding the sample is cut into rectangular shape.

This cell design meets all requirements to ensure a reasonable commissioning into the nanoindenter chamber. Which further adaptations had to be realized, in addition to the cell design, are described in the next section.

3.3. Implementation

Lifting Table

In normal operation mode of the nanoindenter, the sample is mounted on the x-y stage with a rigid sample holder, where the distance from the x-y stage to the indenter head is constant. The sample is mounted at an ideal height in order to guarantee a distance of approximately 0.5 mm between the parked indenter tip and the sample surface, so no movement of the sample in z-direction is necessary. This allows to move the sample laterally under the indenter head for testing different positions on a plan parallel sample. If the sample is now several mm below the surface of a liquid, the shaft of the indenter tip must be extended accordingly and the standard sample holder cannot be used anymore. To overcome the resulting height differences between cell and indenter head, the electrochemical cell must be placed on a lifting table to enable a movement in z-direction. Furthermore, it must be considered that a contact between the electrochemical cell and the indenter shaft during lateral positioning would lead to destruction of the measuring head and must be avoided by all means.

For this purpose, a lifting table of the type Mini Lab Jack L200/M (Thorlabs) was equipped with a stepper motor ST2818L1006-A with the compatible controller unit SMCI33-1 (both Nanotec Electronic GmbH & Co. KG). The control unit was self-built and equipped with buttons for three required positions (Down, Microscope, Indenter) of the lifting table. The stepper motor was fixed with a self-made connector to the lifting table. A detailed picture is shown in Fig. 3-3.

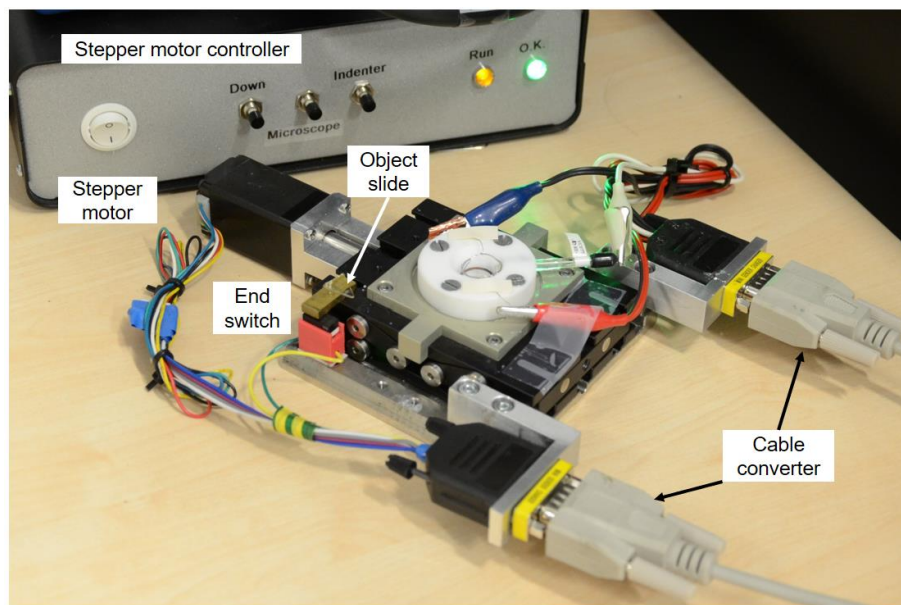


Fig. 3-3: Electrochemical cell on the lifting table with stepper motor and attached cables and switches.

Fig. 3-3 reveals some further useful features, which were attached to improve the functionality of the lifting device. A small brass bar is mounted in the rear edge of the table to press the end switch. This end switch defines the “Down” position of the table. One handicap of the lifting table, that should not be neglected is a pronounced backlash of the thread. To ensure reproducible and exact positioning, the height should always be approached from the “Down” position. Two heights for “Microscope” and “Indenter” position can be defined in the compatible Nanopro 1.7 software from Nanotec Electronics. The higher one is the “Microscope” position, which should only be approached when the cell is positioned under the light microscope objective lens. The “Indenter” position is approx. 11 mm (length of indenter shaft) lower, and serves for threading the indenter shaft inside the reservoir and positioning of the sample surface in operation range of the tip.

Electrochemical equipment

The used potentiostat is a Interface 1010B (Gamry Instruments, Warminster, USA) and can be used for a variety of electrochemical measurements. Beside simple potentiostatic or galvanostatic charging also cyclic polarization curves can be recorded. The potentiostat is

equipped with a joined cell cable, which comprises of six individual cables each of one for working and working sense, counter and counter sense, reference electrode and one grounding cable.

Cable connection

The lifting table together with the stepper motor and the end switch is mounted on a dove tail steel plate, which fits the slide-in stage of the G200 indenter. Additionally, this base plate has space for further attachments, which simplifies the cable connection of electrochemical cell and the stepper motor. For this purpose, two aluminium arms with a recess for cable converters are attached on the front side of the steel plate (Fig. 3-3). Thus stepper motor and electrochemical cell can be easily plugged in and out when inserting the cell through the small hatch of the indenter chamber.

The cables for the electrochemical cell had to be further combined before connecting them to the cable connector. The potentiostat cell cable comprise of five individual cables as described before, which then have to be attached to the sample and electrodes. Since it is tricky to clip two cables to one electrode, the cables were combined and ended with one crocodile clamp each.

3.4. Tip and tip calibration

As already mentioned for testing with the electrochemical cell special fluid compatible tips are needed. In comparison to normal indenter tips they have an elongated steel shaft of 11 mm and are purchased at Synton MDP-AG (Nidau, Schweiz). The shaft is made out of steel with the diamond tip attached at the end. The junction and the shaft are covered with an epoxy coating to ensure chemical resistance and prevent electrochemical potential differences between shaft and sample. The used tip geometries, for this thesis were a Berkovich tip (Publication B) as well as a conical tip with specified radius of 2 μm (Publication A).

Microscope to indenter calibration

The method for standard “Microscope to Indenter Calibration” (MtIC) cannot be directly used on the sample inside the cell, because the x-y stage would move without the possibility to raise or lower the lifting table. To account for this problem a small piece of a silica object slide is clued to the brass bar on the rear side (see Fig. 3-3). This reference sample can now be positioned

on the exact height for microscope and indenter. The position for calibration can be set under the microscope the “Microscope” position of the lifting table. Before starting the MtIC by pressing the NEXT-button the stage must be lowered to “Down” and “Indenter” position must be approached from below. Otherwise the lifted cell would crash the elongated tip from the side and would destroy the fragile spring system of the indenter head, where the tip is mounted. If very precise positioning is necessary, the MtIC must be repeated several times on the reference sample with decreasing “Depth into surface” in the advanced settings of the MtIC menu.

After this calibration the positions can be adjusted to the sample height and no further MtIC has to be done on the sample itself.

Tip area function calibration

For calibration of the area function of the used indenter tip the standard stage with the fused silica sample cannot be used either, due to the elongated shaft. Therefore, a workaround has to be developed for this procedure.

The reference sample, which is clued on the brass arm is also made out of silica, but the mechanical properties are not as well defined as for the fused silica sample supplied with the standard stage of the indenter. The reference sample can be used for checking the area function between individual testing sets, but is not suitable for area function calibration. For this purpose, the fused silica sample is removed from the standard stage and mounted on the dove tail steel plate with a rigid brass holder as a connector, illustrated in Fig. 3-4. The height of the brass holder is adjusted to match the exact operating position of the elongated indenter tip. In this position it is not possible to image the sample surface under the light microscope, but for area function calibration there is no need of imaging the remaining imprints. With this modified setup the area function can be determined equal to the standard procedure. For verifying the accuracy, the results for the fused silica sample ($E = 72 \text{ GPa}$, $\nu = 0.17$) with a standard Berkovich and an elongated tip (Hydrogen-Berkovich) are compared in Fig. 3-4.

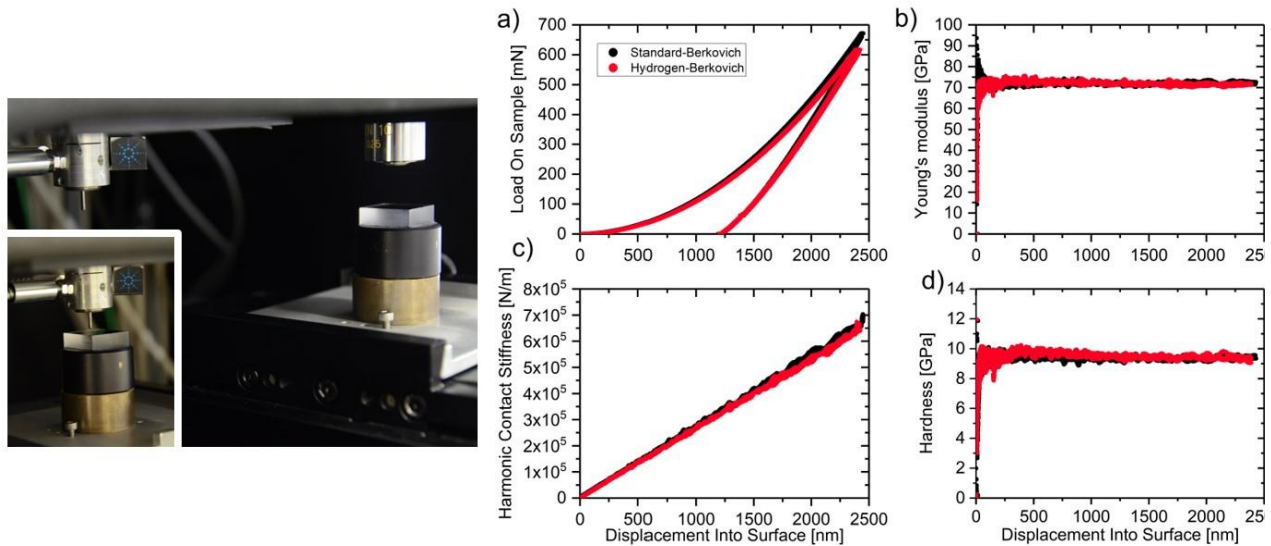


Fig. 3-4: Calibration setup and indentation data for standard and hydrogen Berkovich tip; a) load-displacement curve; b) Young's modulus over indentation depth; c) harmonic contact stiffness; d) hardness.

The agreement of both measurements show a well-defined calibration of the fluid tip and frame stiffness and thus ensure reliable measurements. Depending on the sample and how well it is mounted in the electrochemical cell further stiffness corrections have to be still applied for the individual tests.

3.5. Electrochemical charging

A further important part of the in-situ electrochemical nanoindentation is attributed to electrochemistry. Different preliminary tests have to be conducted before the charging setup and parameters can be determined. The next paragraphs will describe this process in further detail.

First of all, an appropriate electrolyte must be chosen. This can be achieved by a preceding literature study. After a promising type is found, the electrolyte sample combination can be checked by simple exposure test by storing the sample in a glass beaker overnight covered with electrolyte. Before and afterwards the sample surface should be controlled with the light microscope to confirm that no corrosion has occurred during contact. If this holds true, cyclic polarization curves can be recorded.

All following results exemplary represent the most often used electrolyte-material combination, which was used during this thesis. For the nickel-base alloy 725 a glycerine-based electrolyte with sulphuric acid H_2SO_4 with a mixing ratio of 2:1 as proposed by Stenerud [124] was used. Additionally, 1 g/l CH_4N_2S (Thiourea) was added as recombination poison, to promote the adsorption of hydrogen into the sample. Since nickel-base alloys have excellent corrosion resistance they are not sensitive to chloride environments and a Ag/AgCl electrode can be used for reference (as in Publication A). For more corrosion sensitive materials, a borax-based electrolyte in combination with a Hg/Hg₂SO₄ reference electrode can be used.

Fig. 3-5a shows the cyclic polarization curve for a nickel-base alloy 725 in precipitation hardened state. The open circuit potential (OCP), which is the initial potential of the system without applied voltage/current, depends on the assembly of material, electrolyte and reference electrode. Negative potentials, which correspond to the cathodic side, are used for charging the sample with hydrogen. Whereas, positive potentials on the anodic side of the polarization curve can withdraw the hydrogen from the sample.

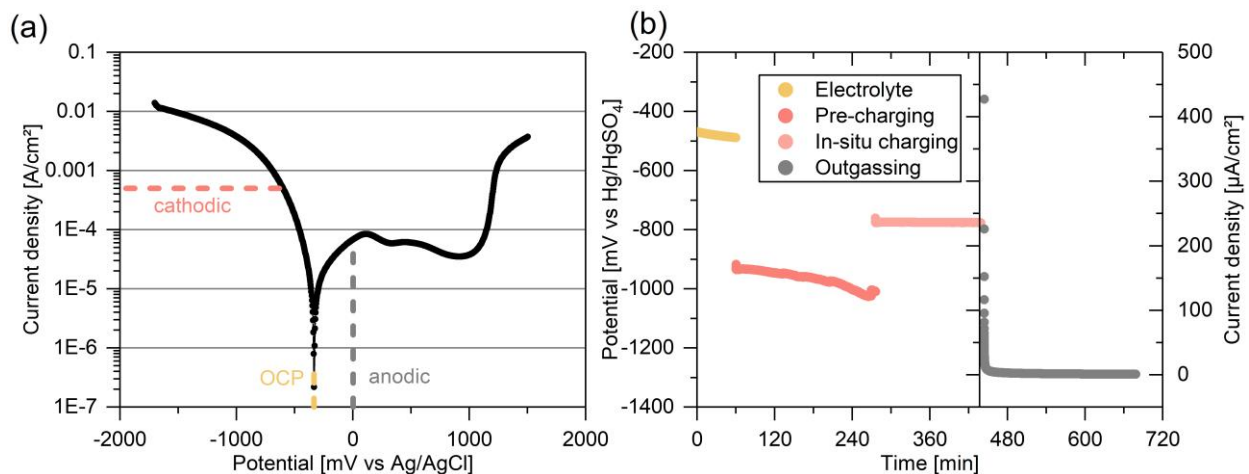


Fig. 3-5: Electrochemical data for nickel-base alloy 725 in precipitation hardened state; a) cyclic polarization curve; b) standard charging procedure.

An exemplary data set of our standard electrochemical charging procedure is visualized in Fig. 3-5b and comprises of four main parts. For guaranteeing an equilibrium of the system at the beginning of the experiment the OCP is measured for one hour. Afterwards the hydrogen charging starts, which is realized through galvanostatic charging with a constant current density to ensure a constant hydrogen flux. The charging itself is divided into two parts. The pre-charging step with

$-500 \mu\text{A}/\text{cm}^2$ and the in-situ charging, during nanoindentation, with $-10 \mu\text{A}/\text{cm}^2$. The current density must be lowered during indentation in order to avoid disturbances from the H_2 bubble formation, which occurs when charging with higher potential/currents. As a last step of this routine an anodic voltage of 0 mV is applied to the sample, which simulates the outgassing of the hydrogen and assures an intact sample surface near the passive region of the cyclic polarization curve.

If the recorded data shows a steady signal, as demonstrated in Fig. 3-5b, it can be expected that no corrosion or other surface modifications occurred during the charging. As an example for an unsuccessful charging cycle Fig. 3-6a shows an unsteady potentiostatic charging signal. The sample surface of the corresponding solution annealed sample is depicted in Fig. 3-6b. The entire sample is covered with slip steps and cracks emerge at some GBs and triple junctions. In our case this phenomenon only occurred for solution annealed material condition.

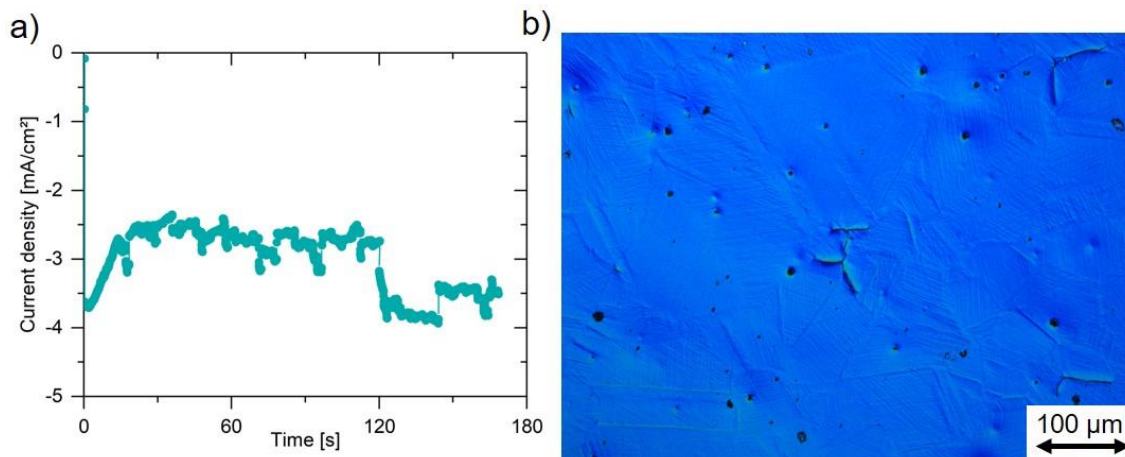


Fig. 3-6: Unsuccessful charging procedure for alloy 725 in solution annealed state; a) recorded current density for charging at a potential of -1000 mV vs. Ag/AgCl electrode; b) light microscope image from sample surface in circular polarized light differential interference (C-DIC) contrast

Detailed investigations of this hydrogen-induced slip steps have shown, that they occur immediately after high current density are applied. Fig. 3-7 shows already incipient slip steps after charging for 20 s with a current density of $-5 \text{ mA}/\text{cm}^2$. After 10 min of charging the slip steps are fully developed. The phenomenon of hydrogen-induced slip steps is also verified for super duplex steels and HEAs [137,128]. This surface modification can have tremendous influence on nanoindentation data, especially the analysis of pop-in is discussed in Publication A.

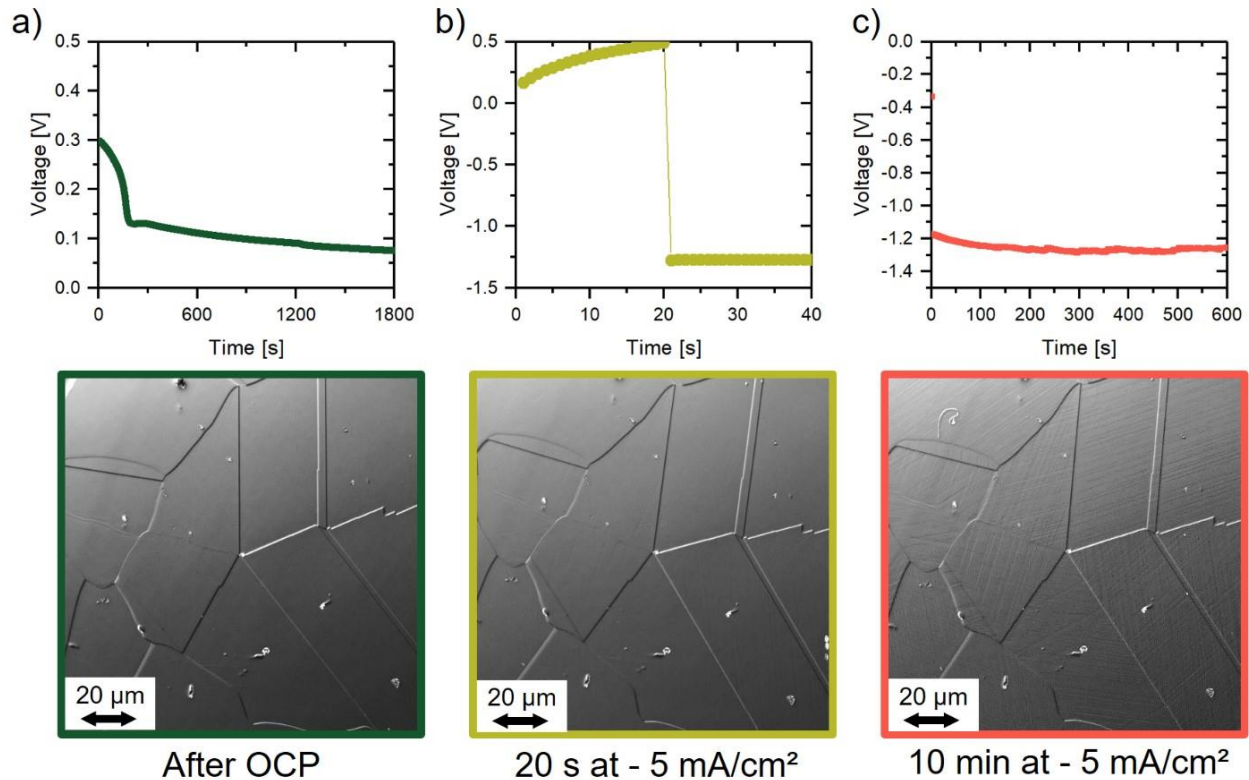


Fig. 3-7: Evolution of slip steps over time with electrochemical data and LSCM image; a) before charging before slip step evolution; b) after 20s of charging with incipient slip steps; c) after 10 min of charging with fully developed slip steps.

3.6. Testing procedure and challenges

The previous section explained the individual parts, which have to operate errorless for a successful in-situ electrochemical nanoindentation experiment. Fig. 3-8a lists some possible influences in the categories electrochemistry and nanoindentation. These two parts can now be combined in the overall testing procedure, which will be described in the next paragraphs and the work flow is schematically illustrated in Fig. 3-8b.

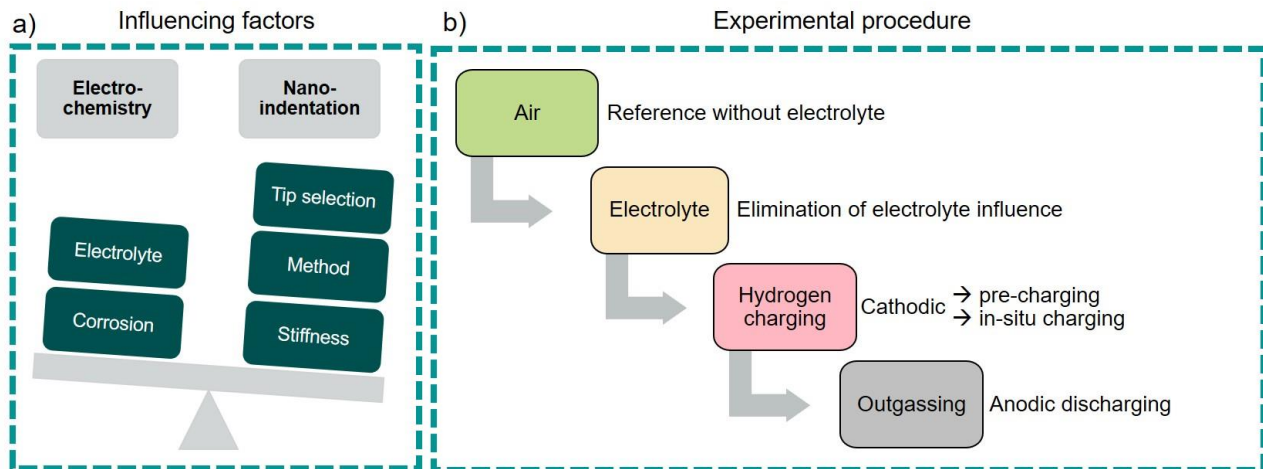
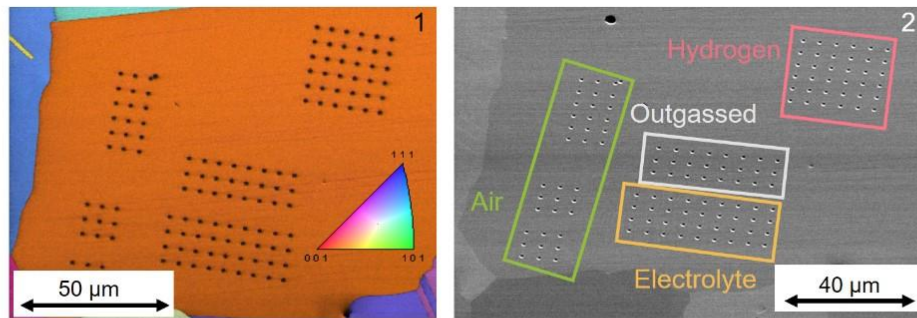


Fig. 3-8: a) Influencing factors and b) experimental procedure for electrochemical nanoindentation

The electrochemical charging procedure was already described in detail in section 3.5 and can be merged with different nanoindentation experiments. For each of the four conditions (Air, Electrolyte, Hydrogen, Outgassed) a set of indents is made. Several points need to be considered for good results. Depending on the parameters to be analysed, the settings for the nanoindentation experiment must be chosen carefully, e.g. tip geometry, number of indents and penetration depth. The differences in this settings for classical indentation with pop-in and hardness analysis (Publication A) in contrast to advanced nanoindentation strain rate jump tests (Publication B) are compared.

Fig. 3-9 show an IPF image as well as an optical images for both types of experiments. Both have in common that all indents are performed within one grain to exclude anisotropic material behaviour of the tested material. For getting a good statistical statement a larger set of indents is essential. In the case of the experiments with following pop-in analysis, the penetration depth only accounts 150-250 nm, since the pop-in for alloy 725 occurs in the first 20 nm. Therefore, a sufficient number of indentations for all conditions can be set inside on grain (Fig. 3-9a). For nanoindentation strain rate jump test a higher penetration depth of 1250 nm is necessary to implement the strain rate jump. As visible in Fig. 3-9 only eight indents fit into one grain for this material with a grain size of around 150 μm . Additionally, occurring twin boundaries can complicate this search. Therefore, a higher amount of grains and grain orientations must be tested during one experiment for good statistical analysis.

a) Pop-in analysis



b) Strain rate jump tests

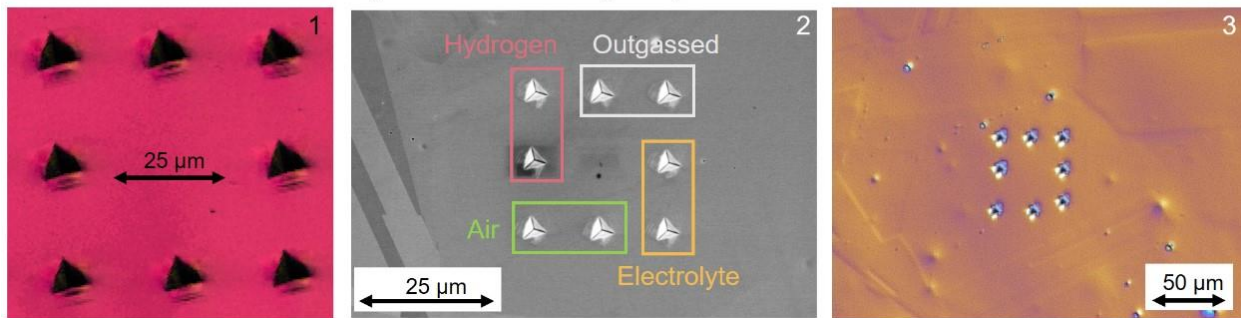


Fig. 3-9: Images of indented samples for a) classical in-situ electrochemical nanoindentation and b) electrochemical strain rate jump test; the indices indicate the type of picture: 1 – IPF image with overlaid image quality from EBSD; 2 – SE image from SEM; 3 – light microscopic picture with C-DIC contrast.

Also the tip selection depends on the type of analysis. For the analysis of the pop-in load a blunted Berkovich tip or as in our case a 2 μm conical tip is beneficial. Since as equation (23) reveals the pop-in load increases when increasing the tip radius. Further details on the correlation between pop-in load and indenter radius with regard to dislocation density can be found in reference [138]. In contrast strain rate jump tests require a sharp and well calibrated Berkovich tip, which was guaranteed through calibration procedure as described in 3.4.

A key feature of the setup and the testing procedure is the possibility of in-situ charging during nanoindentation. This is inevitable due to the fact of hydrogen outgassing from the sample after stopping the applied cathodic charging. If the sample is ex-situ charged outside the nanoindenter it needs to be immediately cooled with liquid nitrogen during the transfer into the nanoindenter chamber to prevent the outgassing of the hydrogen. Even during testing and

latency times for the thermal drift hydrogen continuously diffuses out of the sample. To visualize this effect Fig. 3-10a shows the hydrogen, which outgasses from an ex-situ charged sample after stopping the charging, measured with an hydrogen gas sensor (type MQ-8 for Arduino microcontroller). Additionally, a sensor of the same type is placed outside the glass beaker as a reference. The experimental setup is depicted in Fig. 3-10b. All of these uncertainties can be avoided by using an in situ charging setup, which supplies the sample continuously during testing.

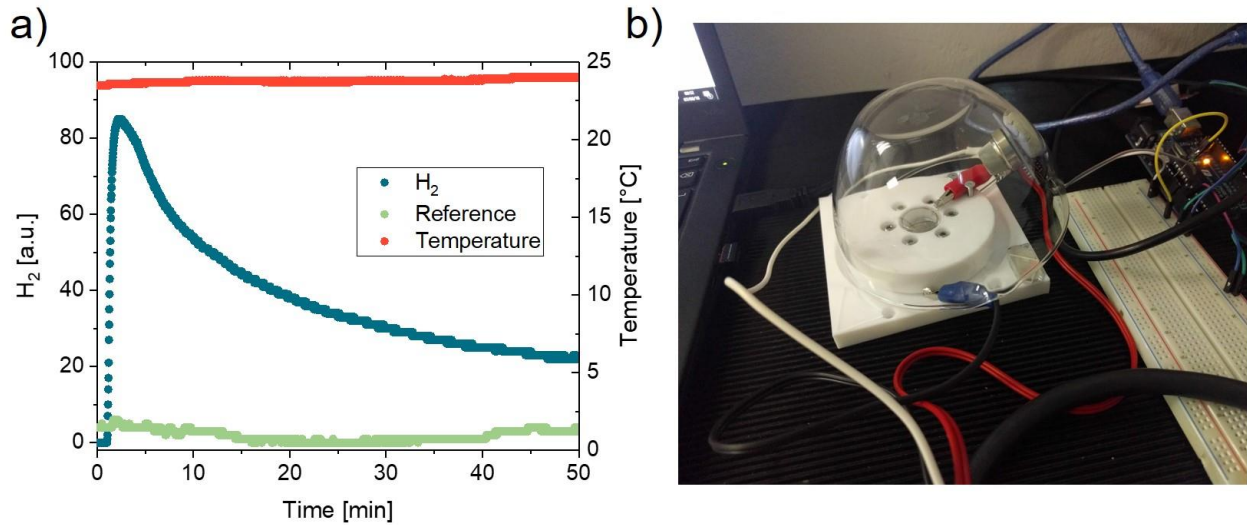


Fig. 3-10: Illustration of the outgassing behaviour of hydrogen; a) decreasing hydrogen gas concentration from the outgassing sample over time compared to reference sensor in air; b) experimental setup for measuring the outgassing profile.

4. Summary of the publications

The following sections will present the main findings and results, which emerged during this PhD thesis, by listing and summarizing the written publications. The work flow of this thesis is depicted in Fig. 4-1. It can be separated into two investigation paths, which had the aim to investigate and improve the performance of the nickel-base alloy 725 under hydrogen influence.

The first path dealt with the nanomechanical investigation of this alloy, and started with the implementation of the electrochemical setup for the G200 nanoindenter platform. The development process is briefly summarized in **Publication A** and the reliability is proved by first results on the standard mechanical properties of alloy 725 in hydrogen charged condition. A more detailed description of the implementation process is outlined in section 3 of this thesis.

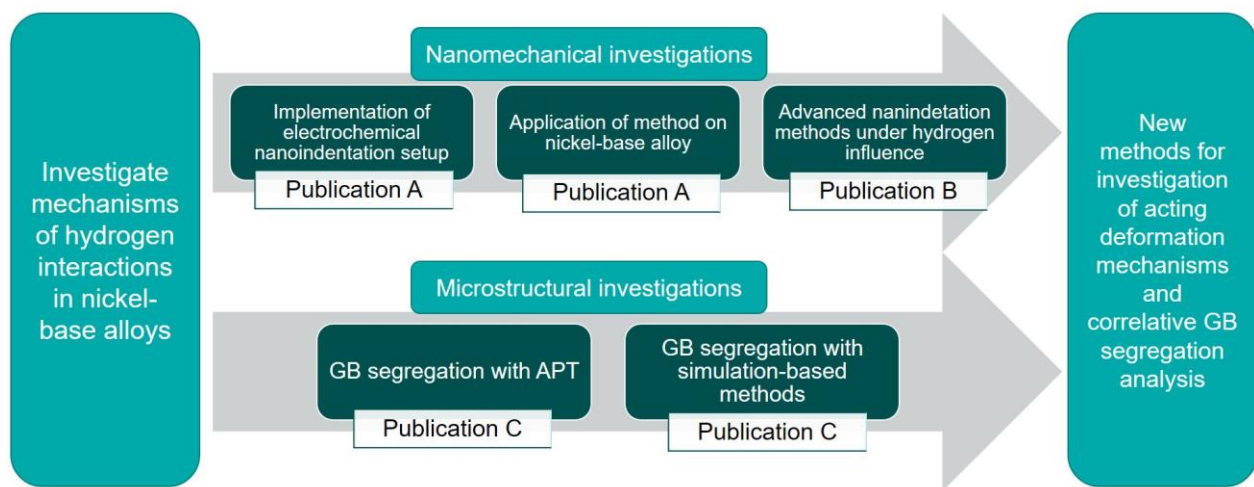


Fig. 4-1: Scheme of work packages and publications done within this thesis

Further work together with improvements on the setup enabled implementing advanced nanoindentation techniques. Therefore, **Publication B** deals with nanoindentation strain rate jump tests, which allow the investigation of deformation mechanisms and thermally activated parameters. The combination of this well-established method together with the electrochemical charging setup provide new possibilities for investigation of HE mechanisms on the microstructural scale.

The second investigation path focused on the analysis of GB segregation with two different approaches. After precise chemical analysis of the GB concentration with APT the

obtained data was used as input for cross-validation of simulation-based segregation predictions. In **Publication C** it is shown, how an accurate quantitative comparison between those two methods can be achieved.

Altogether, the performed developments and investigations complement the available evaluation methods for the investigation of HE and the dominating hydrogen-material interactions. These methods can help to shed some further light on the unsolved questions of HE in the future.

4.1. Publication list

Publication A

A Modified Electrochemical Nanoindentation Setup for Probing Hydrogen-Material Interaction Demonstrated on a Nickel-Based Alloy

A.S. Ebner, S. Brinckmann, E. Plesiutchnig, H. Clemens, R. Pippan, V. Maier-Kiener, JOM 72 (2020) 2020–2029.

DOI: <https://doi.org/10.1007/s11837-020-04104-9>

Publication B

Rate-depending plastic deformation behaviour in a nickel-base alloy under hydrogen influence

A.S. Ebner, E. Plesiutchnig, H. Clemens, R. Pippan, V. Maier-Kiener, International Journal of Hydrogen Energy, 46 (2021) 38132–38143.

DOI: <https://doi.org/10.1016/j.ijhydene.2021.09.030>

Publication C

Grain boundary segregation in Ni-base alloys: a combined atom probe tomography and first principles study

A.S. Ebner, S. Jakob, H. Clemens, R. Pippan, V. Maier-Kiener, S. He, W. Ecker, D. Scheiber, V.I. Razumovskiy, Acta Materialia 221 (2021) 117354

DOI: <https://doi.org/10.1016/j.actamat.2021.117354>

Remarks:

All co-authors have actively contributed to the appended publications by preparation of the manuscript and through fruitful discussions. For expert guidance, helpful discussions and impetus for all publications I want to acknowledge my supervisor V. Maier-Kiener. The main part of all experiments, data analysis and composition of the papers were performed by myself, Anna Sophie Ebner, with the following exceptions:

- Publication A** Steffen Brinkmann supported the construction of the experimental setup including the lifting table control unit and the electrochemical cell design.
- Publication B** V. Maier-Kiener assisted with the implementation of strain rate jump tests and shared her expertise in evaluation and interpretation of the results.
- Publication C** The ab-initio calculation part was conducted by D. Scheiber. Correlation of the experimental and simulation-based results was performed together with D. Scheiber and V.I. Razumovskiy.
- Part of the FIB and APT work was conducted together with S. Jakob, who also shared his expertise on the interpretation of IFE results.

Further publication

Influence of bias voltage on microstructure, mechanical properties and thermal stability of arc evaporated Cr_{0.74}Ta_{0.26}N coatings

C. Kainz, M. Pohler, G.C. Gruber, M. Tkadletz, A.S. Ebner, C. Czettl, N. Schalk
Surface and Coatings Technology 417 (2021) 127212.

DOI: <https://doi.org/10.1016/j.surfcoat.2021.127212>

4.2. Influence of hydrogen on standard nanomechanical properties of a nickel-base alloy (Publ. A)

Before reliable measurements can be conducted with a newly implemented system, a good calibration must be ensured. For nanoindentation, the two most important influencing variables are the setup stiffness as well as the area function calibration of the indenter tip. These calibrations and the further steps for the implementation are also described in detail in section 3 of this thesis.

After implementation and calibration, the setup was ready for conducting the first in-situ electrochemical nanoindentation experiments on alloy 725 in two different heat treated states, which were published in **Publication A**. The alloy was investigated in a solution annealed as well as precipitation hardened state. Solution annealing leads to a homogeneous distribution of all alloying elements and ensures a consistent fcc microstructure. In contrast, the precipitation hardened state has a more complex microstructure, which is also described in detail in section 2.2.1. This microstructure is the technically more relevant application state, and is therefore of great interest. The grain size of both tested materials was in the same range of approximately 150 μm , with many present twin boundaries. For indentation experiments, these twin boundaries restrict the possible available space, since all sets of indent should be placed inside one grain to avoid orientation influences (see Fig. 4-2a). Furthermore, the maximum penetration depth was set to 150 nm in order to place a sufficient amount of indents for each condition inside the chosen grain to get statistically well distributed results.

A standard charging procedure was applied, as explained in section 3.5 and shown in Fig. 3-5, and enabled the nanoindentation measurement of pop-in load, hardness and Young's modulus for both heat treatments. The first in-situ electrochemical nanoindentation studies primarily focused on the evaluation of the pop-in load [125,25,112,113] and therefore used materials with simple alloying concepts or even pure metals. In 2017 The a nickel-base alloy in solution annealed state was investigated for the first time through this technique by Stenerud et al. [124], who proposed an decrease in pop-in load. Their conclusion was not confirmed through the results of the solution annealed sample of alloy 725. For the charged and outgassed conditions a large scatter was found in the pop-in load data. This was related to hydrogen-induced surface

steps, which occurred during the charging procedure. These surface steps, have a great influence on the occurrence of pop-in, which is very sensitive to surface roughness and local stress concentrations at e.g. precipitates [122]. As a conclusion, no reliable pop-in analysis can be performed on solution annealed samples, when hydrogen-induced slip steps are present. Therefore, a reduced pop-in load is probably a result of the irreversible plastic deformation, which could be revealed through EBSD (Fig. 4-2b), rather than of the dissolved hydrogen.

As an additional result of the application of the CSM signal, which is described in chapter 2.4.2, Young's modulus and hardness can be evaluated through the whole penetration depth of the single experiments. The continuous and horizontal trend of the Young's modulus confirms the excellent setup stiffness and shows only minor changes for the four tested conditions (Air, Electrolyte, Hydrogen, Outgassing). In contrast, a hardness increase for the hydrogen charged condition was measured for both samples. The solution annealed sample shows an increase of 15 % compared to only 5.5 % for the precipitation hardened sample as summarized in Fig. 4-2c. This reduced sensitivity to the dissolved hydrogen can be related to presence of the strengthening precipitates, which can accumulate higher amounts of hydrogen at the matrix-precipitate interface and can further act as trapping sites. As a consequence, less hydrogen is left for acting as a Cottrell atmosphere, which hinders the dislocation motion and thus increases the hardness.

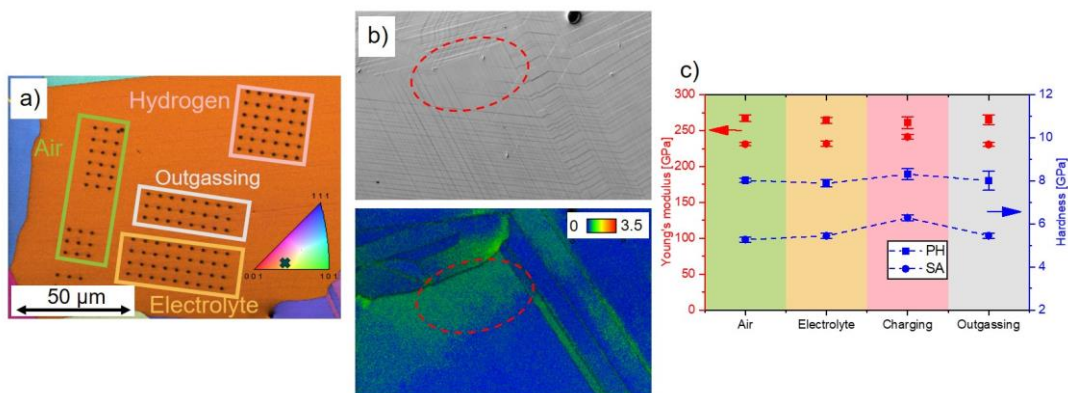


Fig. 4-2: Main results and findings of Publication A; a) intents after in-situ electrochemical nanoindentation on an IPF image; b) hydrogen-induced slip steps for solution annealed sample with irreversible plastic deformation visualized through average misorientation angle map from EBSD; c) average standard nanomechanical properties for solution annealed (SA) and precipitation hardened (PH) sample.

In summary, **Publication A** shows the proper functional principle of the modified electrochemical nanoindentation setup. Beside a brief information about the novelties and the calibration of the setup, it focuses on the standard mechanical properties of nickel-base alloy 725 and provides a critical discussion of the pop-in load. The pop-in load must be taken with caution, if surface irregularities are occurring through the electrochemical charging process. Further complex microstructural features as e.g. precipitates can extrinsically influence the pop-in, and must be considered in the discussion.

In any case, the implemented nanoindentation setup delivers feasible results and can be further used in combination with other advanced nanoindentation methods.

4.3. Influence of hydrogen on plastic deformation parameters of a nickel-base alloy (Publ. B)

To contribute to a better understanding of HE the underlying mechanisms must be also investigated on a local scale. Especially local plasticity plays an important role for the HELP mechanism. Therefore, the processes of plastic deformation and dislocation interaction can give promising insights. With the advanced nanoindentation method of strain rate jump tests the acting deformation mechanisms can be investigated by measuring the thermally activated deformation parameters of strain rate sensitivity and activation volume. The first attempt of applying this technique for investigation of HE mechanisms was performed by Hong et al. [139] on ex-situ charged austenitic stainless steel. Ex-situ charging always entails the uncertainties of outgassing and undefined hydrogen distributions, which must be avoided.

Therefore, **Publication B** proposes to take advantage of the in-situ electrochemical nanoindentation setup with CSM option to apply strain rate jump tests on the precipitation hardened nickel-base alloy 725 to identify the acting deformation mechanisms with and without hydrogen. This kind of investigation was absent in current literature. For this purpose, two indents with a depth of 1250 nm and one jump in strain rate from 0.05 to 0.001 s⁻¹ were performed for each condition inside four different grain orientations (see Fig. 4-3a). Similar to the results in **Publication A** a hydrogen-induced hardness increase of 7.4 and 7.9% was measured for the applied strain rates of 0.001 and 0.05 s⁻¹, and guarantee a successful charging procedure. The

strain rate sensitivity and the activation volume could be calculated from the occurring hardness jump. For the hydrogen charged condition an increase in strain rate sensitivity and a decrease in activation volume were determined (see Fig. 4-3b). In general, coarse grained fcc materials exhibit strain rate sensitivities close to zero. In this study a pronounced rate dependency ($m \approx 0.008$ - 0.001) was detectable due to the high alloying content and an increase in lattice friction due to the hydrogen charging for alloy 725. The low activation volume of approx. $30b^3$ indicate a Peierls-Nabarro mechanism, which is more common for bcc materials. Nevertheless, a further decrease after hydrogen charging is visible, which might be attributed to short-range effects through the solute hydrogen atoms.

Since this short-range effects can promote planar slip and consequently lead to localized deformation, the remaining imprints were investigated with different optical evaluation methods (see Fig. 4-3c).

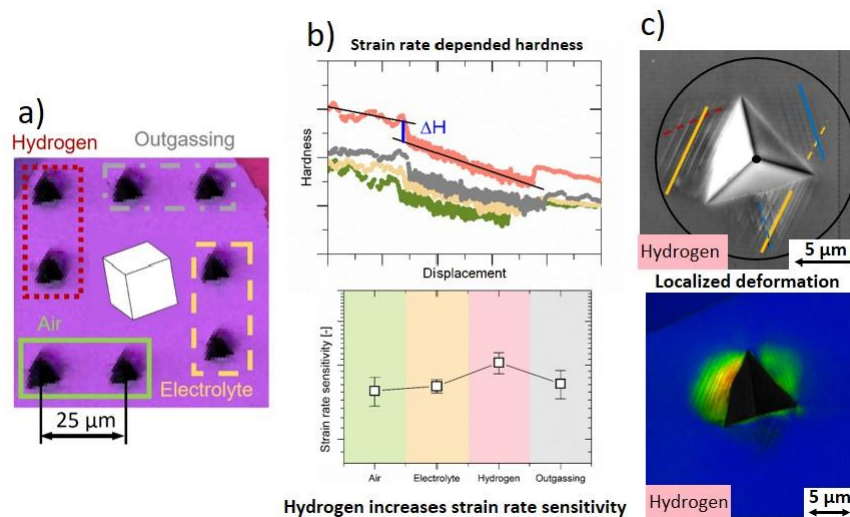


Fig. 4-3: Main findings and results from Publication B; a) remaining imprints for all measured conditions inside one measured grain; b) occurring hardness jump and increase in strain rate sensitivity; c) exemplary remaining imprints with identified slip systems, plastic zone and misorientation map.

SEM images of the imprints allowed a detailed determination of the slip step pattern, which evolve consistently inside one grain orientation. It was shown, that the hydrogen charging led to a reduction of the plastically deformed zone. Furthermore, less slip systems were activated and a narrower slip step spacing was observed. All these indicators suggest a restricted cross slip

capability, which can result in an enhanced planar slip and a more localized deformation. This localization can have further influence the resulting pile-up formation, which was additionally examined with LSCM. The hydrogen charging resulted in an increase in pile-up height as well as in an increased pile-up volume, which is in good agreement with other literature from Hong et al. [139] and Wang et al. [126]. Moreover, the misorientation angle was measured with EBSD and revealed a slightly higher misorientation for the hydrogen charged condition, which can give a hint on a somehow higher amount of geometrically necessary dislocations.

To sum up, **Publication B** has shown the successful application of the in-situ electrochemical nanoindentation setup in combination with strain rate jump tests, which offered the possibility to investigate rate-dependent deformation processes related to the role of hydrogen on the plastic deformation process. With the combination of optical investigation methods, such as SEM and LSCM, the consequences can be visualised. The changes in plastic deformation parameters and the plastically deformed zone can support the HELP hypothesis.

Overall, the **Publications A and B** have shown that electrochemical nanoindentation is a promising tool for investigating the influence of hydrogen on the plastic deformation process. Nevertheless, as HE is a complex process, also GB related methods can be a further approach to improve the susceptibility to HE. The combination of an experimental and a simulation-based method is therefore elucidated in the next section.

4.4. Grain boundary engineering with atom probe tomography and density functional theory (Publ. C)

GBE became a popular method for tailoring the materials properties over the last years also for improving the susceptibility to HE promising results are expected. For the segregation-based GBE, which takes advantage of the positive impact of segregating elements to the GBs, a profound knowledge of this processes is necessary. To the best of the author's knowledge, only a few studies are available, that are addressing the direct comparison of experimental and theoretical data on atomic segregation [140,141,70]. Therefore, **Publication C** aims for a quantitative comparison of the GB segregation in three modifications of nickel-base alloy 725 by

using the chosen methods of APT and DFT. Since they are working on different scales it requires an elaborate approach, which is based on the McLean segregation isotherm. The chemical complexity of the chosen alloy system, with several alloying elements, necessitates to consider site competitions and kinetic extensions of the segregation isotherm.

For the experimental investigations APT measurements were conducted on three different modification of the nickel-base alloy 725. For this purpose, APT tips of GBs with similar misorientation for all three samples were prepared via the side-specific preparation method with FIB according to the lift-out technique of Babinsky et al. [88]. Several tips (see Fig. 4-4a) for each modification could be successfully measured. Beside the bulk and the GB concentration further analysis provided the IFE value, which is a quantitative value for the segregation tendency in atoms/nm². For discussion of the IFE value, the complex microstructure of the precipitation hardened alloy was kept in mind. Therefore, the γ'' precipitates, which contain higher Nb and Ti concentrations, were identified and further analysed through proximity histograms and were mindfully considered in the discussion. Overall, the strongest segregation to the GB was found for B, Mo and C in all three alloy modifications.

For the simulation-based approach the segregation energies of the key alloying elements were calculated for a $\Sigma 5$ GB through ab-initio calculations of solutes (see Fig. 4-4c). For all elements interstitial and substitutional sites were considered. Negative segregation energies for stable interstitial sites, which indicate a segregation propensity, were only found for C, O, B, Si and P, whereas B and P dominate.

These segregation energies from DFT and the chemical bulk concentration from APT measurements were further used as input parameter for the modified multi-site and multi-component McLean isotherm. As an output the modelled GB concentration can be used for calculating the computed IFE value, which is then quantitatively compared with the experimentally determined values. The deviation of the calculated and measured IFE values lie mainly between ± 10 atoms/nm² (see Fig. 4-4b).

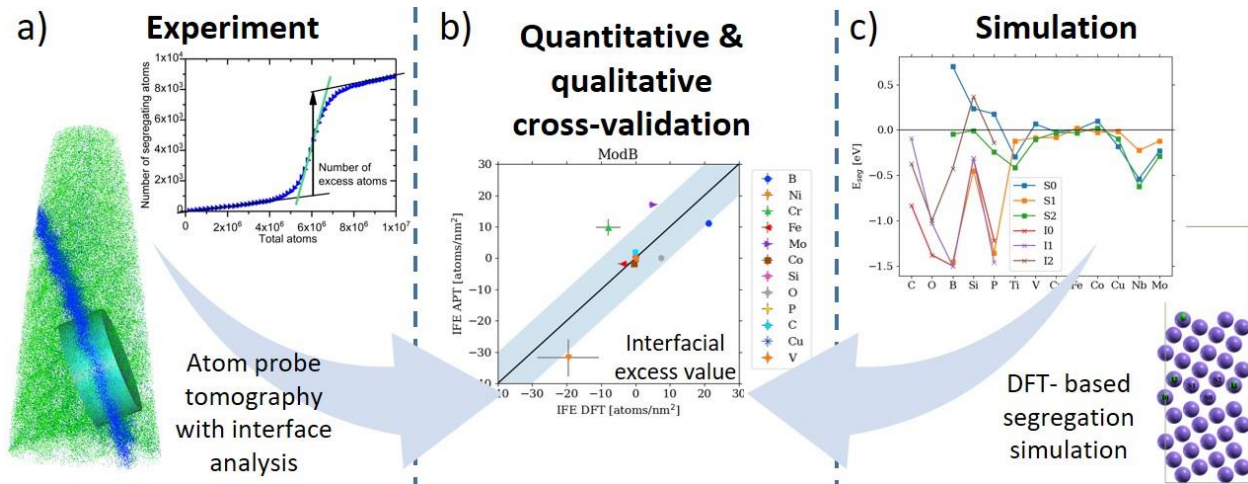


Fig. 4-4: Main findings and results from Publication C; a) APT tip with Ni (green) and B (blue) atoms and ROI for IFE analysis; ladder diagram for B atoms; b) comparison of computational and experimental IFE values; c) segregation energies from DFT and employed structure for $\Sigma 5$ GB.

Publication C provides a list of possible error sources, which can arise during comparison of the results. First of all, the approximations about temperature and concentration dependence influence the results, since it is assumed that the system is in thermodynamic equilibrium after the heat treatment. Furthermore, the experimentally investigated GBs are not $\Sigma 5$ GB as in the calculation, but the chosen GBs can be seen as representative for a high angle GBs. Finally, it has to be kept in mind, that the tested sample volume for APT is just a few nm³, and therefore provide a very localized view of the GB chemistry. A careful selection of the interfaces can guarantee to test similar GBs.

Taking into account all of these before mentioned approximations and precautions, an accurate comparison between DFT-based computational results and experimental APT data is possible. An extraordinary agreement can be reached if possible reasons for deviations are accounted. This approach in combination with the Rice-Wang theory of GB embrittlement is a promising tool to apply the segregation-based GBE to improve the resistivity of GBs against HE.

5. Conclusions and outlook

In order to investigate the hydrogen-materials interaction and underlying mechanisms, the main goal of this PhD thesis was to implement and improve an in-situ electrochemical nanoindentation setup. However, in order to exploit the full potential of this method, possible error sources and limitations must be considered for deriving reliable materials parameter. Due to its manifold usage and the reported failure cases due to HE, the nickel-base alloy 725 served as the model material for all present experimental investigations within this work.

The main results drawn from the implementation of the setup and the conducted material investigations can be summarized as follows:

- After a successful implementation of an electrochemical nanoindentation setup a thorough calibration is essential. The stiffness, as initial parameter for all further calculations, must be well-known and considered for conducting precise measurements. Furthermore, the area function of the used indenter tip has to be calibrated on a reference material with known properties, without unwanted stiffness influence from the lifting table.
- The electrochemical charging setup, consisting of the combination of sample material, electrolyte and electrodes must be carefully chosen ahead of the experiment. If a suitable combination is found the charging parameters (potential or current density) must be adapted to avoid disturbances of the nanoindentation tests through corrosion appearance or severe hydrogen gas bubble formation.
- In some special cases, electrochemical charging can lead to hydrogen charging-induced surface steps. It is suggested, that this surface steps arise from internal stresses and the pronounced hydrogen concentration gradient at the surface. This surface steps can have tremendous effects on the pop-in load, and therefore must be taken into account when evaluating the results. The pop-in load can be further affected by extrinsic influences, e.g. precipitations, and is therefore only restrictively suitable for precipitation hardened materials with complex microstructure.

- Through the hydrogen-induced hardness increase the sensitivity to hydrogen charging could be compared for a solution annealed and a precipitation hardened nickel-base alloy 725. Due to the precipitations acting as trapping sites for the hydrogen, the precipitation hardened sample showed a smaller influence on the hardness when compared to the solution annealed sample.
- The implemented setup was capable of conducting reliable nanoindentation strain rate jump tests. The influence of hydrogen on the strain rate sensitivity and the activation volume of a precipitation hardened nickel-base alloy 725 was demonstrated. Post-mortem analysis of the plastically deformed zone and pile-ups around the indents with optical methods support the HELP hypotheses.
- A segregation-based GBE concept was proposed. Based on DFT calculation of the segregation energy and the local bulk concentration measured with APT, the GB segregation in alloy 725 was predicted and verified according to the McLean segregation isotherm. It was shown, that through careful considerations a good comparison of simulation and experimental results is reached, and, consequently, can be used in future for further alloy development.

The present thesis outlines advanced in-situ electrochemical nanoindentation as a capable method for investigating the changes in nanomechanical properties under the influence of hydrogen. In upcoming studies this technique can be extended by implementing methods with e.g. spherical indenter tips for flow curve extraction or micromechanical tests as micro-pillar compression or micro-cantilever bending. Furthermore, the suggested GBE concept based on the analysis of GB segregation was found to provide good agreement between simulation and experiment. In the future, this method can be used deliberately to reduce the susceptibility of GBs to HE by taking advantage of the strengthening effects of GB segregation by employing beneficial alloying elements.

Therefore, the scientific investigations carried out in the framework of this study make a significant contribution to the hydrogen community, as the versatile application of the presented methodologies have been demonstrated.

6. References

- [1] The Sustainable Development Goals Report 2021, United Nations, 2021.
- [2] W.H. Johnson, On some remarkable changes produced in iron and steel by the action of hydrogen and acids, *Proc. R. Soc. Lond.* 23 (1875) 168–179.
- [3] S.P. Lynch, Failures of engineering components due to environmentally assisted cracking, *Practical Failure Analysis* 3 (2003) 33–42.
- [4] Nice, P. Strong, R., W.M. Bailey, G. Rorvik, J.H. Olsen, T.G. Mobberley, Hydrogen Embrittlement Failure of a PH Nickel Alloy Subsurface Safety Valve Component Installed in a North Sea Seawater Injection Well, *Corrosion Conference and Expo 2014* 3892 (2014) 1–16.
- [5] J. Cwiek, Prevention to Hydrogen Degradation of Steel, *Environmental Degradation of Engineering Materials & Materials Engineering and Technologies* 183 (2011) 31–36.
- [6] D.M. Symons, A comparison of internal hydrogen embrittlement and hydrogen environment embrittlement of X-750, *Engineering Fracture Mechanics* 68 (2001) 751–771.
- [7] D. Figueroa, M.J. Robinson, The effects of sacrificial coatings on hydrogen embrittlement and re-embrittlement of ultra high strength steels, *Corrosion Science* 50 (2008) 1066–1079.
- [8] S. Lynch, Discussion of some recent literature on hydrogen-embrittlement mechanisms: addressing common misunderstandings, *Corrosion Reviews* 37 (2019) 136.
- [9] S.P. Lynch, Hydrogen embrittlement phenomena and mechanisms, *Corrosion Reviews* 30 (2012) 105–123.
- [10] S.K. Sharma, S. Maheshwari, A review on welding of high strength oil and gas pipeline steels, *Journal of Natural Gas Science and Engineering* 38 (2017) 203–217.
- [11] Y. Zhao, J.-M. Park, D.-H. Lee, E.J. Song, J.-Y. Suh, U. Ramamurty, J. Jang, Influences of hydrogen charging method on the hydrogen distribution and nanomechanical properties of face-centered cubic high-entropy alloy: A comparative study, *Scripta Materialia* 168 (2019) 76–80.
- [12] A. Sieverts, Die Löslichkeit von Wasserstoff in Kupfer, Eisen und Nickel, undefined.
- [13] M.H. Armbruster, The Solubility of Hydrogen at Low Pressure in Iron, Nickel and Certain Steels at 400 to 600°, *J. Am. Chem. Soc.* 65 (1943) 1043–1054.
- [14] S. Pillot, L. Coudreuse, in: R.P. Gangloff, B.P. Somerday (Eds.), *The problem, its characterisation and effects on particular alloy classes*, Woodhead Publ, Oxford, 2012, pp. 51–93.
- [15] A. Lasia, in: W. Vielstich, A. Lamm, H.A. Gasteiger, H. Yokokawa (Eds.), *Handbook of Fuel Cells*, John Wiley & Sons, Ltd, Chichester, UK, 2010.
- [16] M. Truschner, A. Trautmann, G. Mori, The Basics of Hydrogen Uptake in Iron and Steel, *Berg Huettenmaenn Monatsh* 166 (2021) 443–449.

- [17] X. Lei, H. Wang, F. Mao, J. Zhang, M. Zhao, A. Fu, Y. Feng, D.D. Macdonald, Electrochemical behaviour of martensitic stainless steel after immersion in a H₂S-saturated solution, *Corrosion Science* (2018) 164–173.
- [18] G.P. Tiwari, A. Bose, J.K. Chakravartty, S.L. Wadekar, M.K. Totlani, R.N. Arya, R.K. Fotedar, A study of internal hydrogen embrittlement of steels, *Materials Science and Engineering A* 286 (2000) 269–281.
- [19] H. Kaesche, *Die Korrosion der Metalle: Physikalisch-chemische Prinzipien und aktuelle Probleme*, 3rd ed., Springer Berlin Heidelberg, Berlin, Heidelberg, 2011.
- [20] A. Drexler, C. Bergmann, G. Manke, V. Kokotin, K. Mraczek, S. Leitner, M. Pohl, W. Ecker, Local hydrogen accumulation after cold forming and heat treatment in punched advanced high strength steel sheets, *Journal of Alloys and Compounds* 856 (2021) 158226.
- [21] H. Mehrer, *Diffusion in solids: Fundamentals, methods, materials, diffusion-controlled processes ; with 27 tables*, Springer, Berlin, 2007.
- [22] A. Turnbull, in: B.P. Somerday, R.P. Gangloff (Eds.), *Gaseous hydrogen embrittlement of materials in energy technologies: Volume 1: The problem, its characterisation and effects on particular alloy classes*, Woodhead Publishing Ltd, Cambridge, 2012, pp. 89–128.
- [23] M. Nagumo, *Fundamentals of Hydrogen Embrittlement*, Springer Singapore, Singapore, 2016.
- [24] M.B. Djukic, G.M. Bakic, V. Sijacki Zeravcic, A. Sedmak, B. Rajicic, The synergistic action and interplay of hydrogen embrittlement mechanisms in steels and iron: Localized plasticity and decohesion, *Engineering Fracture Mechanics* 216 (2019) 106528.
- [25] A. Barnoush, H. Vehoff, Recent developments in the study of hydrogen embrittlement, *Acta Mater.* 58 (2010) 5274–5285.
- [26] L.B. Pfeil, The effect of occluded hydrogen on the tensile strength of iron, *Proc. R. Soc. Lond. A* 112 (1926) 182–195.
- [27] A. Troiano, The role of hydrogen and other interstitials in the mechanical behavior of metal, *Trans. Am. Soc. Met.* 52 (1960) 54–80.
- [28] R. A. Oriani, A mechanistic theory of hydrogen embrittlement of steels, *Berichte der Bunsengesellschaft für physikalische Chemie* 76 (1972) 848–857.
- [29] W.W. Gerberich, R.A. Oriani, M.-J. Lji, X. Chen, T. Foecke, The necessity of both plasticity and brittleness in the fracture thresholds of iron, *Philosophical Magazine A* 63 (1991) 363–376.
- [30] A. Drexler, S. He, R. Pippan, L. Romaner, V.I. Razumovskiy, W. Ecker, Hydrogen segregation near a crack tip in nickel, *Scripta Mater.* 194 (2021) 113697.
- [31] Y.A. Du, L. Ismer, J. Rogal, T. Hickel, J. Neugebauer, R. Drautz, First-principles study on the interaction of H interstitials with grain boundaries in α - and γ -Fe, *Phys. Rev. B* 84 (2011) 144121.
- [32] I.H. Katzarov, A.T. Paxton, Hydrogen embrittlement II. Analysis of hydrogen-enhanced decohesion across (111) planes in α -Fe, *Phys. Rev. Materials* 1 (2017) 33603.

- [33] S. He, W. Ecker, R. Pippan, V.I. Razumovskiy, Hydrogen-enhanced decohesion mechanism of the special $\Sigma 5(0\ 1\ 2)[1\ 0\ 0]$ grain boundary in Ni with Mo and C solutes, *Computational Materials Science* 167 (2019) 100–110.
- [34] C.D. Beachem, A new model for hydrogen-assisted cracking (hydrogen “embrittlement”), *Metall Mater Trans B* 3 (1972) 441–455.
- [35] I.M. Robertson, H.K. Birnbaum, An HVEM study of hydrogen effects on the deformation and fracture of nickel, *Acta Metall.* 34 (1986) 353–366.
- [36] T. Tabata, H.K. Birnbaum, Direct observations of hydrogen enhanced crack propagation in iron, *Scripta Metallurgica* 18 (1984) 231–236.
- [37] P.J. Ferreira, I.M. Robertson, H.K. Birnbaum, Hydrogen effects on the character of dislocations in high-purity aluminum, *Acta Materialia* 47 (1999) 2991–2998.
- [38] H.K. Birnbaum, P. Sofronis, Hydrogen-enhanced localized plasticity—a mechanism for hydrogen-related fracture, *Materials Science and Engineering A* 176 (1994) 191–202.
- [39] P. Sofronis, H.K. Birnbaum, Mechanics of the hydrogen-dislocation-impurity interactions—I. Increasing shear modulus, *Journal of the Mechanics and Physics of Solids* 43 (1995) 49–90.
- [40] J. Song, W.A. Curtin, A nanoscale mechanism of hydrogen embrittlement in metals, *Acta Materialia* 59 (2011) 1557–1569.
- [41] J. Song, W.A. Curtin, Mechanisms of hydrogen-enhanced localized plasticity, *Acta Mater.* 68 (2014) 61–69.
- [42] F. Zhang, W. A. Curtin, Atomistically informed solute drag in Al-Mg, *Modelling Simul. Mater. Sci. Eng.* 16 (2008) 55006.
- [43] Y. Jagodzinski, H. Hänninen, O. Tarasenko, S. Smuk, Interaction of hydrogen with dislocation pile-ups and hydrogen induced softening of pure iron, *Scripta Mater.* 43 (2000) 245–251.
- [44] Y. Deng, A. Barnoush, Hydrogen embrittlement revealed via novel in situ fracture experiments using notched micro-cantilever specimens, *Acta Materialia* 142 (2018) 236–247.
- [45] S.P. Lynch, Environmentally assisted cracking: Overview of evidence for an adsorption-induced localised-slip process, *Acta Metallurgica* 36 (1988) 2639–2661.
- [46] J.A. Clum, The role of hydrogen in dislocation generation in iron alloys, *Scripta Metallurgica* 9 (1975) 51–58.
- [47] S.P. Lynch, Metallographic contributions to understanding mechanisms of environmentally assisted cracking, *Metallography* 23 (1989) 147–171.
- [48] S.P. Lynch, Interpreting hydrogen-induced fracture surfaces in terms of deformation processes: A new approach, *Scripta Materialia* 65 (2011) 851–854.
- [49] *The Superalloys: Fundamentals and Applications*, TMS, 2006.
- [50] M. Iannuzzi, A. Barnoush, R. Johnsen, Materials and corrosion trends in offshore and subsea oil and gas production, *npj Mater Degrad* 1 (2017) 4.

- [51] M.S. Hazarabedian, M. Iannuzzi, The role of nano-sized intergranular phases on nickel alloy 725 brittle failure, *npj Mater Degrad* 5 (2021) 1–9.
- [52] R.J. Walter, R.P. Jewett, W.T. Chandler, On the mechanism of hydrogen-environment embrittlement of iron- and nickel-base alloys, *Materials Science and Engineering* 5 (1970) 99–110.
- [53] J.J. Jebaraj, D.J. Morrison, I.I. Suni, Hydrogen diffusion coefficients through Inconel 718 in different metallurgical conditions, *Corrosion Science* 80 (2014) 517–522.
- [54] A. Drexler, W. Siegl, W. Ecker, M. Tkadletz, G. Klösch, H. Schnideritsch, G. Mori, J. Svoboda, F.D. Fischer, Cycled hydrogen permeation through Armco iron – A joint experimental and modeling approach, *Corrosion Science* 176 (2020) 109017.
- [55] A.S. Ebner, S. Brinckmann, E. Plesiutchnig, H. Clemens, R. Pippan, V. Maier-Kiener, A Modified Electrochemical Nanoindentation Setup for Probing Hydrogen-Material Interaction Demonstrated on a Nickel-Based Alloy, *JOM* 72 (2020) 2020–2029.
- [56] X. Lu, Y. Ma, D. Wang, On the hydrogen embrittlement behavior of nickel-based alloys: Alloys 718 and 725, *Materials Science and Engineering A* 792 (2020) 139785.
- [57] X. Lu, D. Wang, D. Wan, Z.B. Zhang, N. Kheradmand, A. Barnoush, Effect of electrochemical charging on the hydrogen embrittlement susceptibility of alloy 718, *Acta Materialia* 179 (2019) 36–48.
- [58] L. Liu, K. Tanaka, A. Hirose, K.F. Kobayashi, Effects of precipitation phases on the hydrogen embrittlement sensitivity of Inconel 718, *Science and Technology of Advanced Materials* 3 (2002) 335–344.
- [59] L. Liu, C. Zhai, C. Lu, W. Ding, A. Hirose, K.F. Kobayashi, Study of the effect of δ phase on hydrogen embrittlement of Inconel 718 by notch tensile tests, *Corrosion Science* 47 (2005) 355–367.
- [60] V. Demetriou, J.D. Robson, M. Preuss, R. Morana, Study of the effect of hydrogen charging on the tensile properties and microstructure of four variant heat treatments of nickel alloy 718, *Int. J. Hydrogen Energy* (2017) 1–15.
- [61] Z. Tarzimoghdam, D. Ponge, J. Klöwer, D. Raabe, Hydrogen-assisted failure in Ni-based superalloy 718 studied under in situ hydrogen charging, *Acta Mater.* 128 (2017) 365–374.
- [62] M.S. Hazarabedian, M.Z. Quadir, M. Iannuzzi, Characterization of intergranular phases in precipitation hardening Ni alloy UNS N07725, *Materials characterization* 171 (2021) 110770.
- [63] M. Seita, J.P. Hanson, S. Gradečak, M.J. Demkowicz, The dual role of coherent twin boundaries in hydrogen embrittlement, *Nat Commun* 6 (2015) 6164.
- [64] J.P. Hanson, A. Bagri, J. Lind, P. Kenesei, R.M. Suter, S. Gradečak, M.J. Demkowicz, Crystallographic character of grain boundaries resistant to hydrogen-assisted fracture in Ni-base alloy 725, *Nature communications* 9 (2018) 3386.
- [65] Y. Yagodzinskyy, T. Saukkonen, S. Kilpeläinen, F. Tuomisto, H. Hänninen, Effect of hydrogen on plastic strain localization in single crystals of austenitic stainless steel, *Scripta Mater.* 62 (2010) 155–158.

- [66] D. Raabe, M. Herbig, S. Sandlöbes, Y. Li, D. Tytko, M. Kuzmina, D. Ponge, P.-P. Choi, Grain boundary segregation engineering in metallic alloys: A pathway to the design of interfaces, *Current Opinion in Solid State and Materials Science* 18 (2014) 253–261.
- [67] K. Leitner, D. Scheiber, S. Jakob, S. Primig, H. Clemens, E. Povoden-Karadeniz, L. Romaner, How grain boundary chemistry controls the fracture mode of molybdenum, *Materials & Design* 142 (2018) 36–43.
- [68] S. Bechtle, M. Kumar, B.P. Somerday, M.E. Launey, R.O. Ritchie, Grain-boundary engineering markedly reduces susceptibility to intergranular hydrogen embrittlement in metallic materials, *Acta Mater.* 57 (2009) 4148–4157.
- [69] P. Lejcek, *Grain Boundary Segregation in Metals*, Springer, Berlin, Heidelberg, 2010.
- [70] P. Lejček, M. Šob, V. Paidar, Interfacial segregation and grain boundary embrittlement: An overview and critical assessment of experimental data and calculated results, *Progress in Materials Science* 87 (2017) 83–139.
- [71] D. McLean, *Grain boundaries in metals.*, Clarendon Press, Oxford, 1957.
- [72] M.P. Seah, E.D. Hondros, Grain boundary segregation, *Proc. R. Soc. Lond. A* 335 (1973) 191–212.
- [73] R. Fowler, *Statistical thermodynamics*, Macmillan Co. The University Press, New York, Cambridge Eng, 1939.
- [74] M. Guttmann, Equilibrium segregation in a ternary solution: A model for temper embrittlement, *Surface Science* 53 (1975) 213–227.
- [75] M. Guttmann, D. McLean, in: W.C. Johnson, J.M. Blakely (Eds.), *Interfacial segregation*, Metals Park, Ohio, 1979.
- [76] D. Scheiber, L. Romaner, F.D. Fischer, J. Svoboda, Kinetics of grain boundary segregation in multicomponent systems – The example of a Mo-C-B-O system, *Scripta Mater.* 150 (2018) 110–114.
- [77] J.A. Kargol, M.V. Zeller, R. Asfahani, T.M. Parrill, AES studies of phosphorus impurity on hydrogen embrittlement of Ni₂Cr, *Applications of Surface Science* 15 (1983) 129–148.
- [78] E. Kny, W. Stolz, R. Stickler, H. Goretzki, Phase boundary segregation in the multiphase–multicomponent alloy IN 738 studied by AES and SEM, *Journal of Vacuum Science and Technology* 17 (1980) 1208–1212.
- [79] G. Da Rosa, P. Maugis, A. Portavoce, J. Drillet, N. Valle, E. Lentzen, K. Hoummada, Grain-boundary segregation of boron in high-strength steel studied by nano-SIMS and atom probe tomography, *Acta Mater.* 182 (2020) 226–234.
- [80] X. Huang, M.C. Chaturvedi, N.L. Richards, J. Jackman, The effect of grain boundary segregation of boron in cast alloy 718 on HAZ microfissuring—A SIMS analysis, *Acta Mater.* 45 (1997) 3095–3107.
- [81] B. Gault, M.P. Moody, J.M. Cairney, S.P. Ringer, *Atom probe microscopy*, Springer, New York, NY, 2012.

- [82] D.J. Larson, *Local Electrode Atom Probe Tomography: A User's Guide*, 1st ed., Springer New York, New York, NY, 2013.
- [83] W. Lefebvre, F. Vurpillot, X. Sauvage (Eds.), *Atom probe tomography: Put theory into practice*, Academic Press, London, 2016.
- [84] B. Gault, M.P. Moody, F. de Geuser, G. Tsafnat, A. La Fontaine, L.T. Stephenson, D. Haley, S.P. Ringer, Advances in the calibration of atom probe tomographic reconstruction, *Journal of Applied Physics* 105 (2009) 34913.
- [85] M.K. Miller, K.F. Russell, Atom probe specimen preparation with a dual beam SEM/FIB miller, *Ultramicroscopy* 107 (2007) 761–766.
- [86] P.J. Felfer, T. Alam, S.P. Ringer, J.M. Cairney, A reproducible method for damage-free site-specific preparation of atom probe tips from interfaces, *Microscopy research and technique* 75 (2012) 484–491.
- [87] K. Babinsky, R. de Kloe, H. Clemens, S. Primig, A novel approach for site-specific atom probe specimen preparation by focused ion beam and transmission electron backscatter diffraction, *Ultramicroscopy* 144 (2014) 9–18.
- [88] K. Babinsky, W. Knabl, A. Lorich, R. de Kloe, H. Clemens, S. Primig, Grain boundary study of technically pure molybdenum by combining APT and TKD, *Ultramicroscopy* 159 Pt 2 (2015) 445–451.
- [89] A.S. Ebner, S. Jakob, H. Clemens, R. Pippan, V. Maier-Kiener, S. He, W. Ecker, D. Scheiber, V.I. Razumovskiy, Grain boundary segregation in Ni-base alloys: a combined atom probe tomography and first principles study, *Acta Mater.* 221 (2021) 117354.
- [90] Bruce W. Krakauer and David N. Seidman, Absolute atomic-scale measurements of the Gibbsian interfacial excess of solute at internal interfaces, *Physical review B* 48 (1993) 6724.
- [91] M. Thuvander, H.-O. Andrén, A PFIM Studies of Grain and Phase Boundaries, *Materials characterization* 44 (2000) 87–100.
- [92] O.C. Hellman, D.N. Seidman, Measurement of the Gibbsian interfacial excess of solute at an interface of arbitrary geometry using three-dimensional atomprobe microscopy, *Materials Science and Engineering A* 327 (2002) 24–28.
- [93] J.R. Rice, J.-S. Wang, Embrittlement of interfaces by solute segregation, *Materials Science and Engineering A* 107 (1989) 23–40.
- [94] R. M. Smith, G. Sandland, An accurate method of determining the hardness of metals, with particular reference to those of a high degree of hardness, *Proceedings of the Institution of Mechanical Engineers* (1922) 623–641.
- [95] A. Wahlberg, Brinell's Method of Determining Hardness and Other Properties of Iron and Steel, *Journal of the Iron and Steel Institute* 1901 243–298.
- [96] S.P. Rockwell, The Testing of Metals for Hardness, *Transactions of the American Society for Steel Treating* 1922 (2) 1013–1033.
- [97] A. Martens, *Handbuch der Materialienkunde für den Maschinenbau*, Springer Berlin Heidelberg, Berlin, Heidelberg, s.l., 1912.

- [98] W.C. Oliver, G.M. Pharr, An improved technique for determining hardness and elastic modulus using load and displacement sensing indentation experiments, *J. Mater. Res.* 7 (1992) 1564–1583.
- [99] I.N. Sneddon, The relation between load and penetration in the axisymmetric boussinesq problem for a punch of arbitrary profile, *International Journal of Engineering Science* 3 (1965) 47–57.
- [100] J.B. Pethica, W.C. Oliver, Tip Surface Interactions in STM and AFM, *Phys. Scr.* T19A (1987) 61–66.
- [101] J.B. Pethica, W.C. Oliver, Mechanical Properties of Nanometre Volumes of Material: use of the Elastic Response of Small Area Indentations, *MRS Proceedings* (1989) 13–23.
- [102] J. Hay, P. Agee, E. Herbert, Continuous stiffness measurement during instrumented indentation testing, *Experimental Techniques* 34 (2010) 86–94.
- [103] W.C. Oliver, J.B. Pethica, Method for continuous determination of the elastic stiffness of contact between two bodies: US Patent(US4848141A).
- [104] B. Merle, V. Maier-Kiener, G.M. Pharr, Influence of modulus-to-hardness ratio and harmonic parameters on continuous stiffness measurement during nanoindentation, *Acta Mater.* 134 (2017) 167–176.
- [105] V. Maier, K. Durst, J. Mueller, B. Backes, H.W. Höppel, M. Göken, Nanoindentation strain-rate jump tests for determining the local strain-rate sensitivity in nanocrystalline Ni and ultrafine-grained Al, *Journal of Materials Research* 26 (2011) 1421–1430.
- [106] B.N. Lucas, W.C. Oliver, Indentation power-law creep of high-purity indium, *Metall Mater Trans A* 30 (1999) 601–610.
- [107] A.G. Atkins, D. Tabor, Plastic indentation in metals with cones, *Journal of the Mechanics and Physics of Solids* 13 (1965) 149–164.
- [108] C.D. Gu, J.S. Lian, Q. Jiang, W.T. Zheng, Experimental and modelling investigations on strain rate sensitivity of an electrodeposited 20 nm grain sized Ni, *New Journal of Physics* 40 (2007) 7440–7446.
- [109] K. Kumar, H. van Swygenhoven, S. Suresh, Mechanical behavior of nanocrystalline metals and alloys11The Golden Jubilee Issue—Selected topics in Materials Science and Engineering: Past, Present and Future, edited by S. Suresh, *Acta Materialia* 51 (2003) 5743–5774.
- [110] D. Kiener, R. Fritz, M. Alfreider, A. Leitner, R. Pippan, V. Maier-Kiener, Rate limiting deformation mechanisms of bcc metals in confined volumes, *Acta Mater.* 166 (2019) 687–701.
- [111] V. Maier, A. Hohenwarter, R. Pippan, D. Kiener, Thermally activated deformation processes in body-centered cubic Cr – How microstructure influences strain-rate sensitivity, *Scripta Mater.* 106 (2015) 42–45.
- [112] A. Barnoush, H. Vehoff, Electrochemical nanoindentation, *Scripta Mater.* 55 (2006) 195–198.

- [113] A. Barnoush, H. Vehoff, In situ electrochemical nanoindentation of Ni (111) single crystal, *J. Mater. Res.* 97 (2006) 1224–1229.
- [114] M. Zamanzade, Mechanical and electrochemical behavior of Fe₃Al-xCr intermetallics, Saarbrücken.
- [115] A. Barnoush, C. Bies, H. Vehoff, In situ electrochemical nanoindentation of FeAl (100) single crystal, *Journal of Materials Research* 24 (2009) 1105–1113.
- [116] A. Barnoush, M. Asgari, R. Johnsen, Resolving the hydrogen effect on dislocation nucleation and mobility by electrochemical nanoindentation, *Scripta Mater.* 66 (2012) 414–417.
- [117] A. Barnoush, H. Vehoff, Hydrogen embrittlement of aluminum in aqueous environments examined by in situ electrochemical nanoindentation, *Scripta Mater.* 58 (2008) 747–750.
- [118] E. Epler, Mechanical Properties of Lithiumion Batteryelectrodematerials at Different States of Charge. Ph.D. thesis, Göttingen, 2015.
- [119] M.J. Duarte, X. Fang, J. Rao, W. Krieger, S. Brinckmann, G. Dehm, In situ nanoindentation during electrochemical hydrogen charging: a comparison between front-side and a novel back-side charging approach, *Journal of Materials Science* (2021).
- [120] J. Kim, C.C. Tasan, Microstructural and micro-mechanical characterization during hydrogen charging: An in situ scanning electron microscopy study, *Int. J. Hydrogen Energy* 44 (2019) 6333–6343.
- [121] C. Müller, M. Zamanzade, C. Motz, The Impact of Hydrogen on Mechanical Properties; A New In Situ Nanoindentation Testing Method, *Micromachines* 10 (2019).
- [122] M. Göken, M. Kempf, Pop-Ins in Nanoindentations—The Initial Yield Point, *Zeitschrift für Metallkunde* 92 (2001) 1061–1067.
- [123] A. Barnoush, H. Vehoff, In situ electrochemical nanoindentation, *Corrosion Science* 50 (2008) 259–267.
- [124] G. Stenerud, R. Johnsen, J.S. Olsen, J. He, A. Barnoush, Effect of hydrogen on dislocation nucleation in alloy 718, *Int. J. Hydrogen Energy* 42 (2017) 15933–15942.
- [125] A. Barnoush, N. Kheradmand, T. Hajilou, Correlation between the hydrogen chemical potential and pop-in load during in situ electrochemical nanoindentation, *Scripta Mater.* 108 (2015) 76–79.
- [126] D. Wang, X. Lu, Y. Deng, X. Guo, A. Barnoush, Effect of hydrogen on nanomechanical properties in Fe 22Mn-0.6C TWIP steel revealed by in-situ electrochemical nanoindentation, *Acta Materialia* 106 (2019) 618–629.
- [127] N. Kheradmand, R. Johnsen, J.S. Olsen, A. Barnoush, Effect of hydrogen on the hardness of different phases in super duplex stainless steel, *Int. J. Hydrogen Energy* 41 (2016) 704–712.
- [128] D. Wang, X. Lu, Y. Deng, Di Wan, Z. Li, A. Barnoush, Effect of hydrogen-induced surface steps on the nanomechanical behavior of a CoCrFeMnNi high-entropy alloy revealed by in-situ electrochemical nanoindentation, *Intermetallics* 114 (2019) 106605.

- [129] Y. Zhao, D.-H. Lee, J.-A. Lee, W.-J. Kim, H.N. Han, U. Ramamurty, J.-Y. Suh, J. Jang, Hydrogen-induced nanohardness variations in a CoCrFeMnNi high-entropy alloy, *Int. J. Hydrogen Energy* 42 (2017) 12015–12021.
- [130] Y. Zhao, D.-H. Lee, M.-Y. Seok, J.-A. Lee, M.P. Phaniraj, J.-Y. Suh, H.-Y. Ha, J.-Y. Kim, U. Ramamurty, J. Jang, Resistance of CoCrFeMnNi high-entropy alloy to gaseous hydrogen embrittlement, *Scripta Materialia* 135 (2017) 54–58.
- [131] A. Barnoush, J. Dake, N. Kheradmand, H. Vehoff, Examination of hydrogen embrittlement in FeAl by means of in situ electrochemical micropillar compression and nanoindentation techniques, *Intermetallics* 18 (2010) 1385–1389.
- [132] N. Kheradmand, J. Dake, A. Barnoush, H. Vehoff, Novel methods for micromechanical examination of hydrogen and grain boundary effects on dislocations, *Philosophical Magazine* 92 (2012) 3216–3230.
- [133] X. Lu, D. Wang, Effect of hydrogen on deformation behavior of Alloy 725 revealed by in-situ bi-crystalline micropillar compression test, *Journal of Materials Science & Technology* 67 (2021) 243–253.
- [134] T. Hajilou, Y. Deng, B.R. Rogne, N. Kheradmand, A. Barnoush, In situ electrochemical microcantilever bending test, *Scripta Mater.* 132 (2017) 17–21.
- [135] T. Hajilou, Y. Deng, N. Kheradmand, A. Barnoush, Hydrogen enhanced cracking studies on Fe-3wt%Si single and bi-crystal microcantilevers, *Philosophical Transactions of the Royal Society A: Mathematical, Physical and Engineering Sciences* 375 (2017).
- [136] Y. Deng, T. Hajilou, D. Wan, N. Kheradmand, A. Barnoush, In-situ micro-cantilever bending test in environmental scanning electron microscope, *Scripta Mater.* 127 (2017) 19–23.
- [137] A. Barnoush, M. Zamanzade, H. Vehoff, Direct observation of hydrogen-enhanced plasticity in super duplex stainless steel by means of in situ electrochemical methods, *Scripta Materialia* 62 (2010) 242–245.
- [138] A. Barnoush, Correlation between dislocation density and nanomechanical response during nanoindentation, *Acta Mater.* 60 (2012) 1268–1277.
- [139] Y. Hong, C. Zhou, Y. Zheng, L. Zhang, J. Zheng, X. Chen, Dependence of strain rate on hydrogen-induced hardening of austenitic stainless steel investigated by nanoindentation, *Int. J. Hydrogen Energy* (2019).
- [140] D. Scheiber, V.I. Razumovskiy, P. Puschnig, R. Pippan, L. Romaner, Ab initio description of segregation and cohesion of grain boundaries in W–25 at.% Re alloys, *Acta Mater.* 88 (2015) 180–189.
- [141] T. Hajilou, I. Taji, F. Christien, S. He, D. Scheiber, W. Ecker, R. Pippan, V.I. Razumovskiy, A. Barnoush, Hydrogen-enhanced intergranular failure of sulfur-doped nickel grain boundary: In situ electrochemical micro-cantilever bending vs. DFT, *Materials Science and Engineering A* 794 (2020) 139967.

7. Publications

Publication A

A Modified Electrochemical Nanoindentation Setup for Probing Hydrogen-Material Interaction Demonstrated on a Nickel-Based Alloy

A.S. Ebner, S. Brinckmann, E. Plesiutchnig, H. Clemens, R. Pippan, V. Maier-Kiener, JOM 72 (2020) 2020–2029.

DOI: <https://doi.org/10.1007/s11837-020-04104-9>

Publication B

Rate-depending plastic deformation behaviour in a nickel-base alloy under hydrogen influence

A.S. Ebner, E. Plesiutchnig, H. Clemens, R. Pippan, V. Maier-Kiener, International Journal of Hydrogen Energy, 46 (2021) 38132–38143.

DOI: <https://doi.org/10.1016/j.ijhydene.2021.09.030>

Publication C

Grain boundary segregation in Ni-base alloys: a combined atom probe tomography and first principles study

A.S. Ebner, S. Jakob, H. Clemens, R. Pippan, V. Maier-Kiener, S. He, W. Ecker, D. Scheiber, V.I. Razumovskiy, Acta Materialia 221 (2021) 117354

DOI: <https://doi.org/10.1016/j.actamat.2021.117354>

Publication A

A Modified Electrochemical Nanoindentation Setup for Probing Hydrogen-Material Interaction Demonstrated on a Nickel-Based Alloy

**Anna Sophie Ebner, Steffen Brinckmann, Ernst Plesiutchnig,
Helmut Clemens, Reinhard Pippan, Verena Maier-Kiener**

JOM, 72 (2020) 2020-2029

A modified electrochemical nanoindentation setup for probing hydrogen-materials interaction demonstrated on a nickel-based alloy

Anna Sophie Ebner¹, Steffen Brinckmann^{2,3}, Ernst Plesiutchnig⁴, Helmut Clemens¹,
Reinhard Pippan⁵, Verena Maier-Kiener¹

¹ Department of Materials Science, Montanuniversität Leoben, Leoben, Austria

² Max-Planck-Institut für Eisenforschung GmbH, Düsseldorf, Germany

³ IEK-2, Research Center Jülich, Jülich, Germany

⁴ Böhler Edelstahl GmbH & Co KG, Kapfenberg, Austria

⁵ Erich Schmid Institute for Materials Science, Leoben, Austria

Keywords: In-situ electrochemical nanoindentation, nickel-based superalloy, hydrogen-induced surface steps, hydrogen embrittlement, electrochemical hydrogen charging

Abstract

An electrochemical charging setup was implemented in a nanoindentation system to evaluate the sensitivity of technically relevant materials to hydrogen embrittlement. Corresponding changes in the nanomechanical properties such as the hardness, Young's modulus and pop-in load can be measured and interpreted. A nickel-based alloy was examined in solution-annealed and aged condition. A hydrogen-induced hardness increase of 15% was measured for the solution-annealed sample. Aging the alloy leads to a reduced influence of hydrogen, lowering the hardness increase to 5%. For the solution-annealed sample, hydrogen charging-induced surface steps were observed and characterized with laser confocal microscopy and electron backscatter diffraction to reveal plastic deformation.

1. Introduction

Hydrogen embrittlement (HE) has been an ongoing interest and concern of the materials science community and industries over the past several decades. The oil and gas industries, which have to deal with harsh environments such as sour gas and seawater, suffer substantially from component failures due to HE [1,2]. Additionally, current developments in alternative energy sources and energy storage are promoting more intensive research into HE. Therefore, while industry is interested in developing more resistant materials and alloys for application, the science community has a particular focus on revealing the underlying deformation and failure mechanisms.

In the last years different atomistic models for HE have been proposed [3]. The most commonly known are the hydrogen-enhanced decohesion (HEDE) [4,5], hydrogen-enhanced localized plasticity (HELP) [6–9] and adsorption-induced dislocation-emission (AIDE) [3,10,11] models. In the HEDE model a weakening of the cohesive bonds between atoms was the mechanism used to explain the microscopically cleavage-like fracture surfaces in environments with high local hydrogen concentrations. It was first proposed by Oriani [4] and later also mentioned by Troiano [5]. The HELP mechanism proposes an enhanced localized plasticity and has been supported by TEM investigations [6]. Solute hydrogen shields the elastic stress field of dislocations, alters interactions and facilitates planar slip [7]. Due to the local higher relaxation, dislocations can cluster and therefore can lead to higher hardening. Enhanced local plasticity contrasts with the macroscopic brittle behaviour reported in body-centred cubic iron [8]. The simulation work of Song and Curtin [9] even suggests reduced dislocation mobility by hydrogen acting as Cottrell atmospheres. A mechanism that somehow combines elements of both, HEDE and HELP, is the AIDE mechanism proposed by Lynch [3,10,11]. He explains the adsorbed hydrogen responsible for the hydrogen-assisted cracking. His model describes the adsorption of hydrogen at the crack tip, which reduces the dislocation formation energy resulting in an easier dislocation emission. Characteristic for the AIDE mechanism is the occurrence of micro-voids on cleavage-like or intergranular fracture surfaces ahead of the crack tip.

It seems that none of the above-mentioned mechanisms is able to provide a complete picture of HE at a macroscopic as well as microscopic scale. Despite some contradictions, overlaps

are possible [11,12]. Therefore, it is important to find new promising techniques, both experimentally and simulated, to investigate and understand the acting mechanisms in further detail. A promising experimental approach, which was first proposed by Barnoush and Vehoff [13] in 2006, is electrochemical nanoindentation (ECNI). Since nanoindentation is a very localized testing method with a high depth resolution, material response can be tested directly in small volumes, where the hydrogen mechanisms take place. First experiments were dedicated to the analysis of pop-in loads [14–17]. This sudden displacement burst in the recorded load–displacement curve can be correlated to a homogeneous dislocation nucleation (HDN). However, this only applies for coarse-grained materials with a low intrinsic dislocation density. The volume below the indenter tip must be quasi-dislocation free to nucleate the first dislocation at the transition from elastic to elastic-plastic deformation behaviour [18]. Barnoush et al. [17] proposed a decrease of pop-in load with hydrogen by decreasing the necessary activation energy for HDN according to the classical dislocation theory. They suggested a combined HEDE and HELP mechanism by weakening of the interatomic bonds, which they either explain by a reduction of the shear modulus or the stacking fault energy.

Later investigations also focused on the hardness evolution during the ECNI [19–23]. The measured hardness increase supports their hypotheses of a decreasing dislocation mobility due to hydrogen. Further explanations are an increase in lattice friction [20,21] as well as a classical solid solution strengthening contribution by hydrogen [16,22,23]. Overall, a variety of ECNI experiments have been performed, first on fundamental materials such as iron or technically clean nickel [15,24], while more recent investigations have tried to meet the demands of industry by testing technically relevant engineering alloys [19,20,25].

For reliable ECNI experiments the hydrogen diffusion behaviour has to be taken into account. After charging the sample ex situ with hydrogen in an electrolyte by applying a cathodic potential to the specimen, the problem of prompt outgassing during sample transfer from the charging environment to the nanoindenter has to be considered. Samples must be cooled with liquid nitrogen to prevent outgassing, and testing must be performed as soon as possible. All of these uncertainties can be avoided by using an in situ charging setup.

Most of the previous ECNI studies were performed using simple load-controlled indentation. Therefore, only mechanical properties of the specific selected indentation depth can be obtained. The G200 nanoindenter, which is used in this work, has an advanced dynamic testing method called continuous stiffness measurement (CSM) [26,27], where a sinusoidal load signal is superimposed during loading. This method allows a continuous measurement of Young's modulus and hardness over the whole indentation depth and can give further information on possible external influences, such as frame stiffness or depth-dependent properties. The newly developed in situ ECNI setup in combination with the CSM technique is used to investigate the nanomechanical response of a technically relevant nickel-based alloy under the influence of hydrogen.

2. Experimental

2.1. Material, preparation and microstructural investigations

A trial melt of nickel-based alloy 725 was melted using a vacuum induction furnace and forged to a 130 mm bar. After forging and before the investigation, the alloy was heat treated in two conditions. For the solution-annealed (SA) condition, the material was held at 1040°C for 2 h and subsequently water quenched. For the second condition, aging was done at 740°C and 620°C for 8 h each after solution annealing. This aging cycle is in accordance with a standard of the American Petroleum Institute (API); therefore, it will be referred to the abbreviation API for the aged sample. Cylindrical samples with 12 mm diameter were produced via wire erosion. Before testing, all samples were cold embedded with Struers Durocit and cut into dimensions of 18 mm³ x 18 mm³ x 3 mm³ to fit into the electrochemical cell. The embedded samples were ground by using 320 and 800 grid SiC paper followed by polishing with 9 μm, 3 μm and 1 μm diamond paste, respectively. Struers OP-S solution was used as a last mechanic-chemical polishing step. To remove the remaining deformation layer, electropolishing with a methanolic H₂SO₄ solution was carried out in the Struers Lectropol applying 22 V for 40 s [19]. The microstructure was analysed using a laser confocal microscope LEXT OLS4100 (Olympus, Tokyo, Japan) for topography images, which were post-processed with Gwyddion software. Scanning electron microscope (SEM) images and electron backscatter diffraction (EBSD) were carried out on a FEI 3D DualBeam workstation (Thermo Fisher Scientific, Waltham, MA, USA) with an EDAX Hikari XP EBSD camera (EDAX Inc.,

Mahwah, NJ, USA). In addition to grain orientation, also misorientation maps were created with TLS OIM Analysis 7 software (EDAX Inc.).

2.2. Material, preparation and microstructural investigations

An in situ electrochemical nanoindentation setup was implemented in a nanoindentation G200 platform (KLA, Milpitas, CA, USA). This indentation system is known for an overall high frame stiffness as well as for a well-developed dynamic measurement technique known as CSM. The high frame stiffness originates from a rigid frame with a movable table, which is fixed in z-height and leads to a consistent stability to measured mechanical properties. The electrochemical charging cell was designed to benefit from those unique features. A lifting table, consisting of a mini lab jack (Thorlabs Inc., Newton, NJ, USA) and a self-built control unit, was installed to mount the cell and allow precise indentation experiments in a liquid environment [28]. Therefore, an additional fluid tip with an elongated stainless steel shaft was utilized to overcome the resultant difference in height. The electrochemical cell itself was designed in a sandwich-like manner as shown in Fig. 1a with an aluminium base plate to provide further stiffness and a top cover made out of Teflon (PTFE), which accommodates the electrolyte compartment as well as all necessary electrodes and also provides good chemical resistance.

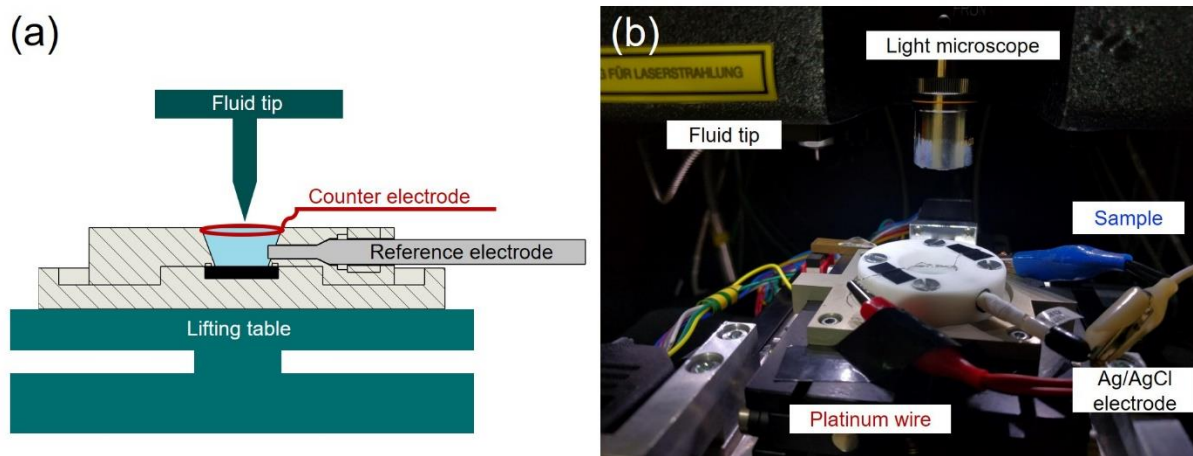


Fig. 1 Electrochemical nanoindentation setup for the G200 platform: (a) schematic drawing and (b) appropriate front view.

2.3. Electrochemical measurements

All electrochemical measurements were conducted with a Gamry 1010B potentiostat in a glycerine-based electrolyte with phosphoric acid in a mixing ratio of 2:1 [19]. To promote the absorption of hydrogen, 1 g/L CH₄N₂S (Thiourea) was added as recombination poison. All reported potentials were measured against an Ag/AgCl reference electrode from ALS Japan with a platinum wire as counter electrode. Beforehand, an example polarization curve was recorded for the material in SA condition to allow for an appropriate choice of charging conditions. The polarization curve was recorded from -1700 mV up to 1500 mV with a scanning rate of 3 mV/s.

2.4. Nanoindentation parameters

All nanoindentation experiments were performed on a KLA G200 nanoindenter utilizing the mentioned electrochemical cell described above and a CSM technique superimposing a harmonic displacement of 2 nm with a frequency of 45 Hz to continuously measure the contact stiffness and thus hardness and Young's modulus over indentation depth. A conical diamond tip with a specified radius of 2 μm and an elongated steel shaft with an additional protective epoxy coating (Synthon-MDP, Nidau, Switzerland) was used. Since the lifting table lowers the overall stiffness of the system, it is not suitable for a reliable tip calibration. To overcome this issue, tip shape calibrations were conducted with a standard fused silica calibration sample within a rigid brass holder. This allows performing reliable Young's modulus and hardness measurements with a minimum of stiffness correction up to 1000 nm indentation depth.

All nanoindentation experiments were evaluated according to the Oliver and Pharr method [29] using a Poisson ratio of 0.31 for nickel to convert the reduced modulus from the indentation experiment to a comparable Young's modulus. Indentations were performed in a constant strain-rate mode (0.005 s⁻¹) up to a maximum indentation depth of 150 nm. All hardness and Young's moduli were averaged between 100 nm and 130 nm. For reliable nanomechanical data the lack of self-similarity of spherical tips has to be taken into account when performing a strain rate controlled experiment [30]. Therefore, a simplified strain rate definition published by Feldner et al. [31] was used for controlling the loading segment. The unloading rate was set to 50 nm/s.

2.5. In-situ ECNI

All ECNI experiments consist of four main parts. To describe the initial, pre-charging state of the materials, indentations were performed in air. For detecting any possible influences due to the electrolyte, the next set of indentations was made during the measurement of the open circuit potential (OCP) to represent an uncharged state in electrolyte contact. The charging part itself is divided into pre-charging and in situ charging. Pre-charging was conducted for 2.5 h at a relatively high cathodic current density of $-500 \mu\text{A}/\text{cm}^2$ on a total exposed area of 1.33 cm^2 . During the actual in situ nanoindentation tests the current density was lowered to $-10 \mu\text{A}/\text{cm}^2$ to reduce hydrogen bubble formation for fewer disturbances during indentation. The last part consists of an outgassing step, which was obtained by outgassing in air for 18 h for the SA sample. The hydrogen of the API specimen was withdrawn by applying an anodic potential of 0 mV for 3 h. A minimum of 12 indentations for each condition was performed to obtain reliable mean values with standard deviation error bars.

3. Results

3.1. Microstructure

Grain boundaries react preferentially during electropolishing, and thus the microstructure is visible in the light-optical microscope as well as in the SEM. Fig. 2 sums up the initial microstructure, exemplarily shown for the SA sample in Fig. 2a, and correspondingly the orientations of the indented grains on both samples are shown in (b). Average grain size was $140 \mu\text{m}$ with no texture present. The orientations of the grains are marked with dots in the inverse pole figure (IPF) triangle in Fig. 2b. For the SA sample the orientation chosen for indentation had a (0 6 1) orientation, corresponding to a near (0 0 1) orientation. In comparison, the grain on the API sample was more in the (1 1 1) direction with Miller indices of (18 11 13). The unit cells are shown as inserts in Fig. 2b.

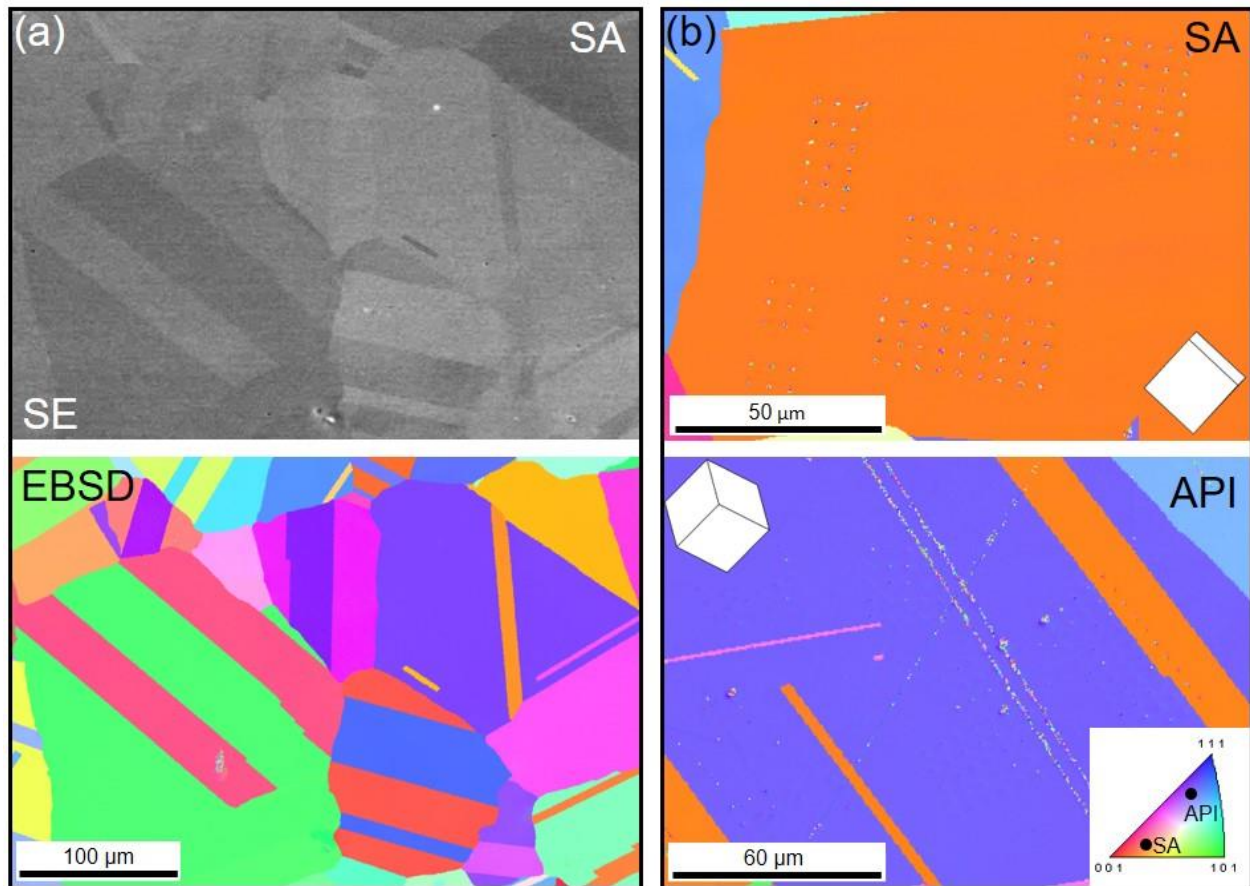


Fig. 2 (a) Microstructure and grain size of an SA condition: SE image (top) and EBSD (bottom); (b) IPF map of indented grain for the SA (top) and API sample (bottom).

3.2. Electrochemical measurements

Figure 3a represents the polarization curve obtained. Starting in the cathodic regime, where hydrogen is produced on the sample surface, the current density decreases from a potential of -1700 mV until the OCP is reached at a potential of -310 mV. The anodic part reaches from the OCP till 1500 mV and includes an anodic nose followed from a passive region before the breakdown potential is reached at around 1000 mV. By taking the polarization curve characteristics into account, a cathodic charging current of $-500 \mu\text{A}/\text{cm}^2$ was chosen to ensure hydrogen absorption. For anodic discharging and promoting hydrogen outgassing, a potential in the beginning of the passive region of 0 mV was selected. All chosen states are marked with dashed lines in Fig. 3a. Figure 3b shows the electrochemical data received for the chosen potentials, which were applied according the procedure described in Sect. 2.5.

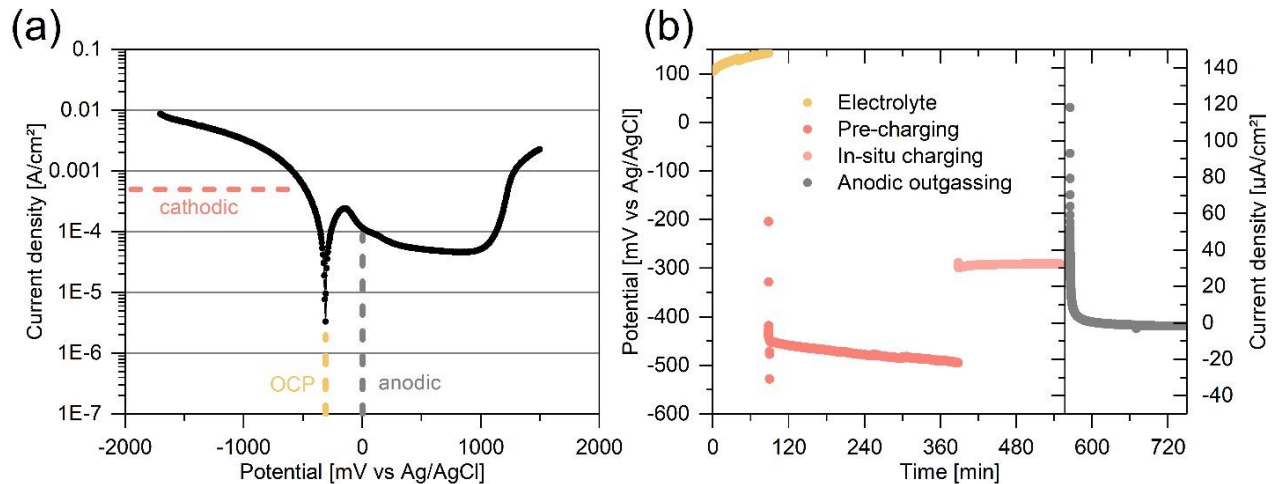


Fig. 3 (a) Representative polarization curve with applied current density and potentials for the SA sample; (b) resulting data from the potentiostat for charging and discharging of the API sample.

3.3. Surface steps after hydrogen charging

Before and after in situ ECNI the sample surfaces were examined with a laser confocal microscope to exclude surface irregularities as well as corrosion effects. A reference position of the SA sample is depicted in Fig. 4. Before testing the root-mean-square roughness, R_q , averaged for three horizontal 15 μm line profiles for each grain in the examined section was 0.71 ± 0.05 nm. After charging, surface steps are present on the entire sample surface, which leads to an increase of R_q to 1.12 ± 0.3 nm in the selected region.

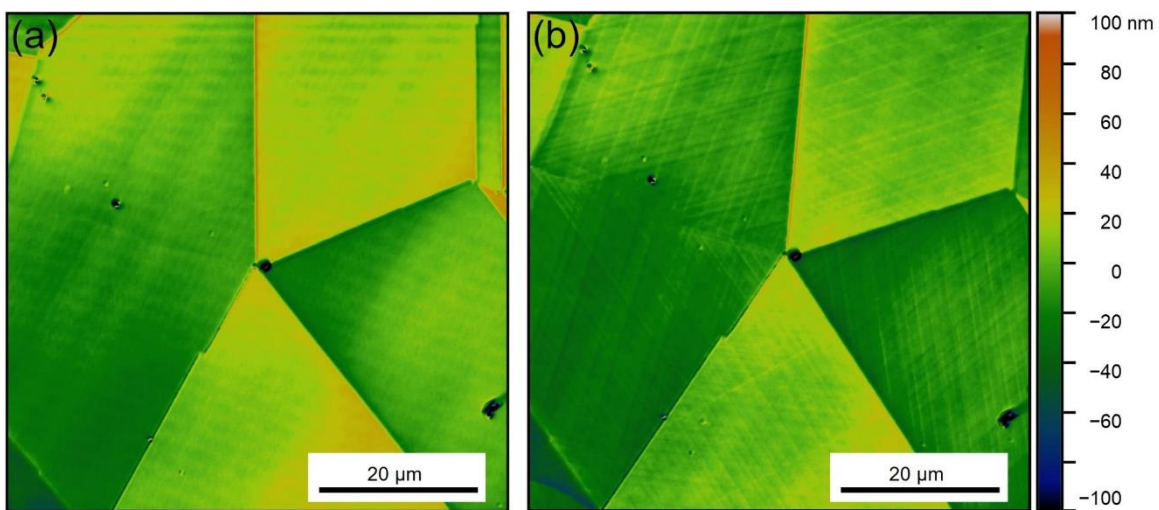


Fig. 4 Representative laser confocal microscope height images of the SA sample (a) before and (b) after the hydrogen charging experiment.

When characterizing the slip steps with different techniques, e.g., compare Fig. 4a and b, it is obvious that the intensity and occurrence of slip steps vary between different grains depending on their orientation. The activated slip system corresponds to those with the maximum Schmid factor (see insert in Fig. 5a) [32]. Additionally, in the vicinity of some grain boundaries it can be observed that the slip lines disappear as soon as they approach the grain boundary. For example, such an area is marked in Fig. 5a with a red dashed circle. The green area in the orientation deviation map in Fig. 5c indicates an increasing misorientation of the fading slip lines. Moreover, the yellow dotted misorientation line profile verifies an increase of point-to-origin misorientation of around 0.4° .

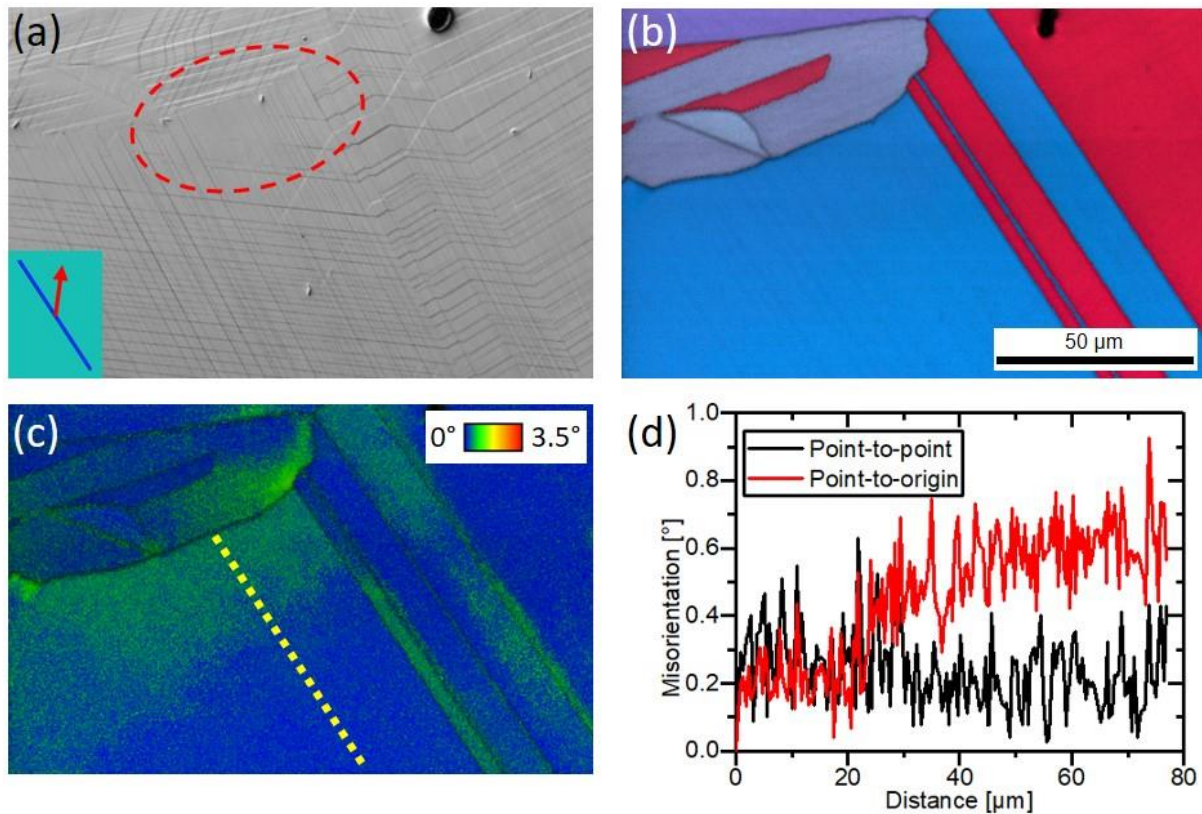


Fig. 5 Characterization of slip line formation on an SA sample with different techniques: (a) laser confocal microscope intensity image with marked areas of interest; (b) IPF image with overlaid image quality (IQ); (c) orientation deviation map with overlaid IQ and yellow dotted line for the misorientation profile shown in (d).

3.2. Nanomechanical properties during ECNI

In addition to standard mechanical properties such as Young's modulus and hardness, also the so-called pop-in load can be measured for the SA sample. This sudden displacement burst marks the transition from fully elastic to elastic–plastic deformation behaviour and is an indicator for a HDN in coarse-grained materials with low dislocation density [17,33].

Figure 6 sums up the in situ ECNI results for the SA sample, (a) including exemplary load–displacement curves Young's modulus and hardness (b). Large data points represent the average value for each condition, and small grey points symbolize a single indentation experiment. The pop-in load stays constant for indentations in air as well as with electrolyte at around $1.05 \text{ mN} \pm 0.05 \text{ mN}$. After charging, the mean value is slightly lower around 0.99 mN , but the standard deviation increases dramatically to 0.23 mN . This can be described by the results of single indentations, which include a few lower values but also pop-in loads near the mean value for air and even above. During outgassing, no recovery of the pop-in load is visible; only a slight decrease in the standard deviation takes place. As verification for the initial pop-in, the Hertzian fit for a tip radius of $1.5 \text{ }\mu\text{m}$ is included in the load–displacement curve in Fig. 6b. More significant changes can be noticed in the hardness data. The first minor increase in hardness is visible from the air to electrolyte from $5.26 \pm 0.11 \text{ GPa}$ to $5.44 \pm 0.12 \text{ GPa}$, which still lies within the uncertainty of the measurements and the corresponding error bars. Hydrogen charging leads to an obvious increase to $6.28 \text{ GPa} \pm 0.13 \text{ GPa}$, which corresponds to an increase of 15% compared with the hardness in the electrolyte. CSM data in Fig. 6b confirm the hardness increase over the entire indentation depth. The observed continuous decrease in hardness with increasing indentation depth for all conditions originates from the so-called indentation size effect, which is usually explained by the Nix–Gao model [34], but will not be discussed in further detail here (for details, see [35,36]). The Young's modulus shows a slight increase there as well, but still in a negligibly regime. Especially when taking a closer look at the Young's modulus in Fig. 6b, an overlap is clearly visible for all conditions.

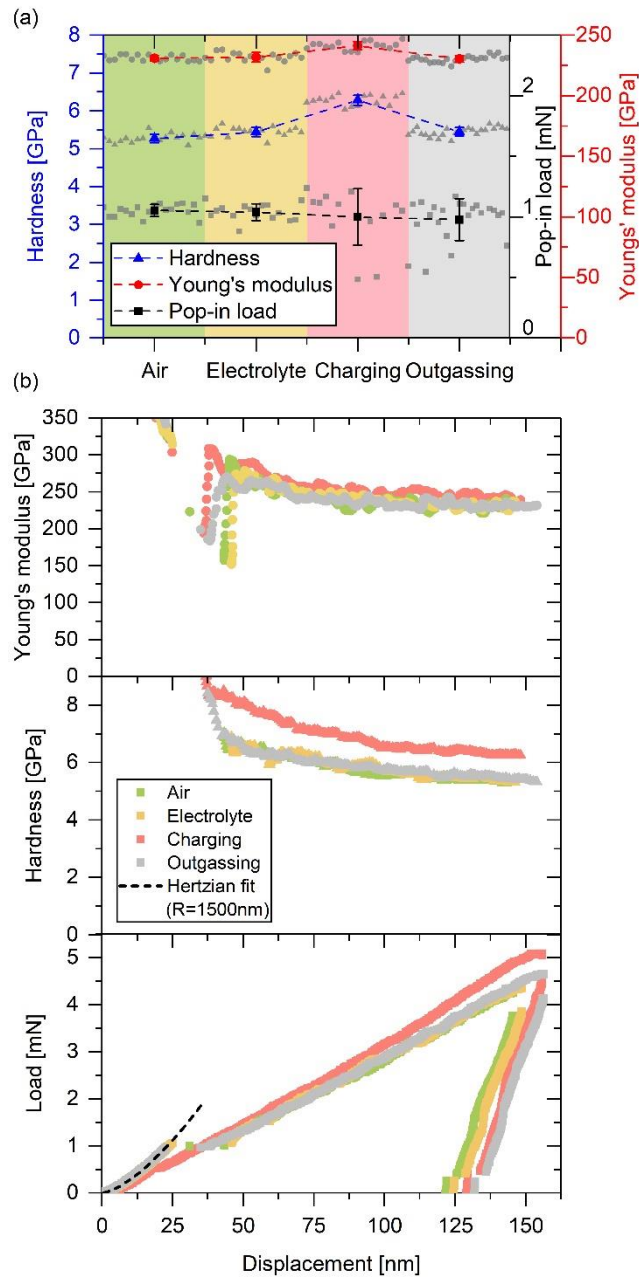


Fig. 6 (a) Averaged nanomechanical properties for SA sample in situ ECNI including Young's modulus, hardness and pop-in load analysis; (b) example load-displacement curves as well as hardness and Young's modulus over indentation depth for all four steps of ECNI (see text).

The results for the API sample are presented in Fig. 7 in the same manner. The pop-in load was not evaluated because of the influence of precipitates, which can act as favourable sites for the dislocation nucleation by lowering the necessary activation energy. Therefore, these nucleation events are no longer representative for a homogeneous dislocation nucleation. In air, a hardness of $8.03 \text{ GPa} \pm 0.11 \text{ GPa}$ is reached. The hardness reference value for the uncharged sample in the electrolyte is $7.88 \text{ GPa} \pm 0.16 \text{ GPa}$. After cathodic charging the hardness increases about 5.5% to $8.31 \text{ GPa} \pm 0.26 \text{ GPa}$. Outgassing by anodic discharging for 2 h leads to a decrease down to $8.01 \text{ GPa} \pm 0.44 \text{ GPa}$. At the same time the Young's modulus stays more or less constant over the whole experiment with just a slight decrease within the standard deviation for the charging section. Exemplary nanoindentation data shown in Fig. 7b confirm the hardness increase, particularly also visible in the higher maximum load in the load–displacement curve. A perfect overlap of Young's modulus curves is received over the total indentation depth for all four conditions. Pop-in events are still present for some indents, confirming a sufficient sample preparation exhibiting a low surface roughness and a low dislocation density.

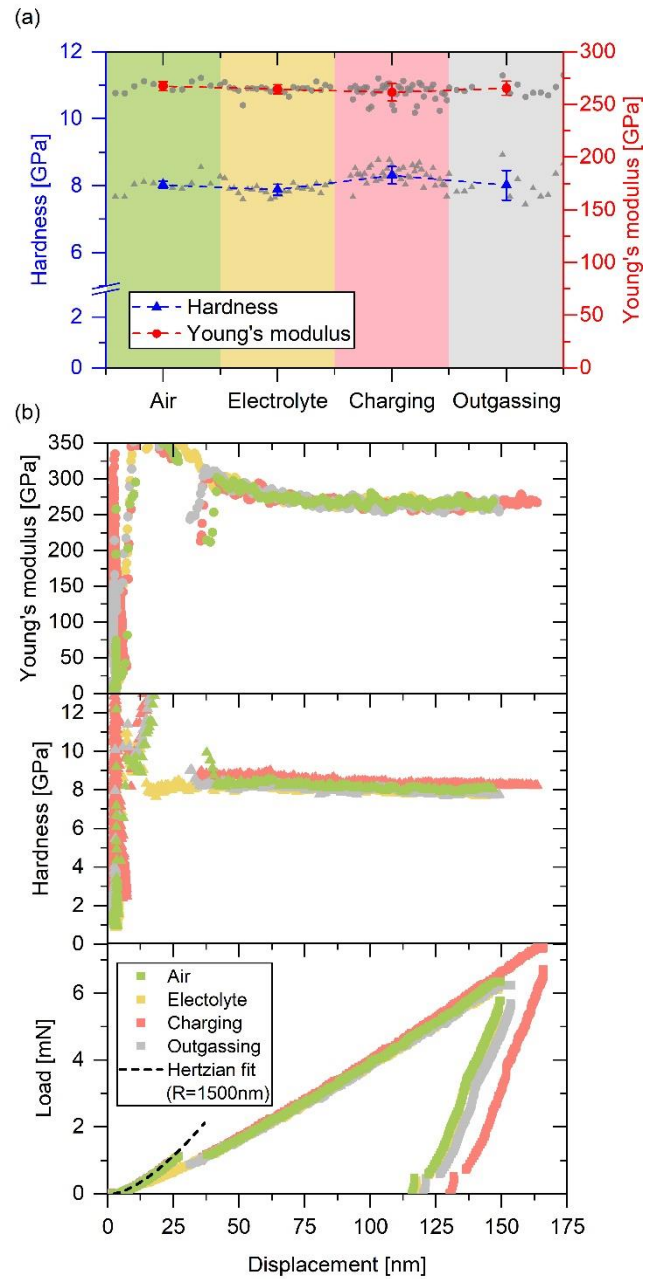


Fig. 7 (a) Averaged nanomechanical properties of the API sample during in situ ECNI including Young's modulus and hardness as well as (b) example load-displacement curves, hardness and Young's modulus over the indentation depth for all four steps of ECNI (see text).

4. Discussion

Surface preparation plays an important role in obtaining reliable nanoindentation data, especially when using the pop-in load as an evaluation criterion. Therefore, we first want to consider possible surface effects during ECNI experiments. Regarding our testing procedure surface changes can occur in different segments of the experiments. First, a deformation layer can remain from the mechanical preparation. By using OP-S polishing as the last mechanical-chemical preparation step, a mild ablation is achieved. A final electropolishing procedure removes the surface layer, which may contain dislocations. A good indicator of an adequate surface preparation is the occurrence of the initial pop-in [33]. For indentations in a coarse-grained material with overall low dislocation density, the pop-in corresponds to the first dislocation nucleation and can also be associated with the theoretical strength of a material [18,37]. Assuming a quasi-dislocation free volume under the indenter tip, the initial pop-in load can be directly correlated to the maximum shear stress τ_{max} necessary for homogenous dislocation nucleation:

$$\tau_{max} = 0.31 \left(\frac{6E_r^2}{\pi^3 R^2} P_{Pop-in} \right)^{1/3}, \quad (1)$$

where P_{Pop-in} is the pop-in load, E_r the reduced modulus and R the tip radius of the indenter tip, as proposed in Eq. (1). Since the SA and API samples show an initial pop-in behaviour, a sufficient surface preparation can be assumed. When calculating the theoretical strength according to equation (1) for the SA sample, a maximum shear stress τ_{max} of approximately 5 GPa is obtained. This value lies a bit below the literature value for nickel with 8 GPa [38]. For the API sample, calculations including pop-in loads are not reasonable, since precipitations promote heterogeneous dislocation nucleation and, therefore lower the pop-in loads. Generally, the pop-in load is influenced by the indentation spacing itself, which was set to a sufficient distance in this work [39].

The electrochemical charging procedure might lead to a surface modification. For these experiments corrosion should not appear during normal contact of the electrolyte and the sample surface for both the cathodic or anodic potential. One possible method to exclude surface changes during the charging procedure is to ensure a stable charging current or potential. Figure

3b shows a smooth development of each part of the electrochemical measurement, which again ensures a proper surface condition. Another indicator is the pattern quality of the EBSD after testing, which also indicates the presence of a good quality surface (Fig. 2b).

Slip steps only occurred on the electropolished surface of the SA sample after hydrogen charging; this might influence the measured mechanical properties. The sample surface is a fundamental requirement for the pop-in analysis as mentioned above. All possible irregularities, which differ from the perfect crystal lattice, can lead to a reduction in pop-in load by lowering the activation energy for dislocation nucleation. Such irregularities for example can be pre-existing dislocations, precipitations as well as enhanced surface roughness by slip steps. The slip steps can act as sites with higher stress concentration and therefore are facilitating the dislocation emission [18]. Immediately after applying a current density of $-500 \mu\text{A}/\text{cm}^2$, the standard deviation of the pop-in load increases and does not drop anymore as shown in Fig. 6a. The occurring slip steps are a possible explanation for the high scatter in pop-in data. When the indenter tip hits near a surface step, it is a more favourable site for dislocation nucleation than the defect-free crystal underneath [40]. Since the steps are not reversible, as seen by the laser confocal microscope image in Fig. 4b, and the surface roughness is increased, also after outgassing no recovery of the pop-in load scattering is observed.

By analysing the orientation deviation map in Fig. 5c, it is obvious that an irreversible plastic deformation takes place, which is depicted by the green area with higher misorientation near the grain boundary. In these areas, however, the dislocations have less possibility to exit the material, because the grain boundary inhibits the free motion of dislocations. When comparing the calculated slip systems with maximum Schmid factors for loading in the z-direction from the EBSD data [32], a correlation can be seen with the slip lines visible in the laser confocal microscope image. All these findings lead to the assumption that the present residual stresses are sufficient to induce irreversible slip traces. When looking for possible explanations for this induced deformation, different explanations can be found in the literature. First, Barnoush and Zamanzade [41] reported such hydrogen-induced surface steps in an austenite phase of a super duplex steel. They interpreted the residual stresses from quench annealing responsible for the occurrence of slip steps, since the hydrogen lowers the required stress to activate these pre-existing dislocations. Similar observations were made by Wang et al. [21] during ECNI of a HEA.

For higher cathodic potentials, they detected irreversible slip steps originating from the hydrogen-induced internal stresses as well as the promotion of dislocation nucleation by lowering the dislocation formation energy. Consequently, the corresponding pop-in loads and also their Young's modulus, calculated from the Hertzian fit, are permanently lowered by the higher surface roughness.

After discussing the influence of surface steps on the pop-in load, we interpret the changes in hardness for both heat treatment conditions. The SA sample shows an obvious increase of 15% from the reference hardness caused by the cathodic hydrogen charging. By measuring the outgassed condition, it is evident that the hardness is fully recovered compared with the pop-in load. Therefore, the hardness is not influenced by the higher surface roughness caused by the surface steps and the generated dislocations. This observation can be explained by the fact that the plastic deformation induced by hydrogen charging is very small compared with the indentation-induced plastic deformation. Furthermore, the hardness is determined from the CSM signal between 100 nm and 130 nm and hence is obtained at a greater depth of the material. By modelling the elastoplastic part of load–displacement curves with the Tabor relation based on the Nix-Gao model and taking into account the underlying lattice friction, Wang et al. [21] proposed an increase in lattice friction by the dissolved hydrogen. This increase can be linked with hydrogen acting as a Cottrell atmosphere [9] and retarding the dislocation motion, which leads to an measurable increased hardness in ECNI experiments.

As the Young's modulus calculated also shows a slight increase, possible influences that might originate from artificial phenomena such as a pile-up formation [42] should be taken into account. Therefore, a pile-up correction according to Joslin and Oliver [43] can be used to reduce the dominant influence of surface roughness or pile up-formation. By applying their correction model and assuming a constant Young's modulus from the literature, a corrected hardness of $5.79 \text{ GPa} \pm 0.06 \text{ GPa}$ can be calculated for the charged SA specimen. This correction reduces the overall hardness increase compared with the electrolyte to 6.0%, but still lies above the electrolyte reference value and hence can be directly contributed to the dissolved hydrogen in the sample.

Compared with the SA sample, the API specimen shows no hydrogen-induced surface steps and no changes in Young's modulus. Therefore, no corrections of Young's modulus or hardness are necessary. The influence of the dissolved hydrogen on the hardness increase amounts to 5.5%. Figure 8 summarizes the Young's modulus and hardness data for both heat treatments. The SA sample shows a more pronounced hardness increase when the uncorrected data are used. The effect of hydrogen as a Cottrell atmosphere seems to be less pronounced in the API sample, since precipitations can act as favourable sites for higher hydrogen concentrations. Therefore, less hydrogen can accumulate at the mobile dislocation to inhibit their motion. When comparing the absolute hardness increase of the corrected SA sample with the API sample, it is almost equal with approximately 0.5 GPa. By comparing the Young's moduli for both samples, a difference of around 30 GPa is recorded. This can be attributed to the different indented orientations. Nickel shows a higher Young's modulus in the (1 1 1) direction than in the (1 0 0) direction, which corresponds quantitatively to the orientations of the indented grains [44].

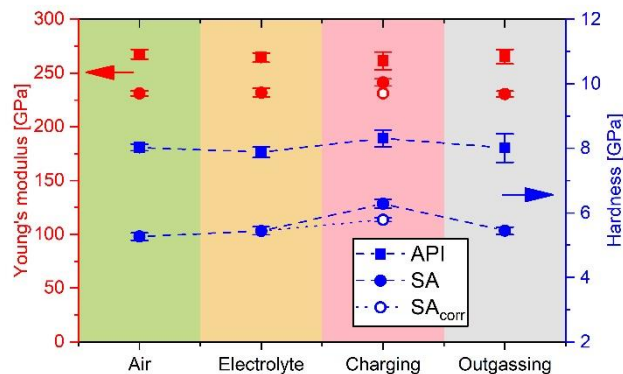


Fig. 8 Comparison of SA and API data regarding Young's modulus and hardness (see text).

5. Summary

The main findings and the outcome of the presented work can be summarized as follows.

- An electrochemical hydrogen charging setup for a nanoindentation platform was designed and established.
- Electrochemical measurements were performed to ensure appropriate surface integrity without corrosion.
- The nickel-based alloy 725 was tested in two different heat treatments, and changes in nanomechanical properties were investigated. The solution-annealed sample showed a somewhat larger hardness increase around 15%, which can be contributed to the effect of hydrogen acting as Cottrell atmosphere. For the precipitation-hardened sample, more hydrogen can be stored at the precipitations and therefore inhibition of dislocation as well as the hardness increase is less pronounced with a hardness increase of 5%.
- No reliable analysis of pop-in loads was possible on solution-annealed sample due to the hydrogen-induced surface steps. These steps led to an irreversible plastic deformation as revealed by EBSD misorientation maps. Therefore, the reduced pop-in load is more likely a consequence of the generated dislocations and surface steps than of the dissolved hydrogen.

Acknowledgements

Open access funding provided by Montanuniversität Leoben. Financial support by the Austrian Federal Government (837900) within the framework of the COMET Funding Programme (MPPE, Project, A2.32) and by the European Research Council under Grant Number 340185 is appreciated.

References

- [1] Nice, P. Strong, R., W.M. Bailey, G. Rorvik, J.H. Olsen, T.G. Mobberley, Hydrogen Embrittlement Failure of a PH Nickel Alloy Subsurface Safety Valve Component Installed in a North Sea Seawater Injection Well, Corrosion Conference and Expo 2014 3892 (2014) 1–16.
- [2] Z. Tarzimoghadam, D. Ponge, J. Klöwer, D. Raabe, Hydrogen-assisted failure in Ni-based superalloy 718 studied under in situ hydrogen charging, *Acta Mater.* 128 (2017) 365–374.
- [3] S.P. Lynch, Hydrogen embrittlement phenomena and mechanisms, *Corrosion Reviews* 30 (2012) 105–123.
- [4] R.A. Oriani, P.H. Josephic, Equilibrium aspects of hydrogen-induced cracking of steels, *Acta Metallurgica* 22 (1974) 1065–1074.
- [5] A. Troiano, Case Institute of Technology., Hydrogen embrittlement and stress corrosion cracking: a Troiano Festschrift, American Society for Metals, Metals Park Ohio, 1984.
- [6] P.J. Ferreira, I.M. Robertson, H.K. Birnbaum, Hydrogen effects on the interaction between dislocations, *Acta Materialia* 46 (1998) 1749–1757.
- [7] H.K. Birnbaum, P. Sofronis, Hydrogen-enhanced localized plasticity—a mechanism for hydrogen-related fracture, *Materials Science and Engineering A* 176 (1994) 191–202.
- [8] W. Xie, X. Liu, W. Chen, H. Zhang, Hydrogen hardening effect in heavily deformed single crystal α -Fe, *Computational Materials Science* 50 (2011) 3397–3402.
- [9] J. Song, W.A. Curtin, Mechanisms of hydrogen-enhanced localized plasticity, *Acta Mater.* 68 (2014) 61–69.
- [10] S.P. Lynch, Environmentally assisted cracking: Overview of evidence for an adsorption-induced localised-slip process, *Acta Metallurgica* 36 (1988) 2639–2661.
- [11] S. Lynch, Discussion of some recent literature on hydrogen-embrittlement mechanisms: addressing common misunderstandings, *Corrosion Reviews* 37 (2019) 136.
- [12] O. Barrera, D. Bombac, Y. Chen, T.D. Daff, E. Galindo-Nava, P. Gong, D. Haley, R. Horton, I. Katzarov, J.R. Kermode, C. Liverani, M. Stopher, F. Sweeney, Understanding and mitigating hydrogen embrittlement of steels: a review of experimental, modelling and design progress from atomistic to continuum, *Journal of Materials Science* 53 (2018) 6251–6290.
- [13] A. Barnoush, H. Vehoff, Electrochemical nanoindentation, *Scripta Mater.* 55 (2006) 195–198.
- [14] X. Fang, A. Kreter, M. Rasinski, C. Kirchlechner, S. Brinckmann, C. Linsmeier, G. Dehm, Hydrogen embrittlement of tungsten induced by deuterium plasma: Insights from nanoindentation tests, *J. Mater. Res.* 33 (2018) 3530–3536.
- [15] A. Barnoush, H. Vehoff, Recent developments in the study of hydrogen embrittlement, *Acta Mater.* 58 (2010) 5274–5285.
- [16] A. Barnoush, M. Asgari, R. Johnsen, Resolving the hydrogen effect on dislocation nucleation and mobility by electrochemical nanoindentation, *Scripta Mater.* 66 (2012) 414–417.

- [17] A. Barnoush, H. Vehoff, In situ electrochemical nanoindentation, *Corrosion Science* 50 (2008) 259–267.
- [18] M. Göken, M. Kempf, Pop-Ins in Nanoindentations—The Initial Yield Point, *Zeitschrift für Metallkunde* 92 (2001) 1061–1067.
- [19] G. Stenerud, R. Johnsen, J.S. Olsen, J. He, A. Barnoush, Effect of hydrogen on dislocation nucleation in alloy 718, *Int. J. Hydrogen Energy* 42 (2017) 15933–15942.
- [20] D. Wang, X. Lu, Y. Deng, X. Guo, A. Barnoush, Effect of hydrogen on nanomechanical properties in Fe 22Mn-0.6C TWIP steel revealed by in-situ electrochemical nanoindentation, *Acta Materialia* 106 (2019) 618–629.
- [21] D. Wang, X. Lu, Y. Deng, Di Wan, Z. Li, A. Barnoush, Effect of hydrogen-induced surface steps on the nanomechanical behavior of a CoCrFeMnNi high-entropy alloy revealed by in-situ electrochemical nanoindentation, *Intermetallics* 114 (2019) 106605.
- [22] Y. Zhao, D.-H. Lee, J.-A. Lee, W.-J. Kim, H.N. Han, U. Ramamurty, J.-Y. Suh, J. Jang, Hydrogen-induced nanohardness variations in a CoCrFeMnNi high-entropy alloy, *Int. J. Hydrogen Energy* 42 (2017) 12015–12021.
- [23] Y. Zhao, J.-M. Park, D.-H. Lee, E.J. Song, J.-Y. Suh, U. Ramamurty, J. Jang, Influences of hydrogen charging method on the hydrogen distribution and nanomechanical properties of face-centered cubic high-entropy alloy: A comparative study, *Scripta Materialia* 168 (2019) 76–80.
- [24] S.K. Lawrence, B.P. Somerday, M.D. Ingraham, D.F. Bahr, Probing the Effect of Hydrogen on Elastic Properties and Plastic Deformation in Nickel Using Nanoindentation and Ultrasonic Methods, *Jom* 70 (2018) 1068–1073.
- [25] N. Kheradmand, R. Johnsen, J.S. Olsen, A. Barnoush, Effect of hydrogen on the hardness of different phases in super duplex stainless steel, *Int. J. Hydrogen Energy* 41 (2016) 704–712.
- [26] K. Durst, V. Maier, Dynamic nanoindentation testing for studying thermally activated processes from single to nanocrystalline metals, *Current Opinion in Solid State and Materials Science* 19 (2015) 340–353.
- [27] V. Maier-Kiener, K. Durst, Advanced Nanoindentation Testing for Studying Strain-Rate Sensitivity and Activation Volume, *JOM* 69 (2017) 2246–2255.
- [28] E. Epler, Mechanical Properties of Lithiumion Batteryelectrodematerials at Different States of Charge. Ph.D. thesis, Göttingen, 2015.
- [29] W.C. Oliver, G.M. Pharr, An improved technique for determining hardness and elastic modulus using load and displacement sensing indentation experiments, *J. Mater. Res.* 7 (1992) 1564–1583.
- [30] A. Leitner, V. Maier-Kiener, D. Kiener, Essential refinements of spherical nanoindentation protocols for the reliable determination of mechanical flow curves, *Materials & Design* 146 (2018) 69–80.

- [31] P. Feldner, B. Merle, M. Göken, Determination of the strain-rate sensitivity of ultrafine-grained materials by spherical nanoindentation, *J. Mater. Res.* 32 (2017) 1466–1473.
- [32] F. Bachmann, R. Hielscher, H. Schaeben, Texture Analysis with MTEX – Free and Open Source Software Toolbox, *SSP* 160 (2010) 63–68.
- [33] Z. Wang, H. Bei, E.P. George, G.M. Pharr, Influences of surface preparation on nanoindentation pop-in in single-crystal Mo, *Scripta Mater.* 65 (2011) 469–472.
- [34] W.D. Nix, H. Gao, Indentation size effects in crystalline materials: A law for strain gradient plasticity, *Journal of the Mechanics and Physics of Solids* 46 (1998) 411–425.
- [35] M. Rester, C. Motz, R. Pippan, Indentation across size scales – A survey of indentation-induced plastic zones in copper {111} single crystals, *Scripta Materialia* 59 (2008) 742–745.
- [36] D. Kiener, W. Grosinger, G. Dehm, R. Pippan, A further step towards an understanding of size-dependent crystal plasticity: In situ tension experiments of miniaturized single-crystal copper samples, *Acta Materialia* 56 (2008) 580–592.
- [37] K.L. Johnson, *Contact Mechanics*, Cambridge University Press, 2012.
- [38] A. Barnoush, H. Vehoff, In situ electrochemical nanoindentation of Ni (111) single crystal, *J. Mater. Res.* 97 (2006) 1224–1229.
- [39] J. Li, G. Dehm, C. Kirchlechner, How close can indents be placed without risking an erroneous pop-in statistics?, *Materialia* 7 (2019) 100378.
- [40] D.B. Shan, Multiscale simulation of surface step effects on nanoindentation, *Materials Science and Engineering: A* 412 (2005) 264–270.
- [41] A. Barnoush, M. Zamanzade, H. Vehoff, Direct observation of hydrogen-enhanced plasticity in super duplex stainless steel by means of in situ electrochemical methods, *Scripta Materialia* 62 (2010) 242–245.
- [42] A. Bolshakov, G.M. Pharr, Influences of pileup on the measurement of mechanical properties by load and depth sensing indentation techniques, *J. Mater. Res.* 13 (1998) 1049–1058.
- [43] D.L. Joslin, W.C. Oliver, A new method for analyzing data from continuous depth-sensing microindentation tests, *J. Mater. Res.* 5 (1990) 123–126.
- [44] M. Yamamoto, The elastic constants of nickel single crystals, *Journal of the Japan Institute of Metals* 6 (1942) 331–338.

Publication B

**Rate-dependent plastic deformation behaviour in a
nickel-base alloy under hydrogen influence**

**Anna Sophie Ebner, Ernst Plesiutchnig, Helmut Clemens,
Reinhard Pippan, Verena Maier-Kiener**

International Journal of Hydrogen Energy, 46 (2021) 38132-38143

Rate-dependent plastic deformation behaviour in a nickel-base alloy under hydrogen influence

Anna Sophie Ebner¹, Ernst Plesiutchnig², Helmut Clemens¹, Reinhard Pippan³,
Verena Maier-Kiener¹

¹ Department of Materials Science, Montanuniversität Leoben, Leoben, Austria

² Voestalpine Böhler Edelstahl GmbH & Co KG, Kapfenberg, Austria

³ Erich Schmid Institute for Materials Science, Austrian Academy of Sciences, Leoben, Austria

Keywords: Electrochemical nanoindentation, Nanoindentation strain rate jump test, Nickel-base alloy, Hydrogen charging

Abstract

Despite a lot of research activities, the influence of hydrogen on the plastic deformation process is controversially discussed and often underestimated. Therefore, in this work strain rate jump tests were performed, using an electrochemical nanoindentation setup to investigate the deformation processes in a nickel-based alloy 725 under the influence of hydrogen, with the aim of determining thermally activated parameters such as strain rate sensitivity and activation volume. A hydrogen-induced hardness increase of about 8% was detected for all applied strain rates. The measured increase in strain rate sensitivity and the decrease in activation volume could be related to short-range order effects, which can lead to a more localized deformation. Furthermore, the optical evaluation of the remaining imprints showed a clear change in the formation of the plastically deformed zone during hydrogen charging. These insights into the deformation behaviour give further understanding regarding hydrogen-induced localized plasticity.

1. Introduction

Over the last 25e30 years, starting with the invention of the Oliver and Pharr method [1] in the year 1992, nanoindentation became a versatile tool in the materials science community and is indispensable for testing mechanical properties on a local nano-sized scale.

Early works primarily dealt with standard measurements of hardness and Young's modulus, for which the method was originally designed for to, e.g. basically characterize metals, bio materials, thin films or multi-phase materials. Over the years the method was continuously improved by the researchers themselves as well as by the nanoindenter manufactures. A significant break-through was achieved when dynamic measurement protocols allowed the continuous measurement of the stiffness over the whole indentation depth [2–4]. In this way nanoindentation was extended to a depth sensing method.

Due to its localized testing and the versatile application fields lots of advanced techniques were invented for in-depth analysis of the microstructure of pure metals, alloys and

Complex material systems, as multi-phase or multi-component materials. Microstructures as e.g. grain boundaries and precipitates, play an important role in tailoring material properties as strength and ductility, two of the most important parameters for constructional and engineering purposes. Both parameters, and especially ductility, is highly affected by the presence of hydrogen and is the main issue, when dealing with hydrogen embrittlement in technical environments as subsea and oil and gas industry [5]. Therefore, the main aim is the material improvement to prevent failure during the lifetime of application. Two main mechanisms, which can contribute to macroscopic failure due to the presence of hydrogen, and which can coexist next to each other is the brittle failure due to decohesion and the failure dominated by dislocation-driven plastic deformation. These two types can be both separately investigated with small scale testing techniques. On the one hand brittle fracture can be explored with micro-cantilever bending to investigate standard fracture-mechanical properties and parameters [6–8], as well as the influence of hydrogen on this fracture behaviour of grain interior and boundaries can be examined [9–12]. Secondly, plastic deformation, which is not directly associated with embrittlement, can be explored through nanoindentation and can be used in

general for studying the slip transfer through a grain boundary [13] or to determine the hardening behaviour from a flow curve with spherical nanoindentation [14].

Recent research [15–18], which investigated the influence of hydrogen with nanoindentation, focused on conventional hardness measurements analysed according to Oliver and Pharr [1] as well as on the evaluation of homogenous dislocation nucleation, represented by the first pop-in event in the nanoindentation load-displacement curve. By using an electrochemical nanoindentation setup, which is additionally equipped with a continuous stiffness measurement (CSM) option, as described in Ref. [19], a broader field including plastic deformation related parameters can be explored. This opens the possibility to implement more advanced nanoindentation methods such as strain rate jump tests [20]. By abruptly changing the indentation strain rate during the indentation process, strain rate dependent material properties can be calculated directly from a single experiment at a given position with limited thermal drift due to reduced indentation times. This allows the calculation of the strain rate sensitivity and the activation volume. In combination with reduced sample volume, preparation and time efforts, these experiments can provide information on the acting deformation mechanisms, which also can give an insight on the role of plastic deformation during hydrogen embrittlement.

In general, coarse-grained face-centred cubic (fcc) metals exhibit a relatively small strain rate sensitivity, for pure metals close to zero, correspondingly paired with an activation volume in the range of $100e1000 b^3$, where b denotes the Burgers vector, indicating a plastic deformation mechanism through forest hardening [21,22]. In contrast, body-centered cubic (bcc) materials with a pronounced fraction of thermally activated stress contribution exhibit higher changes in hardness due to applied strain rate changes at low temperatures, resulting in a higher strain rate sensitivity and a comparatively lower activation volume of $1e10 b^3$, indicating a so-called Peierls-Nabarro mechanism [23,24].

Subject for the investigations in this study is a modified highly alloyed sea-water resistant nickel-base alloy 725 (UNS N07725), which is widely used within the oil & gas industry for aggressive chlorine and mixed sour environments [25]. Although a fcc crystal structure might tend to a less distinct strain rate sensitivity in the coarse grained state, it is reported, that a high alloying content can lead to an increase of the strain rate sensitivity, as it could be confirmed for different

highly alloyed fcc materials, such as austenitic stainless steels [26] or high entropy alloys (HEA) [27,28].

The application of strain rate jump tests for evaluation of the influence of hydrogen on the plastic deformation can therefore shed some light on the acting mechanisms in a smaller size regime than conventional macroscopic test methods [29–31]. Since macroscopic tensile tests [32] already showed an influence of strain rate changes on the susceptibility to hydrogen embrittlement, convincing results are expected for this small scale approach. In an ex-situ charging approach nanoindentation strain rate jump tests were performed for austenitic stainless steel samples [33]. However, by using an in-situ electrochemical charging setup, the problem of a decreasing hydrogen content (outgassing) of the specimen can be eliminated by ensuring a continuous supply of hydrogen during the nanoindentation tests. Consequently, in-situ testing is the preferable method in current researches [34–36] and the reason for recording the occurring changes during charging in an in-situ electrochemical nanoindentation setup. The tests were performed on four different grain orientations and experimental test conditions, and were also supplemented with optical evaluation methods to show characteristics of the slip processes and the pile-up formation.

2. Experimental methods

2.1. Material and preparation

The investigations were carried out on a laboratory scale melted and modified nickel-base alloy 725. After melting in a vacuum induction furnace and forging into a bar with 130 mm diameter, precipitation hardening was performed according to the American Petroleum Institute standard [37]. The heat treatment consists of two steps, starting with solution annealing at 1040°C for 2 h and subsequent water quenching. To precipitate the γ' and γ'' strengthening phases, the two stage aging was performed at 740°C and 620°C for 8 h at each temperature. A subsequent water quenching avoids unwanted phase formation and precipitation coarsening after aging. The resulting microstructure has a mean grain size of $162.3 \pm 4.6 \mu\text{m}$ and shows the presence of annealing twins, typical for nickel. For further investigations 12 mm diameter cylindrical samples with a height of 3 mm were produced via wire erosion. After cold embedding with Struers Epofix, samples were cut into final shape of $18 \times 18 \times 3 \text{ mm}^3$ to fit the dimensions of

the electrochemical cell. Subsequent metallographic preparation was performed with SiC paper up to a grit of 1200. Polishing was performed with 3 μm and 1 μm diamond paste and finished with colloidal silica suspension (Struers OP-S). To remove the remaining deformation layer, electropolishing with a methanolic H_2SO_4 solution (1 mol/l) was carried out in the Struers Lectropol. The parameters applied were 22 V for 40 s at an electrolyte temperature ranging between 10 and 15°C.

2.2. In-situ electrochemical nanoindentation

All electrochemical nanoindentation tests were performed using a custom-built electrochemical cell in a G200 nanoindenter platform (KLA, Milpitas, CA, USA) equipped with a diamond Berkovich indentation tip (Synthon-MDP, Nidau, Switzerland). For detailed description regarding assembly and calibration see Ref. [19].

The electrochemical setup used for charging consists of the Gamry 1010B potentiostat (Gamry Instruments Inc., Warminster, PA, USA) connected to a three-electrode cell setup with a platinum counter electrode, a $\text{Hg}/\text{Hg}_2\text{SO}_4$ reference electrode and the sample as working electrode. The electrochemical cell was filled with a glycerine-based electrolyte with phosphoric acid (85%) in a mixing ratio of 2:1 [38]. For minimizing recombination of H_2 gas bubbles 1 g/ $\text{CH}_4\text{N}_2\text{S}$ (Thiourea) was added.

To choose the appropriate potentials a cyclic polarization curve was recorded beforehand on an additional sample from -1500 mV up to 1500 mV, with a scanning rate of 3 mV/s. The resulting cyclic polarization curve is shown in Fig. 1 (a) indicating all used states for charging with dashed lines.

The electrochemical charging procedure itself comprises of four different parts. In the beginning the open circuit potential (OCP) is measured for 0.5 h, to ensure an equilibrium state of the electrochemical system. In order to avoid a pronounced bubble formation during in-situ nanoindentation, the hydrogen charging is divided into two parts. A 4 h precharging with a relatively high current density of $-500 \mu\text{A}/\text{cm}^2$ warrants a sufficient hydrogen content in the near surface region. During indentation the current density is lowered to $-10 \mu\text{A}/\text{cm}^2$ for less disturbances due to hydrogen bubbles. To remove the hydrogen for simulating an outgassed condition, the sample was kept at an anodic potential of 0 mV. The resulting electrochemical data

for the whole charging procedure is plotted in Fig. 1 (b). The stability in the measured data indicate an intact surface, which is vital for nanoindentation tests. Discontinuities in the recorded potential or current density can point towards corrosion or other surface modifications.

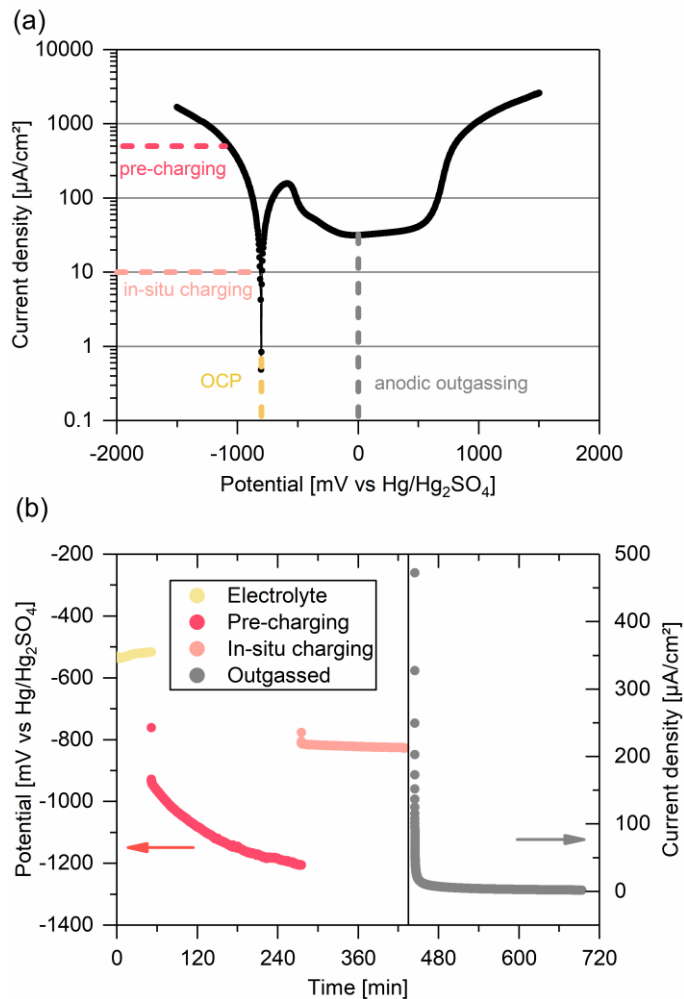


Fig. 1: a) Cyclic polarization curve for the used three-electrode setup. The used states for charging are marked with dashed lines; b) resulting current density and potential for applied hydrogen charging cycle, see text.

Prior to the electrochemical charging with hydrogen, reference indentations in air were performed to measure the initial mechanical properties. Sets of two indents for each of the four conditions were performed and marked in Fig. 2. In order to receive a reliable test result during one charging cycle four different grains (and orientations) were probed and for reference named with Pos1, Pos2, Pos3, and Pos4. The corresponding orientations are depicted in Fig. 2.

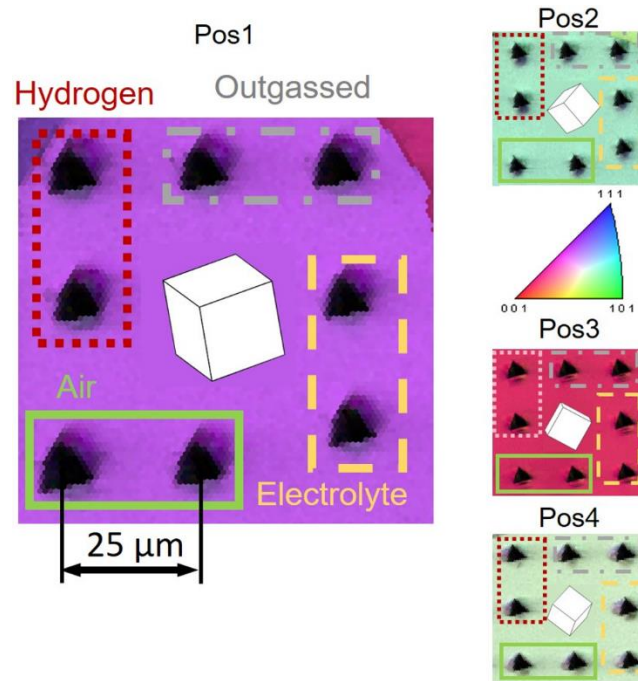


Fig. 2: Inverse pole figure maps with overlaid image quality for all 4 tested grain orientations. The inserts show the orientation of the corresponding unit cells. The four experimental conditions with the corresponding indents are depicted by the coloured framing. The indent spacing was 25 μm for all tests.

2.3. Nanoindentation strain rate jump tests

For measuring the local strain rate sensitivity, nanoindentation strain rate jump tests according to Maier et al. [20] were adapted for the in-situ electrochemical nanoindentation application. The total indentation depth was set to 1250 nm with an initial strain rate of 0.05 s^{-1} . One abrupt change in strain rate to 0.001 s^{-1} was performed at an indentation depth of 750 nm, while returning back to the initial strain rate at a depth of 1000 nm. All experiments were conducted with the CSM option to continuously measure the contact stiffness by superimposing an additional displacement signal with a frequency of 45 Hz and a harmonic amplitude of 2 nm. To reduce the influence of an indentation size effect, caused by the quasi single crystalline behaviour at low penetration depth, the hardness and the Young's modulus for all tested conditions were averaged before the strain rate jump at an indentation depth between 500 and 600 nm. In order to monitor the influence of the lower strain rate of 0.001 s^{-1} on the hydrogen-induced hardness increase, a second averaging section was chosen between 800 and 900 nm.

Fig. 3 gives an overview of an exemplary load-displacement curve for the used nanoindentation strain rate jump test protocol with the corresponding hardness and Young's modulus data for the investigated alloy 725. For calculating the values, which are characteristic for the underlying thermally activated deformation mechanisms, the occurring hardness difference due to the abrupt strain rate changes has to be determined. The insert in Fig. 3 demonstrates the used evaluation method. With the received hardness difference ΔH , the strain rate sensitivity m and the activation volume V^* can be calculated according to the following equations [26,39]:

$$m = \frac{\partial \ln \sigma}{\partial \ln \dot{\epsilon}} \sim \frac{\partial \ln H}{\partial \ln \dot{\epsilon}} = \frac{\partial \ln H_2 - \partial \ln H_1}{\partial \ln \dot{\epsilon}_2 - \partial \ln \dot{\epsilon}_1} \quad (1)$$

and

$$V^* = C^* \cdot \sqrt{3} \cdot k_B T \cdot \frac{\partial \ln \dot{\epsilon}}{\partial H} \sim C^* \cdot \sqrt{3} \cdot \frac{k_B T}{m \cdot H}, \quad (2)$$

where C^* is a constraint factor, which directly connects the stress to the hardness and is set to 2.8 [40]. Furthermore k_B , is the Boltzmann constant and T is the temperature (in our experiments: room temperature, 298 K). The Burgers vector for the investigated nickel-base alloy was assumed to be 0.25 nm[20,41].

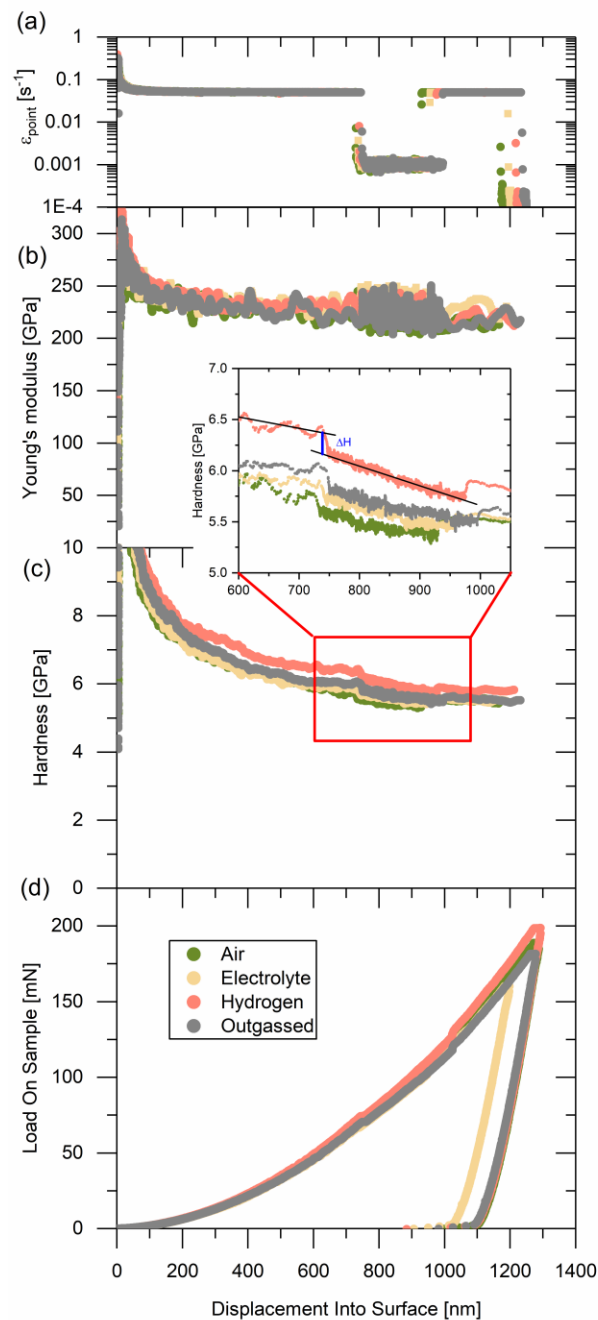


Fig. 3: Nanoindentation strain rate jump test data obtained for nickel-base alloy 725 for conditions air, electrolyte, hydrogen and outgassed, where a) shows the applied strain rate profile b) the constant Young's modulus with more data points during the lower strain rate and thus slower deformation, c) hardness development with the visible jumps and d) the resulting load-displacement curves. The insert displays the analysis of the hardness jump in more detail (black lines are drawn to guide the eye and are no linear fit to the data).

2.4. Optical evaluation methods

After successful nanoindentation experiments all remaining imprints were documented using a laser scanning confocal microscope (LSCM) of the type LEXT OLS4100 (Olympus, Tokyo, Japan). For further analysis regarding the plastically deformed zone and the corresponding pile-up formation, the height images were post-processed employing the software Gwyddion. For scanning electron microscopy (SEM) and electron backscatter diffraction (EBSD) a FEI 3D DualBeam workstation (Thermo Fisher Scientific, Waltham, MA, USA) equipped with an EDAX Hikari XP EBSD camera (EDAX Inc., Mahwah, NJ, USA) was used.

3. Results

3.1. Electrochemical in-situ jump tests

Before detailed analysis of the nanoindentation strain rate jump tests was conducted, the commonly used mechanical values of hardness and Young's modulus were evaluated to prove a successful charging procedure. The averaged mechanical properties for all four tested grain orientations are summarized in Fig. 4.

As expected, the Young's modulus remains constant throughout the whole experiment with approximately 240 ± 8 GPa in air, proving a stable experimental setup and a well-defined frame stiffness. In contrast, the hardness shows a clear increase of 7.9% from 6.18 ± 0.11 GPa in electrolyte to 6.66 ± 0.12 GPa in the hydrogen charged condition for the initial strain rate of 0.05 s^{-1} . After the anodic outgassing, the hardness drops back to 6.26 ± 0.06 GPa. When analysing the changes in mechanical properties for the lower strain rate of 0.001 s^{-1} a similar trend can be observed. The Young's modulus remains constant as well, despite an increasing standard deviation for the hydrogen charged condition, which is attributed to the higher data density at a lower strain rate [39]. The hardness shows a similar trend as for 0.05 s^{-1} , with an increase of 7.4% from 5.62 ± 0.05 GPa in electrolyte to 6.04 ± 0.12 GPa in hydrogen charged condition.

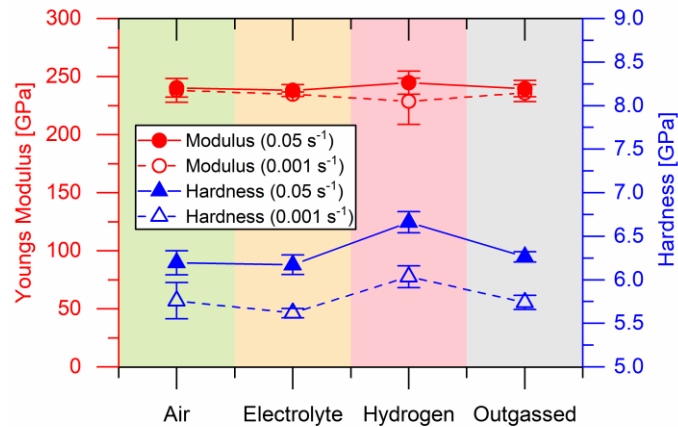


Fig. 4: Hardness and Young's modulus for all four conditions of the electrochemical nanoindentation experiment (averaged over all four positions). Full symbols belong to standard strain rate of 0.05 s^{-1} , blank ones to strain rate of 0.001 s^{-1} .

The results for the strain rate sensitivity m and the activation volume V^* from the nanoindentation strain rate jump tests are plotted in Fig. 5. Since the analysis of the hardness jumps, needed for calculation of m and V^* , is performed manually, the thereby obtained values are subjected to a larger scatter. Nevertheless, a trend is visible in strain rate sensitivity m as well as for the activation volume V^* . In average m increases from 0.0082 ± 0.0022 in uncharged condition of about 24.5% to 0.0102 ± 0.0028 , while the activation volume shows an opposite development by decreasing from $30.2 \pm 10.6 \text{ b}^3$ to $21.1 \pm 5.1 \text{ b}^3$, which corresponds to a reduction of 30.1%.

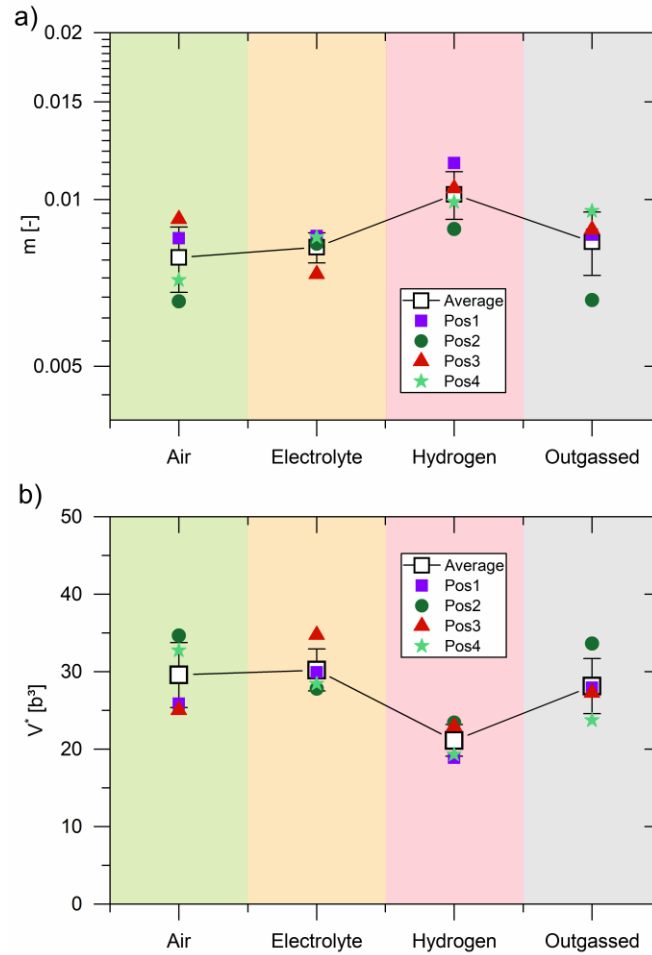


Fig. 5: Summary of nanoindentation strain rate jump test results for (a) strain rate sensitivity m and (b) activation volume V^* . Averaged values in black with standard deviation and for each individual position in colour without error bars for better visibility.

3.2. Evaluation of pile-ups, slip steps and the plastically deformed zone

The plastic zone was exemplary evaluated for four residual impressions of Pos4 by calculating the plastic zone radius r_{pZ} , the contact radius r_c as well as by analysing the slip step patterns. The results are summarized in Table 1, depicted in Fig. 6 and will be described in detail in the following paragraphs.

The plastic zone radius r_{pz} was estimated according to a theory derived by Lawn et al. [42], which takes into account the ratio between Young's modulus and hardness:

$$r_{pz} = \phi \left(\frac{E}{H} \right)^{1/3} \tan^{1/3}(\theta) h_f, \quad (3)$$

where ϕ and θ depend on the geometry of the Berkovich tip and are 3.64 for the geometry constant and 19.7° for the equivalent cone angle, respectively. Additional to the E/H ratio the remaining depth h_f of the indent must be extracted from the load-displacement data.

Table 1: Calculated plastic zone radius r_{pz} after Eq. (3) and measured contact radius r_c for the indents of Pos4 as shown in Fig. 6

	h_f [μm]	r_{pz} [μm]	r_c [μm]
Air	1.08 ± 0.01	9.36 ± 0.11	5.18 ± 0.09
Electrolyte	1.05 ± 0.01	9.16 ± 0.07	5.13 ± 0.02
Hydrogen	1.05 ± 0.01	9.13 ± 0.01	5.08 ± 0.02
Outgassed	1.06 ± 0.01	9.27 ± 0.10	5.24 ± 0.01

Fig. 6 shows one exemplary impression for each condition for the selected grain orientation Pos4. The corresponding coloured circles visualize the plastically deformed zones with the plastic zone radius r_{pz} calculated according to Eq. (3). The contact radius r_c is marked with a white dashed circle. When comparing both zones in Table 1 it suggests a smaller plastically deformed zone size present in hydrogen charged condition, as well as a smaller contact radius r_c .

Further, the arising slip steps at the three flanks of each Berkovich imprint were classified regarding their primary surface steps (solid lines), contrast (dashed lines = secondary surface steps) and assigned slip planes (same line colour). In the hydrogen charged condition, the number of activated slip systems present appears to be less, as visible in Fig. 6 (c), because of the missing dashed blue line at the upper left flank and the missing solid red line at the bottom flank, respectively. When taking a more precise look at the upper left flank of the hydrogen charged imprint a denser morphology for the primary slip steps in direction of the yellow line can be observed.

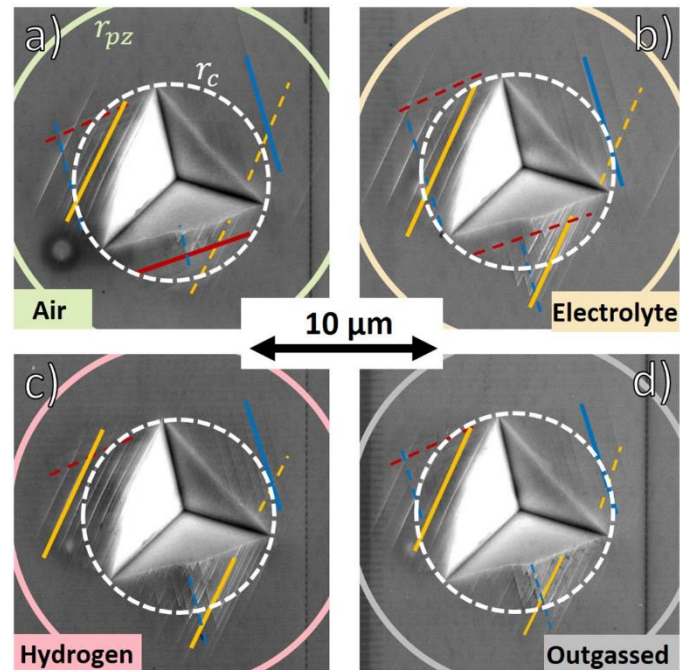


Fig. 6: Exemplary Berkovich impressions in one grain with identical orientation (Pos4) for each condition: a) air, b) electrolyte, c) hydrogen, and d) outgassed, with an indicated plastically deformed zone size (r_{pz} solid line, r_c white dashed line) as well as marked identified slip steps (for colour and line type explanation see corresponding text).

To quantify the changes in the plastically deformed zone, the remaining impressions were further evaluated by assessing the pile-up height and volume. The results for each grain for pile-up height and volume are summarized in Fig. 7. For this purpose, a threshold of 15 nm above the base level (sample surface) was chosen for confining the pile-up area, which is exemplarily illustrated with the purple mask in the insert in Fig. 7 (b). The pile-up height was traced by a line profile over the highest pile-up for all indents in each individual grain. An average value for the four different orientations cannot be given, since different crystallographic orientations lead to variations in the material response and thus in a crystal orientation dependent pile-up formation.

All positions show an increase in pile-up height for the impressions performed in the hydrogen charged condition. For Pos1, 2 and 4 a subsequent drop back after outgassing follows. However, for Pos3 this drop back cannot be seen. Accordingly, the pile-up volume shows a similar trend, but the aberration of Pos3 after outgassing is not as much pronounced.

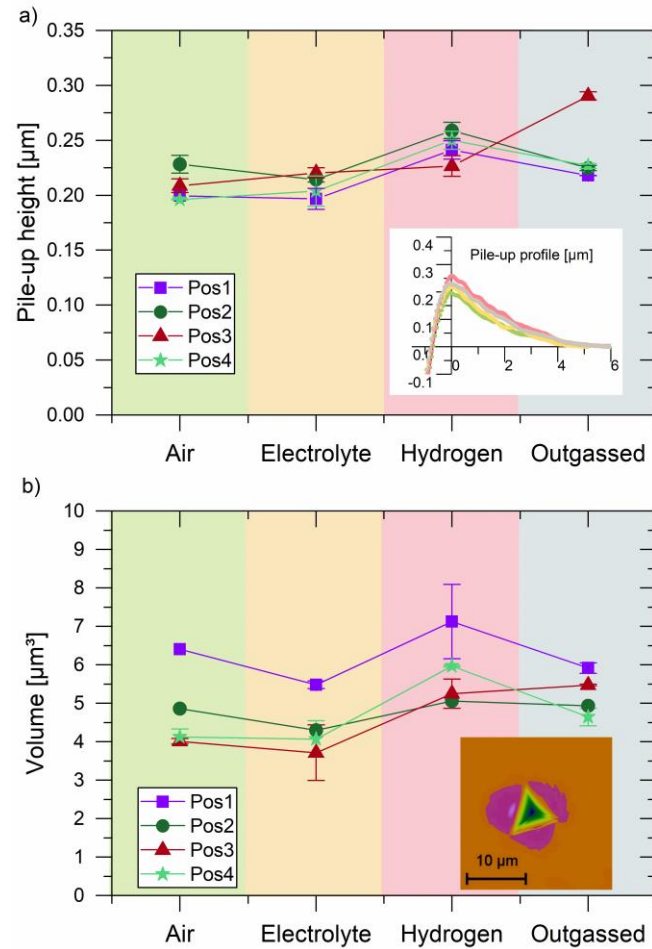


Fig. 7: Results of pile-up characterization by means of LSM: (a) shows maximum pile-up height from line profile of the most pronounced pile-up and (b) represents the pile-up volume around the entire imprint.

Besides identifying the crystallographic orientation via EBSD analysis, also the misorientation angle was detected for visualizing the indentation-induced deformation by assuming that the orientation differences arise from plastic deformation[13,43]. One exemplary indent for each condition is depicted in Fig. 8. For all uncharged conditions, misorientation differences are visible at all three flanks of the Berkovich imprint. The hydrogen charged condition shows a more noticeable change in deformation on the upper left flank and nearly no deformation for the bottom flank.

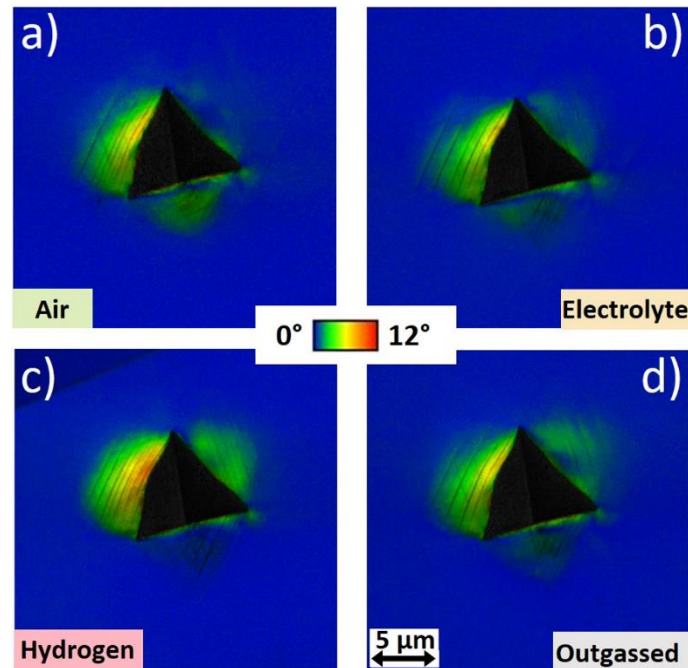


Fig. 8: Orientation angle deviation map with overlaid image quality for one exemplary indent in grain orientation Pos4 for each condition: a) air, b) electrolyte, c) hydrogen charged, and d) outgassed.

4. Discussion

The most commonly used value in classical electrochemical nanoindentation, beside the pop-in analysis, is the so-called hydrogen-induced hardness increase. In previous studies, it was revealed for more complex multi-phase material systems that the analysis of the pop-in load can be influenced by extrinsic conditions as, e.g. surface roughness, hydrogen induced surface steps, local stress as well as hydrogen concentrations at precipitates [19]. If conclusions about incipient plasticity [44–46] are drawn based on the initial pop-in, these extrinsic influences must be avoided as much as possible. As a consequence, materials with a homogenous microstructure and large grain sizes are better suitable for investigation of hydrogen influence on the onset of plasticity [47,48]. Therefore, in our study the change in hardness can give a better insight into the plastic deformation response of a precipitation hardened material. Because of the special, well-defined and adapted design of nanoindentation strain rate jump tests with only a small segment of low strain rate for the evaluation of the strain rate sensitivity, a large part of each indentation remains with the standard strain rate of 0.05 s^{-1} , which allows a reliable averaging of the hardness. To

minimize the influence of the indentation size effect, which leads to a continuous decrease of hardness over indentation depth in single crystalline and coarse grained metals, the continuously recorded mechanical properties (hardness and Young's modulus) were averaged between 500 and 600 nm for all indentations and conditions to allow a comparable data discussion. The hardness values, which are averaged over all four positions, exhibit a small standard deviation and thus emphasizes the validity of the measured hardness increase of 7.9%, which is visible in Fig. 4. The drop back for the outgassed condition points out a sufficient outgassing in the nanohardness affected zone.

The hydrogen-induced hardness increase at a lower strain rate of 0.001 s^{-1} is in a similar range as for the standard strain rate of 0.05 s^{-1} . Only a slight decrease of 0.5% occurs. Thus a less pronounced hydrogen-induced hardness increase for lower strain rates, as proposed by Hong et al. [33] for ex-situ charged austenitic (fcc) stainless steel samples, can be confirmed in this in-situ testing study even though it is less distinct for the nickel-base alloy 725. According to literature the increase in hardness can be attributed to classical solid solution strengthening [48–51], an increase in lattice friction [17,18] as well as an increase in slip planarity [52–54].

In contrast to the hardness, the Young's modulus stays constant over the whole experiment as expected due to the relative small hydrogen concentration, which evidences a stiff and well-calibrated setup and is depicted in Fig. 3 (b). The higher scattering during testing at slow strain rate can be ascribed to the higher data density in this regime [39].

Moreover, the advanced nanoindentation method of strain rate jump tests allows the calculation of both rate dependent deformation parameters, the strain rate sensitivity m and the activation volume V^* . Both provide significant information about thermally activated deformation processes as well as the dominating deformation mechanisms, such as Peierls-Nabarro mechanism, dislocation gliding or forest cutting. For coarse-grained fcc metals, a strain rate sensitivity close to zero is reported in literature for pure metals [55,26,39]. However, different variations in chemical composition and microstructure can change this behaviour. It is reported, that an increase in alloying elements, e.g. in high-alloyed systems such like HEAs, can result in an increase in lattice friction. In contrast, conventional pure fcc materials exhibit quite low lattice friction and thus are favourable to dislocation glide [28,27].

In this study the material consists of approx. 50 m% nickel and, therefore, has a quite high alloying content, which might explain the higher strain rate sensitivity of 0.0082 ± 0.0022 for the uncharged condition in comparison to pure coarse-grained nickel. Table 2 gives a comparison to literature values and displays a strain rate sensitivity in our current study, which is a factor of 2-8 times larger when compared to the coarse-grained state on pure nickel investigated by means of tensile tests as done by Dalla Torre et al. [56] and Vehoff et al. [41]. Most nanoindentation studies in the past were conducted on ultrafine-grained (ufg) or nanocrystalline (nc) nickel, hence comparison was done to the coarsest state investigated in the cited literature. In comparison to m values from nanoindentation on ufg and nc sample, our strain rate sensitivity is lower around a factor of $2e3$ times. The high strain rate sensitivity for ufg and nc materials can be explained by the large contribution of grain boundaries to the deformation mechanism, like grain boundary diffusion and dislocation glide-based plasticity [57]. A good comparability of the strain rate sensitivity is also found with the results for a nickel-base alloy 720 in uncharged condition as reported by Gopinath et al. [58], who performed tensile tests, and with the results for a equiatomic CrMnFeCoNi HEA derived from a nanoindentation study conducted by Maier-Kiener et al. [59].

With hydrogen charging the strain rate sensitivity even increases, which can indicate a further increase in lattice friction. For a HEA this increase in lattice friction due to hydrogen charging was also reported and calculated by Wang et al. [17] and is confirmed by our finding of an increasing strain rate sensitivity for alloy 725 in hydrogen charged condition.

Table 2: Comparison of strain rate sensitivity m for pure nickel and nickel containing alloys in this study and literature obtained by nanoindentation or bulk uniaxial (compression or tensile) tests

	Method	Material	Grainsize [μm]	m	V^* [b^3]
Present study	NI	Alloy 725	150	0.008	30
Maier et al. [20]	NI	nc Ni	0.025	0.019	14
	compression			0.016	17
Vehoff et al. [41]	tensile	mc Ni	> 10	0.002-0.003	1000-1400
Torre et al. [56]	tensile	Ni	> 1000	0.001-0.004	-
Gopinath et al. [58]	tensile	Alloy 720	11-22	0.009	-
Maier-Kiener et al. [59]	NI	fcc HEA	> 1000	0.008	69

abbreviations: nanocrystalline (nc), ultrafine grained (ufg), mc (microcrystalline), high entropy alloy (HEA), nanoindentation (NI), nickel (Ni)

The activation volume V^* of coarse-grained fcc materials ranges around $100 \cdot \text{b}^3$ for dislocation-dislocation interaction and can reach up to $\sim 1000 \cdot \text{b}^3$ in the case of forest hardening [21]. A lower activation volume between 1 and $10 \cdot \text{b}^3$ corresponds to the Peierls-Nabarro mechanism and is more common for bcc or hcp metals [60,61]. However, it can also be seen in ufg fcc materials, as pointed out in Table 2. With an activation volume of around $30 \cdot \text{b}^3$ the fcc nickel-base alloy 725 exhibits a quite low value, when compared to the coarse-grained nickel investigated by Vehoff [41], which even decreases further after hydrogen charging. According to literature this might be attributed to short-range effects resulting from solute atoms, which can promote planar slip and, therefore, can lead to localized deformation and the appearance of narrow slip bands as reported in Refs. [62,63]. Furthermore, a low activation volume can be an additional evidence for an increase in lattice friction [26].

The assumption of a possible change in deformation behaviour, indicated by a decrease in activation volume, leads to the detailed analysis of the remaining imprints and the slip step patterns around them. In general, the slip steps developing around indentation imprints in single grains, see Fig. 6, are very reproducible and can give insight on the occurring plastic flow and

deformation processes [64,65]. Wang et al. [18] already confirmed the influence of hydrogen on the size of the plastic zone and the pile-up formation during electrochemical nanoindentation on a TWIP steel with electron channelling contrast imaging. Similar findings can be seen in this study for the nickel-base alloy 725. The hydrogen leads to a shrinkage of the plastically deformed zone radius r_{pz} (see Table 1) by hindering dislocation motion, when acting as Cottrell atmosphere [66]. Especially for the upper left flank in Fig. 6 a change in slip step quantity and spacing can be observed. More slip steps are present in a smaller region, which leads to a denser appearance. This is an indicator of restricted cross-slip, which comes along with the enhanced planar slip predicted for the hydrogen-enhanced localized plasticity. Also micropillar compression experiments conducted on nickel-base alloy 725, showed denser slip step characteristics for hydrogen charged pillars, see Ref. [67]. But in literature also contradictory findings are present for ex-situ hydrogen testing. For example, an increase in slip step spacing and height was found in ex-situ experiments by Nibur et al. [52] for an austenitic stainless steel, which they also attributed to the slip planarity. They also found an increase in slip activity resulting from a reduced stress necessary for dislocation glide. However, Fig. 6 clearly shows the opposite behaviour for our investigated nickel-base alloy, pictured by missing slip steps for the left and the bottom Berkovich flank.

Beside the slip step pattern, also the pile-up behaviour sheds more light into the plastic deformation process. For both evaluation methods, via line profile of the most pronounced pile-up and through the sum of the total piled-up volume, an increase for the hydrogen charged condition can be seen for three out of four grains. One possible explanation of the divergent behaviour of Pos3 could be an underlying grain with different orientation, which influences the pile-up formation. Since EBSD only gives a 2D information of the surface, such an effect cannot be totally excluded. Nevertheless, the overall behaviour is in good agreement with the outcomes of Wang et al. [18] and Hong et al. [33], who also predicted an increase in pile-up height with hydrogen.

Another indicator of the amount of plastic deformation is the change of the misorientation angle as observed through EBSD analysis. This technique is often used for post-mortem analysis of the effect of hydrogen on the fatigue crack growth [43,68] In the case of nanoindentation no

distinct difference in localized deformation can be seen. Only the upper left flank in Fig. 6, which holds the main deformation, shows a higher misorientation angle, which can indicate a somehow higher amount of geometrically necessary dislocations in this region.

This study shows that the method of nanoindentation strain rate jump tests, in combination with hydrogen charging, gives the possibility to investigate rate dependent deformation processes, which can be related to the role of hydrogen in the plastic deformation process. With the combination of further investigation methods, in our case optical ones, such as SEM and LSCM, the consequences of this effect can be captured and visualized. As hydrogen embrittlement is a phenomenon, which takes place on different length scales and can be examined by different approaches [69], the strengths of each method should be kept in mind when interpreting the results with regard to the occurring deformation mechanisms.

Finally, it should be noted that such nanoindentation strain rate jump tests in combination with electrochemical charging can be improved by statistically verifying the results by performing a large number of indents in a significant coarser grained material to exclude grain orientation influences.

5. Discussion

In this study nanoindentation strain rate jump tests in an electrochemical setup were performed on the nickel-base alloy 725 to investigate the influence of hydrogen on hardness, strain rate sensitivity and activation volume. Additionally, the remaining Berkovich imprints were analysed by different optical methods, to visualize the plastically deformed zone and the pile-up formation. From the obtained results the following conclusions can be drawn:

- Hydrogen increases the measurable hardness for both applied strain rates in all tested grain orientations.
- The exposure of hydrogen leads to a change in the deformation-related parameters. The increase in strain rate sensitivity indicates an increase in lattice friction. The observed decrease of the activation volume suggests a promotion of planar slip, which leads to a more localized deformation.

- The analysis of the remaining Berkovich imprints showed a decrease in the plastically deformed zone, an increase in pile-up height and volume, as well as changes in the slip step characteristics as a consequence of hydrogen charging.
- All findings can be related to the appearance of hydrogen-enhanced localized plasticity.

Acknowledgements

The authors gratefully acknowledge the financial support under the scope of the COMET program within the K2 Center “Integrated Computational Material, Process and Product Engineering (IC-MPPE)” (Project No 859480). This program is supported by the Austrian Federal Ministries for Climate Action, Environment, Energy, Mobility, Innovation and Technology (BMK) and for Digital and Economic Affairs (BMDW), represented by the Austrian research funding association (FFG), and the federal states of Styria, Upper Austria and Tyrol.

References

- [1] W.C. Oliver, G.M. Pharr, An improved technique for determining hardness and elastic modulus using load and displacement sensing indentation experiments, *J. Mater. Res.* 7 (1992) 1564–1583.
- [2] J.B. Pethica, W.C. Oliver, Tip Surface Interactions in STM and AFM, *Phys. Scr. T19A* (1987) 61–66.
- [3] J.B. Pethica, W.C. Oliver, Mechanical Properties of Nanometre Volumes of Material: use of the Elastic Response of Small Area Indentations, *MRS Proceedings* (1989) 13–23.
- [4] J. Hay, P. Agee, E. Herbert, Continuous stiffness measurement during instrumented indentation testing, *Experimental Techniques* 34 (2010) 86–94.
- [5] Nice, P. Strong, R., W.M. Bailey, G. Rorvik, J.H. Olsen, T.G. Mobberley, Hydrogen Embrittlement Failure of a PH Nickel Alloy Subsurface Safety Valve Component Installed in a North Sea Seawater Injection Well, *Corrosion Conference and Expo 2014* 3892 (2014) 1–16.
- [6] G. Dehm, B.N. Jaya, R. Raghavan, C. Kirchlechner, Overview on micro- and nanomechanical testing: New insights in interface plasticity and fracture at small length scales, *Acta Mater.* 142 (2018) 248–282.
- [7] B.N. Jaya, C. Kirchlechner, G. Dehm, Can microscale fracture tests provide reliable fracture toughness values?, *J. Mater. Res.* 30 (2015) 686–698.

- [8] D. Kiener, C. Motz, T. Schöberl, M. Jenko, G. Dehm, Determination of Mechanical Properties of Copper at the Micron Scale, *Adv. Eng. Mater.* 8 (2006) 1119–1125.
- [9] T. Hajilou, Y. Deng, B.R. Rogne, N. Kheradmand, A. Barnoush, In situ electrochemical microcantilever bending test, *Scripta Mater.* 132 (2017) 17–21.
- [10] T. Hajilou, Y. Deng, N. Kheradmand, A. Barnoush, Hydrogen enhanced cracking studies on Fe-3wt%Si single and bi-crystal microcantilevers, *Philosophical Transactions of the Royal Society A: Mathematical, Physical and Engineering Sciences* 375 (2017).
- [11] Y. Deng, T. Hajilou, D. Wan, N. Kheradmand, A. Barnoush, In-situ micro-cantilever bending test in environmental scanning electron microscope, *Scripta Mater.* 127 (2017) 19–23.
- [12] Y. Deng, A. Barnoush, Hydrogen embrittlement revealed via novel in situ fracture experiments using notched micro-cantilever specimens, *Acta Materialia* 142 (2018) 236–247.
- [13] S. Jakob, A. Leitner, A. Lorich, M. Eidenberger-Schober, W. Knabl, R. Pippan, H. Clemens, V. Maier-Kiener, Influence of crystal orientation and Berkovich tip rotation on the mechanical characterization of grain boundaries in molybdenum, *Materials & Design* 182 (2019) 107998.
- [14] A. Leitner, V. Maier-Kiener, D. Kiener, Essential refinements of spherical nanoindentation protocols for the reliable determination of mechanical flow curves, *Materials & Design* 146 (2018) 69–80.
- [15] N. Kheradmand, R. Johnsen, J.S. Olsen, A. Barnoush, Effect of hydrogen on the hardness of different phases in super duplex stainless steel, *Int. J. Hydrogen Energy* 41 (2016) 704–712.
- [16] Y. Zhao, D.-H. Lee, J.-A. Lee, W.-J. Kim, H.N. Han, U. Ramamurty, J.-Y. Suh, J. Jang, Hydrogen-induced nanohardness variations in a CoCrFeMnNi high-entropy alloy, *Int. J. Hydrogen Energy* 42 (2017) 12015–12021.
- [17] D. Wang, X. Lu, Y. Deng, Di Wan, Z. Li, A. Barnoush, Effect of hydrogen-induced surface steps on the nanomechanical behavior of a CoCrFeMnNi high-entropy alloy revealed by in-situ electrochemical nanoindentation, *Intermetallics* 114 (2019) 106605.
- [18] D. Wang, X. Lu, Y. Deng, X. Guo, A. Barnoush, Effect of hydrogen on nanomechanical properties in Fe 22Mn-0.6C TWIP steel revealed by in-situ electrochemical nanoindentation, *Acta Materialia* 106 (2019) 618–629.
- [19] A.S. Ebner, S. Brinckmann, E. Plesiutchnig, H. Clemens, R. Pippan, V. Maier-Kiener, A Modified Electrochemical Nanoindentation Setup for Probing Hydrogen-Material Interaction Demonstrated on a Nickel-Based Alloy, *JOM* 72 (2020) 2020–2029.
- [20] V. Maier, K. Durst, J. Mueller, B. Backes, H.W. Höppel, M. Göken, Nanoindentation strain-rate jump tests for determining the local strain-rate sensitivity in nanocrystalline Ni and ultrafine-grained Al, *Journal of Materials Research* 26 (2011) 1421–1430.
- [21] C.D. Gu, J.S. Lian, Q. Jiang, W.T. Zheng, Experimental and modelling investigations on strain rate sensitivity of an electrodeposited 20 nm grain sized Ni, *New Journal of Physics* 40 (2007) 7440–7446.

- [22] K. Kumar, H. van Swygenhoven, S. Suresh, Mechanical behavior of nanocrystalline metals and alloys¹¹The Golden Jubilee Issue—Selected topics in Materials Science and Engineering: Past, Present and Future, edited by S. Suresh, *Acta Materialia* 51 (2003) 5743–5774.
- [23] D. Kiener, R. Fritz, M. Alfreider, A. Leitner, R. Pippan, V. Maier-Kiener, Rate limiting deformation mechanisms of bcc metals in confined volumes, *Acta Mater.* 166 (2019) 687–701.
- [24] V. Maier, A. Hohenwarter, R. Pippan, D. Kiener, Thermally activated deformation processes in body-centered cubic Cr – How microstructure influences strain-rate sensitivity, *Scripta Mater.* 106 (2015) 42–45.
- [25] O. El kebir, Comparison of hydrogen embrittlement of stainless steels and nickel-base alloys, *Int. J. Hydrogen Energy* 27 (2002) 793–800.
- [26] V. Maier-Kiener, K. Durst, Advanced Nanoindentation Testing for Studying Strain-Rate Sensitivity and Activation Volume, *JOM* 69 (2017) 2246–2255.
- [27] D.-H. Lee, I.-C. Choi, M.-Y. Seok, J. He, Z. Lu, J.-Y. Suh, M. Kawasaki, T.G. Langdon, J. Jang, Nanomechanical behavior and structural stability of a nanocrystalline CoCrFeNiMn high-entropy alloy processed by high-pressure torsion, *J. Mater. Res.* 30 (2015) 2804–2815.
- [28] Z. Wu, H. Bei, G.M. Pharr, E.P. George, Temperature dependence of the mechanical properties of equiatomic solid solution alloys with face-centered cubic crystal structures, *Acta Mater.* 81 (2014) 428–441.
- [29] X. Li, J. Zhang, Q. Fu, E. Akiyama, X. Song, Y. Wang, Q. Li, N. Zou, Tensile mechanical properties and fracture behaviors of nickel-based superalloy 718 in the presence of hydrogen, *Int. J. Hydrogen Energy* 43 (2018) 20118–20132.
- [30] F. Galliano, E. Andrieu, J.-M. Cloué, G. Odemer, C. Blanc, Effect of temperature on hydrogen embrittlement susceptibility of alloy 718 in Light Water Reactor environment, *Int. J. Hydrogen Energy* 42 (2017) 21371–21378.
- [31] F. Galliano, E. Andrieu, C. Blanc, J.M. Cloué, D. Connetable, G. Odemer, Effect of trapping and temperature on the hydrogen embrittlement susceptibility of alloy 718, *Materials Science and Engineering A* 611 (2014) 370–382.
- [32] Y. Momotani, A. Shibata, D. Terada, N. Tsuji, Effect of strain rate on hydrogen embrittlement in low-carbon martensitic steel, *Int. J. Hydrogen Energy* 42 (2017) 3371–3379.
- [33] Y. Hong, C. Zhou, Y. Zheng, L. Zhang, J. Zheng, X. Chen, Dependence of strain rate on hydrogen-induced hardening of austenitic stainless steel investigated by nanoindentation, *Int. J. Hydrogen Energy* (2019).
- [34] A. Massone, A. Manhard, A. Drexler, C. Posch, W. Ecker, V. Maier-Kiener, D. Kiener, Addressing H-Material Interaction in Fast Diffusion Materials-A Feasibility Study on a Complex Phase Steel, *Materials (Basel, Switzerland)* 13 (2020).
- [35] A. Massone, A. Manhard, W. Jacob, A. Drexler, W. Ecker, A. Hohenwarter, S. Wurster, D. Kiener, An SEM compatible plasma cell for in situ studies of hydrogen-material interaction, *Review of Scientific Instruments* 91 (2020) 43705.

- [36] J. Kim, C.C. Tasan, Microstructural and micro-mechanical characterization during hydrogen charging: An in situ scanning electron microscopy study, *Int. J. Hydrogen Energy* 44 (2019) 6333–6343.
- [37] American Petroleum Institute, *Age-hardened Nickel-based Alloys for Oil and Gas Drilling and Production Equipment*, 1st ed.(API STD 6ACRA), 2018.
- [38] G. Stenerud, R. Johnsen, J.S. Olsen, J. He, A. Barnoush, Effect of hydrogen on dislocation nucleation in alloy 718, *Int. J. Hydrogen Energy* 42 (2017) 15933–15942.
- [39] K. Durst, V. Maier, Dynamic nanoindentation testing for studying thermally activated processes from single to nanocrystalline metals, *Current Opinion in Solid State and Materials Science* 19 (2015) 340–353.
- [40] A.G. Atkins, D. Tabor, Plastic indentation in metals with cones, *Journal of the Mechanics and Physics of Solids* 13 (1965) 149–164.
- [41] H. Vehoff, D. Lemaire, K. Schüler, T. Waschkes, B. Yang, The effect of grain size on strain rate sensitivity and activation volume – from nano to ufg nickel, *IJMR* 98 (2007) 259–268.
- [42] B.R. Lawn, A.G. Evans, D.B. Marshall, Elastic/Plastic Indentation Damage in Ceramics: The Median/Radial Crack System, *J American Ceramic Society* 63 (1980) 574–581.
- [43] Y. Ogawa, D. Birenis, H. Matsunaga, A. Thøgersen, Ø. Prytz, O. Takakuwa, J. Yamabe, Multi-scale observation of hydrogen-induced, localized plastic deformation in fatigue-crack propagation in a pure iron, *Scripta Mater.* 140 (2017) 13–17.
- [44] D. Catoor, Y.F. Gao, J. Geng, M. Prasad, E.G. Herbert, K.S. Kumar, G.M. Pharr, E.P. George, Incipient plasticity and deformation mechanisms in single-crystal Mg during spherical nanoindentation, *Acta Mater.* 61 (2013) 2953–2965.
- [45] T. Ohmura, M. Wakeda, Pop-In Phenomenon as a Fundamental Plasticity Probed by Nanoindentation Technique, *Materials (Basel, Switzerland)* 14 (2021) 1879.
- [46] C. Zhu, Z.P. Lu, T.G. Nieh, Incipient plasticity and dislocation nucleation of FeCoCrNiMn high-entropy alloy, *Acta Mater.* 61 (2013) 2993–3001.
- [47] D. Wang, X. Lu, M. Lin, Di Wan, Z. Li, J. He, R. Johnsen, Understanding the hydrogen effect on pop-in behavior of an equiatomic high-entropy alloy during in-situ nanoindentation, *Journal of Materials Science & Technology* 98 (2022) 118–122.
- [48] G. Yang, Y. Zhao, D.-H. Lee, J.-M. Park, M.-Y. Seok, J.-Y. Suh, U. Ramamurty, J. Jang, Influence of hydrogen on incipient plasticity in CoCrFeMnNi high-entropy alloy, *Scripta Materialia* 161 (2019) 23–27.
- [49] D.H. Lee, J.A. Lee, M.Y. Seok, U.B. Baek, S.H. Nahm, J.I. Jang, Stress-dependent hardening-to-softening transition of hydrogen effects in nanoindentation of a linepipe steel, *Int. J. Hydrogen Energy* 39 (2014) 1897–1902.
- [50] Y. Zhao, J.-M. Park, D.-H. Lee, E.J. Song, J.-Y. Suh, U. Ramamurty, J. Jang, Influences of hydrogen charging method on the hydrogen distribution and nanomechanical properties of face-centered cubic high-entropy alloy: A comparative study, *Scripta Materialia* 168 (2019) 76–80.

- [51] A. Barnoush, M. Asgari, R. Johnsen, Resolving the hydrogen effect on dislocation nucleation and mobility by electrochemical nanoindentation, *Scripta Mater.* 66 (2012) 414–417.
- [52] K.A. Nibur, D.F. Bahr, B.P. Somerday, Hydrogen effects on dislocation activity in austenitic stainless steel, *Acta Mater.* 54 (2006) 2677–2684.
- [53] Y. Tang, S.I. Rao, J.A. El-Awady, in: TMS (Ed.), TMS 2013 142nd annual meeting & exhibition: Annual meeting supplemental proceedings, TMS, Hoboken, N.J, s.l., 2013, pp. 719–726.
- [54] K.R. Morasch, The effects of hydrogen on deformation and cross slip in a BCC titanium alloy, *Scripta Materialia* 45 (2001) 839–845.
- [55] Y. Zhao, X. Wang, T. Cao, J.-K. Han, M. Kawasaki, J. Jang, H.N. Han, U. Ramamurty, L. Wang, Y. Xue, Effect of grain size on the strain rate sensitivity of CoCrFeNi high-entropy alloy, *Materials Science and Engineering A* 782 (2020) 139281.
- [56] F. Dalla Torre, H. van Swygenhoven, M. Victoria, Nanocrystalline electrodeposited Ni: microstructure and tensile properties, *Acta Mater.* 50 (2002) 3957–3970.
- [57] J. Wehrs, G. Mohanty, G. Guillonneau, A.A. Taylor, X. Maeder, D. Frey, L. Philippe, S. Mischler, J.M. Wheeler, J. Michler, Comparison of In Situ Micromechanical Strain-Rate Sensitivity Measurement Techniques, *JOM* 67 (2015) 1684–1693.
- [58] K. Gopinath, A.K. Gogia, S.V. Kamat, R. Balamuralikrishnan, U. Ramamurty, Tensile Properties of Ni-Based Superalloy 720Li: Temperature and Strain Rate Effects, *Metall Mater Trans A* 39 (2008) 2340–2350.
- [59] V. Maier-Kiener, B. Schuh, E.P. George, H. Clemens, A. Hohenwarter, Nanoindentation testing as a powerful screening tool for assessing phase stability of nanocrystalline high-entropy alloys, *Materials & Design* 115 (2017) 479–485.
- [60] M.A. Meyers, A. Mishra, D.J. Benson, Mechanical properties of nanocrystalline materials, *Progress in Materials Science* 51 (2006) 427–556.
- [61] Q. Wei, S. Cheng, K. Ramesh, E. Ma, Effect of nanocrystalline and ultrafine grain sizes on the strain rate sensitivity and activation volume: fcc versus bcc metals, *Materials Science and Engineering A* 381 (2004) 71–79.
- [62] Z. Wu, Y. Gao, H. Bei, Thermal activation mechanisms and Labusch-type strengthening analysis for a family of high-entropy and equiatomic solid-solution alloys, *Acta Mater.* 120 (2016) 108–119.
- [63] S.I. Hong, J. Moon, S.K. Hong, H.S. Kim, Thermally activated deformation and the rate controlling mechanism in CoCrFeMnNi high entropy alloy, *Materials Science and Engineering A* 682 (2017) 569–576.
- [64] W. Xia, G. Dehm, S. Brinckmann, Insight into indentation-induced plastic flow in austenitic stainless steel, *J Mater Sci* 55 (2020) 9095–9108.
- [65] K.A. Nibur, D.F. Bahr, Identifying slip systems around indentations in FCC metals, *Scripta Materialia* 49 (2003) 1055–1060.

- [66] J. Song, W.A. Curtin, Mechanisms of hydrogen-enhanced localized plasticity, *Acta Mater.* 68 (2014) 61–69.
- [67] X. Lu, D. Wang, Effect of hydrogen on deformation behavior of Alloy 725 revealed by in-situ bi-crystalline micropillar compression test, *Journal of Materials Science & Technology* 67 (2021) 243–253.
- [68] Di Wan, Y. Deng, J.I.H. Meling, A. Alvaro, A. Barnoush, Hydrogen-enhanced fatigue crack growth in a single-edge notched tensile specimen under in-situ hydrogen charging inside an environmental scanning electron microscope, *Acta Mater.* 170 (2019) 87–99.
- [69] M. Wasim, M.B. Djukic, Hydrogen embrittlement of low carbon structural steel at macro-, micro- and nano-levels, *Int. J. Hydrogen Energy* 45 (2020) 2145–2156.

Publication C

**Grain boundary segregation in Ni-base alloys:
A combined atom probe tomography and first principles study**

**Anna Sophie Ebner , Severin Jakob, Helmut Clemens,
Reinhard Pippan, Verena Maier-Kiener, Shuang He, Werner Ecker,
Daniel Scheiber, Vsevolod I. Razumovskiy**

Acta Materialia, 221 (2021) 117354

**Grain boundary segregation in Ni-base alloys:
A combined atom probe tomography and first principles study**

Anna Sophie Ebner^a, Severin Jakob^a, Helmut Clemens^a,
Reinhard Pippan^b, Verena Maier-Kiener^a, Shuang He^c, Werner Ecker^c,
Daniel Scheiber^c, Vsevolod I. Razumovskiy^c

^a Department of Materials Science, Montanuniversität Leoben, Leoben 8700, Austria

^b Erich Schmid Institute for Materials Science, Austrian Academy of Sciences, Leoben 8700 Austria

^c Materials Center Leoben Forschung GmbH, Leoben 8700, Austria

Keywords: Grain boundary segregation; First principles calculations; Atom probe tomography; Interfacial excess evaluation; Grain boundary engineering

Abstract

Grain boundary engineering (GBE) plays an important role in the design of new polycrystalline materials with enhanced mechanical properties. This approach has been shown to be very effective in design of Ni-base alloys, where grain boundary segregation is expected to play a central role in defining their mechanical behavior. In the present work, we apply a powerful combination of advanced experimental and theoretical methods to reveal the grain boundary chemistry of the 725 Ni-base alloy at the atomic level. The methods of investigation comprise atom probe tomography (APT) measurements and density functional theory (DFT) calculations. We also propose a way to cross-validate DFT and APT results in a DFT-based model approach for evaluation of the interfacial excess as a function of the heat treatment history of the material and its chemistry. Both theoretical and experimental methods are applied to a detailed analysis of the GB chemistry of three modifications of the 725 alloy and the results of this investigation are presented and discussed in detail.

1. Introduction

The main idea behind the segregation-based grain boundary engineering (GBE) concept focuses on tailoring material properties by controlling the grain boundary (GB) chemistry by means of alloying or applying specific heat treatments to achieve a desired GB composition [1,2]. The ability to control the GB chemistry requires access to accurate and predictive material models that need to be experimentally validated. In spite of a quite substantial effort in this direction on both experimental and theoretical sides of the problem, there are only a few publications addressing the direct comparison between experimental and theoretical data on segregation at the atomic level [3–9]. The main reason is that experimental methods of GB chemistry investigation, like atom probe tomography (APT), and predictive computational approaches, like density functional theory (DFT), work at different time and length scales. Both methods have their own limitations and, as a consequence, require an adequate and robust methodological approach to compare and validate the results.

The approach we propose to address this problem is based on the use of the McLean segregation isotherm [10] and its site competition as well as its kinetic extensions [7,11]. In this way the segregation energies accessible in DFT calculations and the actual bulk content from the experiment are connected to the measured GB enrichment of solutes after a certain heat treatment.

The Rice-Wang theory of GB embrittlement [12] and some of its parameters like the changes in work of separation are directly accessible in DFT calculations [13–16] and can be immediately utilized in this approach as indicators of a possible effect of solutes on the GB cohesive strength: solutes that prefer segregation to the GB over the free surface lead to an increase in GB cohesion upon segregation, whereas solutes decreasing the GB cohesion prefer segregation to the free surface.

Some of the methods discussed above are available for some decades but their application for evaluation and interpretation of experimental results has been scarcely reported so far and mostly focused on understanding GB segregation at a qualitative level and neglecting experimental validation in many cases [11,17–22].

Therefore, APT could provide an excellent method for complementing this modelling-based approach. Research on Ni-base alloys with APT is a common tool to address different GB chemistry related issues [23–25]. With the interfacial excess (IFE) first mentioned by Thuvander et al. and Hellmann et al. [26,27], GB segregation is accessible in a quantitative way. While keeping in mind some critical reflections [28], the interfacial excess analysis can be used to explain segregation phenomena in different material classes [29–31]. Such developments of theoretical and experimental state-of-the-art techniques have already brought the field of GBE to a new level of quantitative investigations for the GB segregation phenomenon.

In this paper, we employ state-of-the-art APT for quantitative measurements of the IFE values of alloying elements in a 725 Ni-base alloy and use predictive DFT-based model IFE calculations to interpret and explain the experimental data. The proposed model approach is extended beyond standard single solute enrichment models to describe simultaneous multiple solute segregation to the GB. The experimental measurements are performed on multiple tips for three different alloy modifications to justify the validity of the proposed approach.

2. Methodology

2.1. Material and metallographic preparation

The three studied Ni-base alloys were trial melts where the first alloy (ModA) has the nominal composition of Alloy 725 with its main alloying elements Cr, Fe, Mo, Ti and Nb [32]. The other two alloys were slightly modified with B addition for ModB and Cu and B additions for ModC. The alloys were melted in a vacuum induction furnace and forged into cylindrical bars with a diameter of 130 mm. For homogeneous distribution of all alloying elements, solution annealing was done at 1040 °C for 2 h with a following water quenching. The aging itself was conducted at 740 °C and 620 °C for 8 h respectively, with furnace cooling in between and subsequent water quenching. This heat treatment resulted in an average grain size of $138.9 \pm 9.0 \mu\text{m}$ for ModA, $132.8 \pm 6.6 \mu\text{m}$ for ModB and 163.6 ± 4.6 for ModC and the presence of γ'' strengthening phases [33] for all three alloys. Cylindrical samples with a diameter of 12 mm were produced via wire erosion from the forged ingot and cut into 3 mm slices for further metallographic sample preparation. The surface was ground with SiC paper from grid 320 to 1200. Mechanical polishing

was done with 3 and 1 μm diamond suspension and finalized with colloidal silica suspension (Struers OP-S) for a better visibility of the GB structure.

2.2. Sample preparation for atom probe tomography

The atom probe tip preparation for the GBs was performed in a FEI Versa 3D Dualbeam workstation, attached with a EDAX Hikari XP system for electron backscatter diffraction (EBSD) analysis. The most frequently observed GBs with similar misorientation between 38° and 48° and grain orientations near to $[1\ 1\ 1]$ and $[1\ 0\ 1]$ were selected via EBSD technique, and are exemplarily depicted in Fig. 1 (b). Note that this is not equivalent to a complete characterization of all five degrees of freedom, which is much more involved and beyond the scope of this work. For specimen preparation the lift-out technique according to the work of Babinsky et al. [29,34] was used. This technique was first mentioned by Miller et al. [35,36]. For a successful positioning of the GB in the vicinity of the apex of the tip, this technique combines focused ion beam (FIB) milling with transmission Kikuchi diffraction (TKD). EBSD analysis was performed in analytical mode with acceleration voltage of 20 kV and a probe current of 8 nA. All coarse milling steps were performed with 30 kV and ion currents between 100 pA and 3 nA. Subsequent annular fine milling was carried out with 8 kV and 12 pA. The preparation sequence of a representative GB is shown in Fig. 1. For further details on the applied TKD technique see Ref. [37]. With this technique it was possible to fabricate several tips for each modification suitable for APT measurement and further segregation analysis.

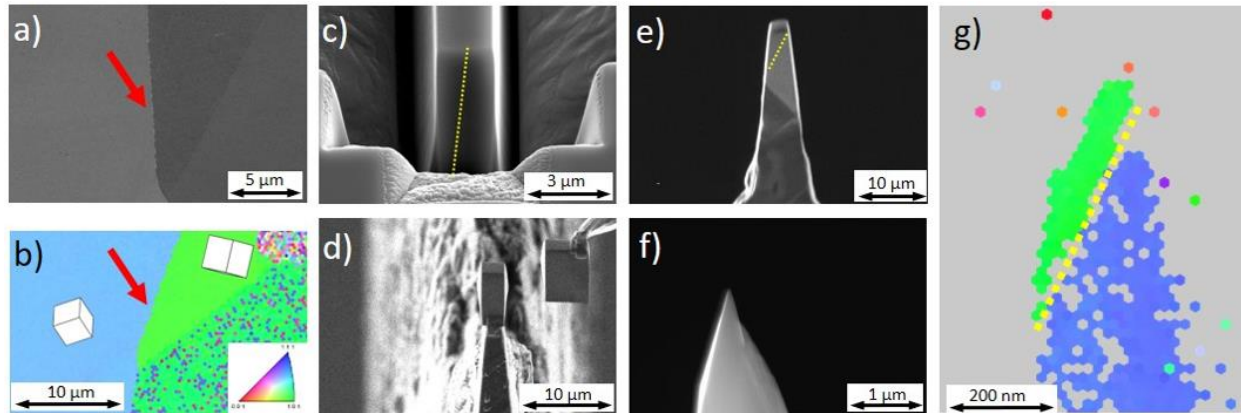


Fig. 1 Sequence of the APT tip preparation with FIB milling and combined TKD method: a) selected GB of Mo₄A in secondary electron contrast and b) as EBSD inverse pole figure map with corresponding unit cells; c) material wedge with the GB (yellow, dotted line) before lift-out and d) during positioning on a Mo carrier grid; e) representative sample after positioning and pyramidal milling; f) the finished APT needle after annular milling; g) respective TKD map of final tip, the GB is located within the first 100 nm

2.3. Atom probe tomography and data

The used APT system was a Cameca LEAP 30 0 0X HR in laser-pulse mode with a laser energy of 0.5 nJ (laser wavelength 525 nm, spot size $\sim 10 \mu\text{m}$). The temperature was set to 60 K and the used pulse frequency was 250 kHz. The target evaporation rate was varied between 0.5% and 1%. For reconstruction, the software IVAS 3.6.14 (Cameca) was employed.

For quantifying the GB segregation, the Gibbs IFE value was calculated, which describes the excess number of atoms per unit area (atoms/nm^2) resulting from solute segregation to the interface. For this method, a cylindrical region of interest (ROI), positioned perpendicular to the GB plane (see Fig. 2 (a), left), was used to prepare so-called ladder diagrams as described in Refs. [27,26].

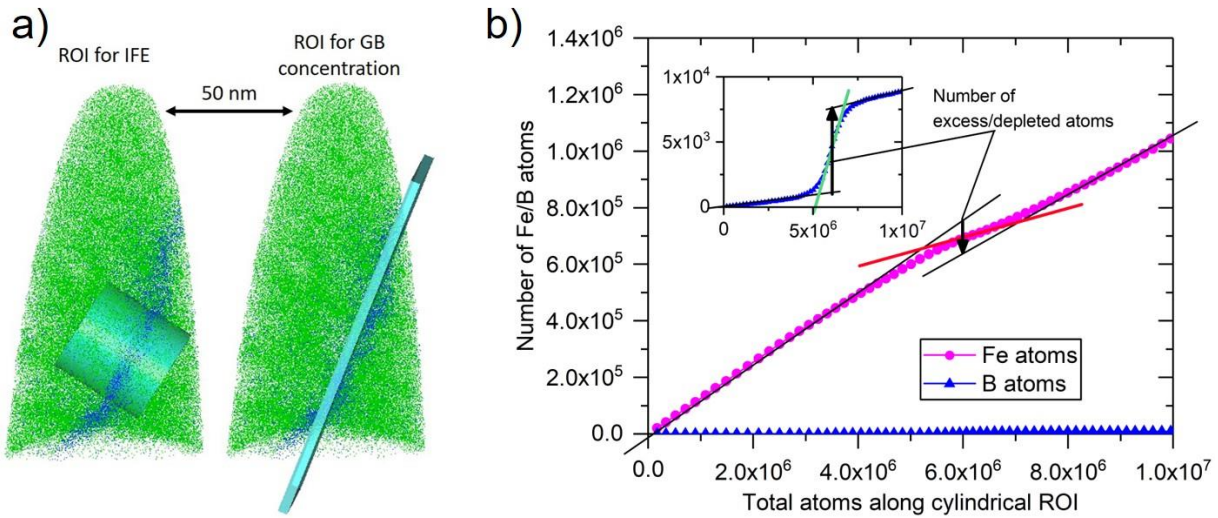


Fig. 2 a) ROI for the evaluation of the IFE value (left) and the GB concentration (right); b) exemplary ladder diagram for Fe and B at a ROI perpendicular to the GB (in Moda). The linear fit shows segregation (green) and depletion (red), the excess or depletion atoms are indicated with black arrows.

This method is insensitive to reconstruction artifacts and resolution issues [38], which might be observed in concentration profiles. These values can be compared quantitatively for each element in the different modifications. For better understanding of the origin of IFE values, a ladder diagram for Fe and B is schematically visualized in Fig. 2 (b). Fe shows depletion at the GB represented by the slightly decreasing slope (red), which leads to a negative IFE value. In contrast, B exhibits a strong segregation to the GB outlined by the pronounced increase in the slope (green), which results in a positive IFE.

The chemical composition of the APT tips was evaluated in two different regions defined by a cuboidal ROI of 5 nm thickness through the GB plane, which is depicted in Fig. 2 (a)(right). The first region is outside this ROI and was used for the matrix composition, whereas the second region is inside this ROI and was used for the GB composition, respectively.

For analyzing the composition of occurring γ'' precipitates, a proximity histogram (proxigram) [39] was created for Nb isoconcentration surfaces with a threshold of 5 at% (the corresponding isosurfaces can be seen in Fig. 4 (d)). To exclude the influence of the segregated elements at the GB, the proxigram, was calculated for the matrix region only with a bin size of

0.1 nm and a maximum distance of 5 nm, where edge polygons were excluded from the computation.

2.3. DFT calculations

The first principles calculations at 0 K were performed using the projector-augmented wave (PAW) [40,41] method as employed in the Vienna *ab initio* simulation package (VASP) [42,43]. The Perdew-Burke-Ernzerhof (PBE) implementation of generalized gradient approximation (GGA) was used for the exchange-correlation potential [44]. The plane-wave basis set cutoff energy was set to 400 eV. The convergence criteria of self-consistent calculations was set to 10^{-5} eV/cell for the total energy and to 9×10^{-3} eV/Å for the atomic forces. The integration over the Brillouin zone was done using the $4 \times 4 \times 1$ Monkhorst-Pack k -mesh [45] for the GB cell and using the $4 \times 4 \times 4$ k -mesh in the $3 \times 3 \times 3$ (conventional face-centered cubic (fcc) cell) bulk supercell calculations. The lattice parameter was fixed to 3.515 Å [46] and only the ions were allowed to relax in the calculations. The coincidence site lattice (CSL) symmetric tilt $\Sigma 5(012)[100]$ has been selected as a representative GB in this study [17]. This high angle GB has a GB energy that falls in the mid-range of the CSL GB energies and is close to the experimentally measured GB energy values in polycrystalline Ni [46]. The $\Sigma 5(012)$ GB was modeled using a 76-atom GB slab with 19 layers and 4 atoms/layer [46]. The Ni $\Sigma 5(012)$ GB structure used in this work is illustrated in Fig. 3 (a).

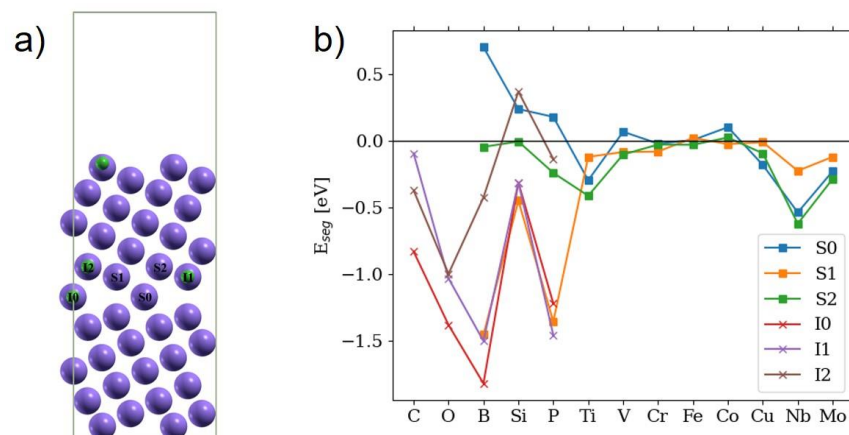


Fig. 3: a) Structure of the employed $\Sigma 5(012)[100]$ CSL GB where both substitutional (S0 to S2) and interstitial (I0 to I2) sites at the GB are labelled; b) segregation energies for studied solutes to interstitial and substitutional positions.

The site preference of impurities in the bulk of fcc Ni was studied by means of DFT calculations, which showed that C, B, and O occupy the octahedral interstitial site in the bulk. We have computed the GB segregation energy as the total energy difference between the bulk of the material with an impurity atom occupying the most-stable site (i.e. interstitial octahedral or substitutional site) and the system with an impurity atom situated at the GB (both substitutional and interstitial sites are considered). The segregation energy is given by [17,46]

$$E_{seg} = (E_{slab}^j - E_{slab}) - (E_{bulk}^j - E_{bulk}) + \delta E_{bulk}/N, \quad (1)$$

where E_{slab}^j and E_{slab} denote the total energy of the GB slab with and without solute j , respectively, and similar, E_{bulk}^j and E_{bulk} refer to the bulk cell with and without solute j . The number of atoms in the pure bulk cell is denoted by N and δ changes depending on the site type. For the case where a solute segregates from the one type of site (interstitial or substitutional) in the bulk to same type of site at the GB, $\delta = 0$, for the case that the solute is interstitial in the bulk and substitutional at the GB, $\delta = 1$, and in case the solute is substitutional in the bulk and interstitial at the GB, $\delta = -1$. In this definition, solute enrichment is preferential for negative values of the segregation energy and solute depletion for positive values.

The GB enrichment of the impurities was modeled using a modified McLean isotherm [7,10,47] that incorporates multiple solutes and multiple sites at the GB, which allows to use as input GB segregation energy profiles from DFT calculations. With that the concentration at the GB for a solute j is computed as

$$C_{GB}^j = \frac{1}{n} \sum_i \frac{C_b^j \exp(-\beta E_{seg}^{i,j})}{1 - \sum_l C_b^l + C_b^l \exp(-\beta E_{seg}^{i,l})}. \quad (2)$$

Here, n is the number of sites at the GB, C_b^j the bulk content of solute j , $E_{seg}^{i,j}$ the segregation energy of solute j to site i at the GB, and β is given by $1/(k_B T)$. The IFE value in atoms/nm² that is extracted from APT measurements can be computed from the GB concentration as [2]

$$IFE = n(C_{GB} - C_b)/A, \quad (3)$$

with A denoting the area of the GB.

3. Results

3.1. General APT results

For ModA, only a single tip was used for IFE calculation, because the conducted APT measurements revealed a GB decoration with an intermetallic phase on all but one tip. The measured phase may be a F-phase [48], but the nature of it is not in the scope of this work and pronounced GB phases would affect the IFE segregation analysis. Therefore, only the single tip without the intermetallic GB phases was analyzed and all IFE values for ModA therefore have no error bars. For ModB and ModC, two and four tips, respectively, were successfully measured and the error bars give the minimum and maximum of the corresponding values in Fig. 6.

The overall visual appearance of the element distribution in the single APT tips is similar for all three modifications. Thus, in Fig. 4 the individual elements of an exemplary tip of ModB are shown. The corresponding figures for ModA and ModC can be found in the supplementary. In contrast to the visual appearance, a clear distinction between the modifications can be made by comparison of the chemical composition obtained from the APT analysis as summarized in Table 1. As expected, the main differences between the three alloys are visible in B and Cu content.

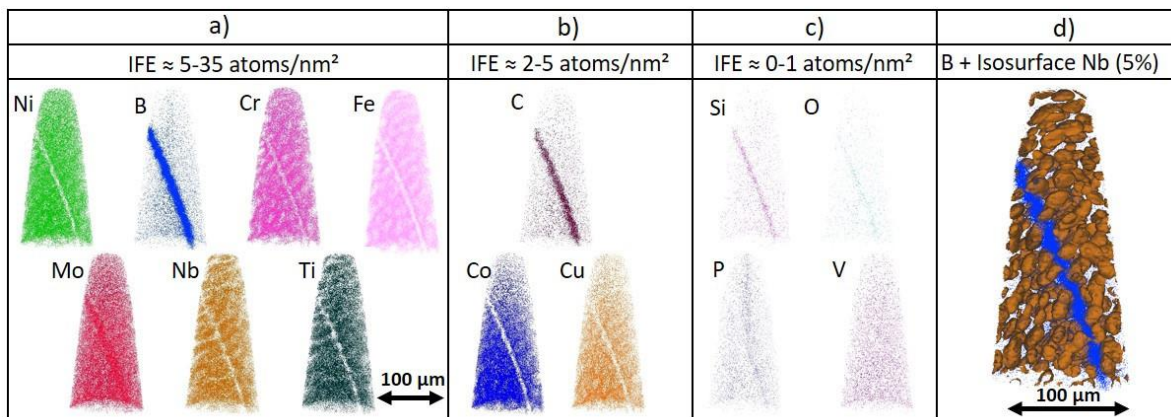


Fig. 4: APT reconstruction of a measured tip of ModB: a) elements with IFE value between ± 5 to 35 atoms/nm²; b) elements with IFE value between ± 2 to 5 atoms/nm²; c) elements with IFE value below ± 1 atoms/nm²; d) shows isoconcentration surfaces with a threshold of 5 at% for Nb (orange) and B atoms (blue).

All three modifications show the presence of γ'' precipitates (see Fig. 4 (d) and supplementary), which exhibit a higher Nb and Ti concentration according to literature and a stoichiometry of $\text{Ni}_3(\text{Nb}, \text{Ti}, \text{Al})$ [49–52]. For further analysis of the chemical nature of the precipitates, proxigrams were studied for the isosurfaces with a Nb concentration of 5 at% and are depicted in Fig. 5. The increase in scatter at a distance of above 3 nm arises due to the varying precipitate size, which can be smaller than the 5 nm chosen as maximum distance. Due to minor differences in the results of the proxigrams of the different modifications, an exemplary one is shown for ModB. The proxigrams for ModA and ModC can be found in the supplementary. The main elements enriched in the γ'' are Ni, Nb and Ti. A lower solubility of Fe and Cr is present, as visible in Fig. 5 (a). In Fig. 5 (b), a slight enrichment of Mo at the interface between matrix and γ'' appears. In comparison, Co and Cu show an even distribution throughout the precipitate. The alloying elements B, C, Al, and Si all show a slight increase in concentration inside the γ'' precipitate (see Fig. 5 (c)).

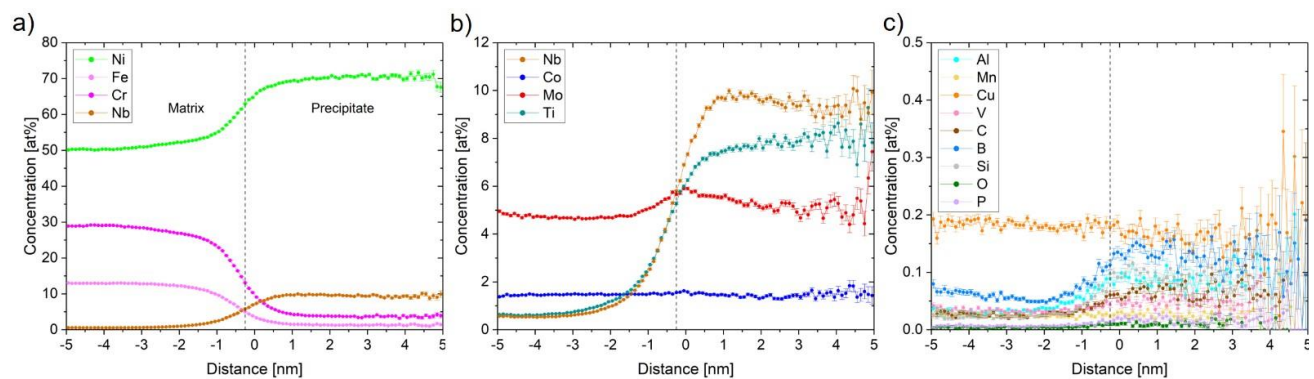


Fig. 5: Exemplary proxigrams for precipitates in ModB with 5 at% Nb for the elements with a) alloying content up to 50 at%, b) alloying content from 1 to 10 at%, and c) low alloying content between 0 and 0.5 at%. (GB region of 10 nm thickness was excluded for evaluation).

Table 1: Average chemical composition from APT analysis for the grain interior (Matrix) and the GB region (GB) in at%. For the definition of GB and matrix region see section 2.3 and Fig. 2 (a).

	ModA		ModB		ModC	
	Matrix	GB	Matrix	GB	Matrix	GB
Ni	57.87%	59.77%	55.97%	48.66%	54.77%	46.48%
Cr	22.50%	18.29%	24.54%	26.38%	24.73%	26.58%
Fe	11.43%	7.92%	10.82%	9.44%	9.06%	8.04%
Mo	3.26%	4.83%	3.55%	7.99%	3.94%	9.03%
Nb	2.17%	4.38%	2.01%	1.87%	1.97%	1.69%
Ti	2.09%	3.87%	1.87%	1.48%	1.86%	1.35%
B	0.03%	0.28%	0.11%	2.91%	0.13%	3.36%
C	0.02%	0.10%	0.02%	0.45%	0.03%	0.42%
P	0.00%	0.02%	0.00%	0.09%	0.00%	0.09%
Cu	0.05%	0.05%	0.08%	0.06%	1.91%	1.33%
Co	0.44%	0.28%	0.93%	0.51%	1.14%	0.69%
Mn	0.01%	0.01%	0.01%	0.02%	0.02%	0.03%
Al	0.08%	0.10%	0.05%	0.05%	0.06%	0.05%
V	0.01%	0.01%	0.01%	0.01%	0.02%	0.02%
Si	0.04%	0.10%	0.02%	0.05%	0.02%	0.05%
O	0.00%	0.00%	0.00%	0.03%	0.03%	0.07%

3.2. IFE determination from APT data

Fig. 6 shows a bar chart for the GB enrichment in all three modifications, where Fig. 6 (a) contains all elements with strong tendency for segregation or depletion, denoted by an absolute IFE value between 5 and 35 atoms/nm². Fig. 6 (b) and (c) correspond to medium (1–5 atoms/nm²) and low (0–1 atoms/nm²) segregation/depletion tendencies, respectively. For strongly segregating elements, ModB and ModC show similar behavior, whereas ModA exhibit distinctly lower IFEs for B and Ni. The amount of Mo segregation is in the same range for all three modifications. In contrast to ModB and ModC, the IFE for Cr and Fe in ModA is negative, while for Nb and Ti, the opposite is the case. Co and C show the same tendencies of medium

segregation/depletion in all three alloys. Obvious variations can be seen in Cu for ModC, which are understandable in terms of the added Cu for ModC. All comparisons for elements with low IFE value must be treated with caution, since values between 0 and 1 are suggesting quite low propensity for segregation. However, the observed trends in Fig. 6 (c) are consistent for the three studied alloys.

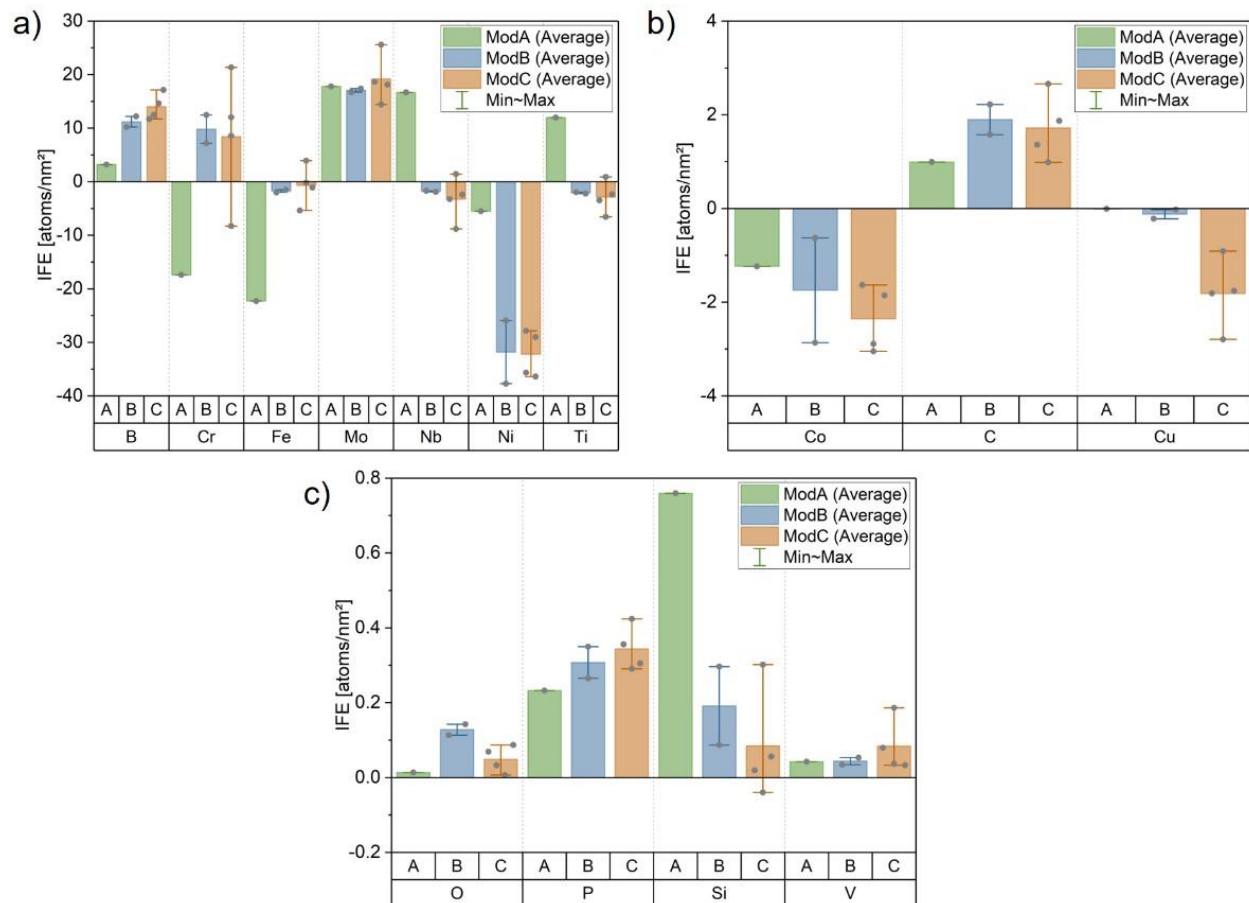


Fig. 6: Average IFE values for all elements and modifications with (a) high IFE values, (b) medium IFE values and (c) low IFE values. The error bars represent minimum and maximum value (see text).

3.3. Segregation energies from DFT

The segregation energies of key alloying elements are evaluated using ab-initio calculations of solutes at the $\Sigma 5(012)[100]$ GB of Ni. We have computed the segregation energies for the investigated solutes from their preferred bulk position to both interstitial and substitutional site at the GB. The obtained segregation energies are presented in Fig. 3 (b). Stable interstitial sites at the GB with values for the segregation energy below zero (indicating

segregation propensity) were found only for C, O, B, Si, and P. Overall, the strongest segregation tendency is observed for B and P, followed by O and C with segregation energies down to -1.5 eV. The transition metals and Si have significantly lower segregation tendencies with values above -0.6 eV. Especially for V, Cr, Fe, and Co, the segregation energies are close to zero and therefore, segregation is unlikely for these solutes.

4. Discussion

4.1. APT and IFE analysis

A first evidence for segregation to the GB can be gained by comparing the average chemical composition between matrix and the GB region of the three modifications listed in Table 1 and the visual appearance of the tips in Fig. 4. As example, for ModB the elements B, Mo, C, Si and P appear to accumulate at the GB in the visual APT reconstruction. This correlates well with the average chemical composition. For some other elements, e.g. Cr, this correlation is not as clear. Here, the analysis of IFE values and proxigrams can give a deeper insight into the occurring segregation.

When analyzing the segregation tendencies, occurring precipitates have to be considered, as all types of precipitates can have undesirable influence on the IFE evaluation. Due to the higher Nb and Ti concentration inside the γ'' precipitates, which can be seen in the proxigrams in Fig. 5 for our alloy 725, both elements are strongly depleted in the matrix region and are not available for segregation to the GB. Thus, they are excluded in some points of discussion later on. This partitioning was also shown by Gardner et al. [49] for γ'' precipitates in Inconel 625. Furthermore, the suppression of Fe and Cr also has to be kept in mind for the discussion of IFE data. The segregation of Mo to the interface between matrix and γ'' precipitates is small (increase of ~ 1 at%, seen in 5 (b)) in comparison to the segregation to the GB (increase of ~ 4.5 at%, shown in Table 1) and therefore, it may be neglected as it will have no influence on the IFE analysis.

The quantitative magnitude of the IFE is not solely defined by the amount of segregation because it also depends on the bulk concentration. Therefore, comparison of IFE is ideal for elements with similar bulk concentration. Nevertheless, it is possible to explain some deviations of IFE in the different modifications by taking a closer look into the elements' distribution in Fig. 4. It is visible, that some elements, in particular Cr, Fe, Nb, and Ti, show an inhomogeneous

distribution in the grain interior apart. By applying the isoconcentration surfaces for Nb and Ti with a threshold of 5%, it is possible to reveal the γ'' precipitates. These precipitates also have further reaching impact on other elements. For example, Cr and Fe are expelled from the γ'' precipitate because of their lower solubility, which results in an inhomogeneous distribution throughout the remaining tip [53] visible in Fig. 4 (a). This can compromise the IFE evaluation at the GB. The non-uniform element distribution leads to some additional considerations when interpreting IFE results. For compensation of composition differences, the volume of the chosen cylindrical region of interest should be maximized by setting the diameter as big as possible inside each individual APT tip. This way, the composition is averaged over precipitates and matrix to obtain a meaningful concentration profile, which minimizes the influence on the IFE calculation. Special caution should still be taken for interpreting the IFE of these elements, as it might explain part of the differences between ModA in comparison to ModB and ModC for the elements Cr, Fe, Nb, and Ti.

A second possible reason for the deviations is the presence of unwanted an intermetallic phase in the vicinity of the analyzed tip in ModA, yet outside the APT needle. The F-phase has a higher content of Cr and Fe [48], and hence can lead to the strong depletion of these two elements in the tip of ModA used for IFE calculation, see Fig. 6 (a). This depletion can also have a further influence on the IFE of Ni in ModA. Since Fe and Cr are already strongly depleted, the lack of Ni at the GB is not as pronounced.

4.2. Segregation modeling

The segregation energy profiles shown in Fig. 3 (b) along with the bulk composition from the APT measurements from Table 1 have been used as an input for the modified multi-site and multi-component McLean Isotherm (see Eq. 2 and Ref. [11]). Due to the presence of coherent γ'' precipitates throughout the analyzed sample, Nb, Ti and Al atoms have been excluded from the analysis as discussed in Section 4.1 .

The calculated results on the GB enrichment shown in Fig. 7 suggest that B, Mo, and O are the strongest segregation solutes in the fcc solid solution of Ni. The strongest and practically temperature-independent enrichment in the considered temperature range is observed for B. This strong segregation tendency is a result of exceptionally low segregation energy values for B

at multiple GB segregation sites in Ni shown in Fig. 3 (b). A similar segregation energy profile has been obtained for P (Fig. 3 (b)), but its GB concentration appears to be insignificant compared to that of B due to an order of magnitude smaller bulk content of P in the Ni solid solution and a strong site competition with B atoms. In other words, P and B can segregate to the same sites but the element with the strongest segregation tendency (B) can replace the other one (P). This is exactly what we see in the calculations for the case of B and P site competition: B atoms dominate GB segregation and replace P. The situation is somewhat different for O, which also segregates to the same GB sites as B but has a stronger segregation tendency to site I2 and therefore has a rather pronounced GB excess in the calculations.

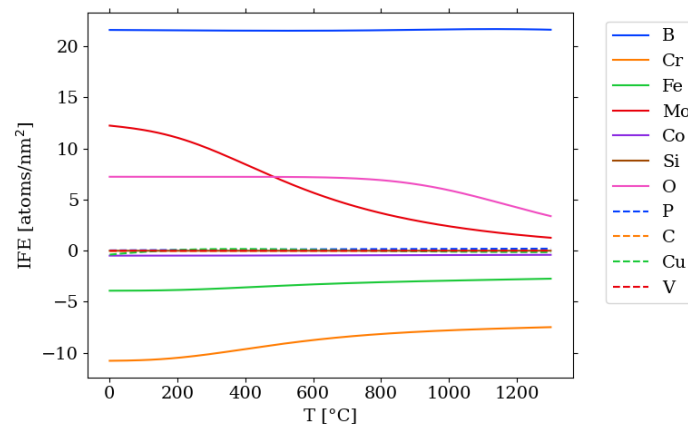


Fig. 7: Estimate of the GB enrichment as a function of temperature evaluated with multi-site McLean isotherm exemplarily for alloy ModC. No significant enrichment is observed for the elements Co, Si, P, C, and V.

Compared to the solutes discussed above, Mo atoms segregate exclusively to the GB substitutional sites and win the substitutional site competition (see Fig. 3 (b)). Therefore, Mo atoms show a substantial GB enrichment in the calculations that increases as the temperature decreases. This trend is different to other substitutional solutes such as Cr, Fe, and Cu, whose content decreases with decreasing temperature as they get replaced by Mo and other stronger segregating atoms like V at lower temperatures. However, the calculated IFE within the modified McLean model GB excess of Co, Si, P, C, and V is negligibly small at all temperatures due to very low segregation energy values at all considered GB sites.

4.3. APT vs DFT

In the previous sections, GB segregation was investigated with experimental and computational methods, which can now be combined and compared to evaluate and discuss the differences between both approaches. For comparing the measured content with the modelled results, we evaluate the IFE from DFT at the last annealing step at 620°C. No further solute enrichment takes place in a consequent cooling step, which has been checked for different technically relevant cooling rates by explicit kinetic segregation calculations, see Refs. [11,47] for the model description. In Fig. 8, the IFE from APT is plotted against the IFE from the DFT approach evaluated at the last annealing step at 620 °C. The error bars for experimental data correspond to the variation in IFE measurements. Since for ModA only one GB without *F*-phase was measured, there are no vertical error bars indicated. For the simulation of IFE value, the chemical composition from APT measurements was used as input, see Table 1. To visualize the variations in IFE, that originate from fluctuations in the bulk, the IFE computed from the segregation energies is obtained with bulk content values from Table 1 that are varied by a factor of 0.5 to 1.5. This variation is shown as horizontal error bars in Fig. 8.

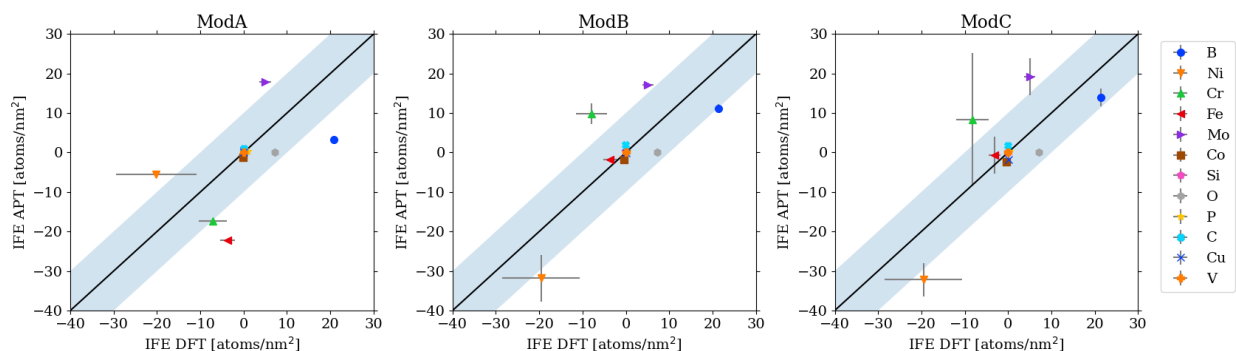


Fig. 8: Correlation of IFE values from APT and DFT for investigated alloys. The variation of APT measurements in the IFE values is shown with vertical error bars and the effect of bulk variations on modelling the IFE is shown as horizontal error bars. The blue shaded region marks ± 10 atoms/nm². See text for further details.

There is a linear correlation observable between the measurements and computed IFE values. The agreement between the two sets of data is quantitatively convincing and perfect on a qualitative level, when considering the error bars that highlight the possible variations. For all

alloy modifications, most elements are within the blue shaded region of ± 10 atoms/nm². Elements above the median correspond to higher experimental segregation than predicted from simulation. The data points below the median vice versa corresponds to lower experimental segregation. For example, Mo is slightly underestimated for all modifications while for modification ModA, Fe, Cr, and B are overestimated in the computed values. This overestimation in ModA can be explained by the presence of *F*-phase and the reduced solubility in γ'' precipitates, which lead to the inhomogeneous distribution of elements and the uncertainty in IFE analysis. For Ni, slight deviations in the predictions are observed, which are the summed up deviations of the solutes. This is because Ni is the matrix element and is only implicitly included in the simulations.

Other, more general reasons for the observed deviations between measured IFE through APT and computed IFE should also be noted:

- One reason is related to the approximations done in the IFE calculations, which neglected concentration and temperature dependencies of the segregation energies obtained in the DFT calculations and presumed that the system has reached thermodynamic equilibrium after the given annealing time at a given temperature. Our earlier results as well as selected former DFT calculations of solute segregation in binary concentrated alloys with various GB coverage indicate that the computational setup selected for this study is accurate enough to produce segregation energy values in high alloyed systems within reasonable accuracy (of about 10% for the matrix composition of 725 alloy) [3–5,54]. We estimate the computational error associated with neglecting the vibrational contribution to the segregation energy at 620°C to a maximum of 15% of the corresponding segregation energy value calculated at 0K [55]. We have also performed an additional set of kinetic segregation calculations to ensure that the segregation state has reached thermal equilibrium at 620°C after 8 h of heat treatment (see Section 2.1 and for model details Refs. [11,47]). These calculations have shown that the IFE values at the thermal equilibrium condition reproduce the results of the kinetic simulation within ± 3 atoms/nm² in all considered alloys, meaning that

the system is practically at thermodynamic equilibrium after the heat treatment. Omitting solute-solute interactions in the used multi-site McLean model is another important simplification that makes this type of calculations possible, but that has to be treated with caution as it cannot be applied in general to all segregating solutes. In our case, we focus on segregation of B and Mo atoms. These have relatively large absolute values of E_{seg} and, in accordance with other first principles calculations [5,54,56,57], we expect that the interaction energies with other solutes are small relative to the segregation energy. On the other hand, there are exceptions to this rule, like S in Ni [17], where this simplification does not hold true and in which case an explicit treatment of solute-solute interaction in a spirit of Guttman or Fowler isotherms is required to achieve accurate segregation predictions [8].

- Another reason is related to the differences between the underlying GB structure in the experiment and in the calculation. The segregation energies have been computed for a special CSL GB, i.e. the $\Sigma 5(012)[100]$ GB, whereas the exact GBs structure has not been fully identified in the experiment and only the misorientation GB angle has been measured. Nevertheless, all experimentally investigated GBs in this study had a misorientation between 38 and 48°, and thus are also ranked among high angle GBs. Obviously, differences in the misorientation angle go along with changes in the atomic structure, but since they were randomly chosen, they are considered as representative. Since the absolute value of the segregation energy typically scales with the GB energy [3] and since the modelled GB belongs to the class of high angle GBs, we believe that the GB structure-related deviations between calculated and measured IFE are minor, though a special care should be given to this problem in the general case.
- APT is an evaluation method on an extremely local scale and, therefore, gives location-specific results. A volume of several hundreds of nm³ is assumed to be representative for a group of GBs. However, the atomic arrangement can change even for the same GB. Since the preparation of atom probe tips is so cumbersome,

one can only take precautions during selection of the interfaces to test similar GBs, as was done in this study.

Careful consideration of the above-mentioned points is a necessary condition for an accurate quantitative comparison between APT experimental and DFT-based computational results. In summary, if one takes into account possible reasons for the deviation between the DFT and the APT results, the extraordinary agreement between the theory and experiment can be achieved.

5. Conclusion

Segregation of alloying elements to GBs in three modifications of a 725 Ni-base alloy was investigated. The experimentally investigated GBs had misorientations between 38 and 48° and the grain orientations were near to [1 1 1] and [1 0 1] in all cases. The APT measurements revealed formation of nanoscale Ti- and Nb-rich γ'' precipitates throughout the material, as well as a GB decoration with F-phase within the non-modified 725 alloy. Two modifications of the 725 alloy with B and with Cu addition exhibited a similar distribution of the Ti- and Nb-rich γ'' precipitates, though no intermetallic phase has been observed along these GBs. The analysis of the element-specific concentration profiles across the GBs has revealed strong segregation of B and pronounced segregation of Mo. Weak segregation of C, O, P, and Si was detected at the GBs.

The DFT-based predictive segregation model has supported the IFE data obtained from the APT analysis. The results of both approaches have been found to be in good quantitative agreement with each other showing GB segregation of B, Mo, C, O, and P and depletion for Fe, Co, and Cu. A combination of the APT segregation data analysis with predictive model results has allowed us to improve the accuracy of experimental data interpretation and differentiate between atoms primarily involved in formation of precipitates and those that segregate to GBs in the atomic form. Of all studied solutes, Mo and B show the most pronounced enrichment tendencies at the GB and consequently have the potential to replace other undesirable solutes from the interface.

Acknowledgements

The authors gratefully acknowledge the financial support under the scope of the COMET program within the K2 Center “Integrated Computational Material, Process and Product Engineering (IC-MPPE)” (Project No 859480). This program is supported by the Austrian Federal Ministries for Climate Action, Environment, Energy, Mobility, Innovation and Technology (BMK) and for Digital and Economic Affairs (BMDW), represented by the Austrian research funding association (FFG), and the federal states of Styria, Upper Austria and Tyrol. The computational results presented have been achieved using the Vienna Scientific Cluster (VSC).

References

- [1] D. Raabe, M. Herbig, S. Sandlöbes, Y. Li, D. Tytko, M. Kuzmina, D. Ponge, P.-P. Choi, Grain boundary segregation engineering in metallic alloys: A pathway to the design of interfaces, *Current Opinion in Solid State and Materials Science* 18 (2014) 253–261.
- [2] K. Leitner, D. Scheiber, S. Jakob, S. Primig, H. Clemens, E. Povoden-Karadeniz, L. Romaner, How grain boundary chemistry controls the fracture mode of molybdenum, *Materials & Design* 142 (2018) 36–43.
- [3] D. Scheiber, V.I. Razumovskiy, P. Puschnig, R. Pippan, L. Romaner, Ab initio description of segregation and cohesion of grain boundaries in W-25 at.% Re alloys, *Acta Materialia* 88 (2015) 180–189.
- [4] V.I. Razumovskiy, S.V. Divinski, L. Romaner, Solute segregation in Cu: DFT vs. Experiment, *Acta Materialia* 147 (2018) 122–132.
- [5] T. Hajilou, I. Taji, F. Christien, S. He, D. Scheiber, W. Ecker, R. Pippan, V.I. Razumovskiy, A. Barnoush, Hydrogen-enhanced intergranular failure of sulfur-doped nickel grain boundary: In situ electrochemical micro-cantilever bending vs. DFT, *Materials Science and Engineering A* 794 (2020) 139967.
- [6] M.P. Moody, A.V. Ceguerra, A.J. Breen, X.Y. Cui, B. Gault, L.T. Stephenson, R.K.W. Marceau, R.C. Powles, S.P. Ringer, Atomically resolved tomography to directly inform simulations for structure–property relationships, *Nature communications* 5 (2014) 5501.
- [7] P. Lejcek, *Grain Boundary Segregation in Metals*, Springer, Berlin, Heidelberg, 2010.
- [8] P. Lejček, M. Šob, V. Paidar, Interfacial segregation and grain boundary embrittlement: An overview and critical assessment of experimental data and calculated results, *Progress in Materials Science* 87 (2017) 83–139.
- [9] X.-Y. Cui, S.P. Ringer, On the nexus between atom probe microscopy and density functional theory simulations, *Materials characterization* 146 (2018) 347–358.
- [10] D. McLean, *Grain Boundaries in Metals*, Clarendon Press, Oxford, 1957.

- [11] D. Scheiber, L. Romaner, F.D. Fischer, J. Svoboda, Kinetics of grain boundary segregation in multicomponent systems-The example of a Mo-CBO system, *Scripta Materialia* 150 (2018) 110–114.
- [12] J.R. Rice, J.-S. Wang, Embrittlement of interfaces by solute segregation, *Materials Science and Engineering A* 107 (1989) 23–40.
- [13] M. Yamaguchi, M. Shiga, H. Kaburaki, Energetics of segregation and embrittling potency for non-transition elements in the Ni 5 (012) symmetrical tilt grain boundary: a first-principles study, *Journal of Physics: Condensed Matter* 16 (2004) 3933–3956.
- [14] X. Wu, Y.W. You, X.S. Kong, J.L. Chen, G.N. Luo, G.H. Lu, C.S. Liu, Z. Wang, First-principles determination of grain boundary strengthening in tungsten: Dependence on grain boundary structure and metallic radius of solute, *Acta Materialia* 120 (2016) 315–326.
- [15] V.I. Razumovskiy, A.V. Ruban, I.M. Razumovskii, A.Y. Lozovoi, V.N. Butrim, Y.K. Vekilov, The effect of alloying elements on grain boundary and bulk cohesion in aluminum alloys: An ab initio study, *Scripta Materialia* 65 (2011) 926–929.
- [16] A.Y. Lozovoi, A.T. Paxton, M.W. Finnis, Structural and chemical embrittlement of grain boundaries by impurities: a general theory and first-principles calculations for copper, *Physical review B* 74 (2006) 155416.
- [17] V.I. Razumovskiy, A.Y. Lozovoi, I.M. Razumovskii, First-principles-aided design of a new Ni-base superalloy: Influence of transition metal alloying elements on grain boundary and bulk cohesion, *Acta Mater* 82 (2015) 369–377.
- [18] V.I. Razumovskiy, D. Scheiber, I.M. Razumovskii, V.N. Butrim, A.S. Trushnikova, S.B. Varlamova, Beresnev, AG, New Cr-Ni-base alloy for high-temperature applications designed on the basis of first principles calculations, *Advances in Condensed Matter Physics* 2018 (2018).
- [19] R. Mahjoub, D.A. Basha, A. Singh, M. Ferry, N. Stanford, The contrasting fracture behaviour of twin boundaries and general boundaries – A first principles study based on experimental observation, *Materials Science and Engineering: A* 781 (2020) 139225.
- [20] D. Scheiber, Segregation and embrittlement of gold grain boundaries, *Computational Materials Science* 187 (2021) 110110.
- [21] L. Huber, J. Rottler, M. Militzer, Atomistic simulations of the interaction of alloying elements with grain boundaries in Mg, *Acta Mater* 80 (2014) 194–204.
- [22] A.S. Kholobina, R. Pippan, L. Romaner, D. Scheiber, W. Ecker, V.I. Razumovskiy, Hydrogen Trapping in bcc Iron, *Materials (Basel, Switzerland)* 13 (2020).
- [23] D. Lemarchand, E. Cadel, S. Chambrelan, D. Blavette, Investigation of grain-boundary structure-segregation relationship in an N18 nickel-based superalloy, *Philosophical Magazine A* 82 (2002) 1651–1669.
- [24] D. Blavette, P. Duval, L. Letellier, M. Guttman, Atomic-scale APFIM and TEM investigation of grain boundary microchemistry in Astroloy nickel base superalloys, *Acta Mater.* 44 (1996) 4995–5005.

- [25] E. Cadel, D. Lemarchand, S. Chambreland, D. Blavette, Atom probe tomography investigation of the microstructure of superalloys N18, *Acta Mater.* 50 (2002) 957–966.
- [26] M. Thuvander, H.-O. Andrén, A PFIM Studies of Grain and Phase Boundaries, *Materials characterization* 44 (2000) 87–100.
- [27] O.C. Hellman, D.N. Seidman, Measurement of the Gibbsian interfacial excess of solute at an interface of arbitrary geometry using three-dimensional atomprobe microscopy, *Materials Science and Engineering A* 327 (2002) 24–28.
- [28] B.M. Jenkins, F. Danoix, M. Gouné, P.A.J. Bagot, Z. Peng, M.P. Moody, B. Gault, Reflections on the Analysis of Interfaces and Grain Boundaries by Atom Probe Tomography, *Microscopy and Microanalysis* (2020) 1–11.
- [29] K. Babinsky, W. Knabl, A. Lorich, R. de Kloe, H. Clemens, S. Primig, Grain boundary study of technically pure molybdenum by combining APT and TKD, *Ultramicroscopy* 159 Pt 2 (2015) 445–451.
- [30] B.M. Jenkins, J.O. Douglas, H.M. Gardner, D. Tweddle, A. Kareer, P.S. Karamched, N. Riddle, J.M. Hyde, P.A. Bagot, G.R. Odette, M.P. Moody, A more holistic characterisation of internal interfaces in a variety of materials via complementary use of transmission Kikuchi diffraction and Atom probe tomography, *Applied Surface Science* 528 (2020) 147011.
- [31] S. Sulzer, M. Hasselqvist, H. Murakami, P. Bagot, M. Moody, R. Reed, The Effects of Chemistry Variations in New Nickel-Based Superalloys for Industrial Gas Turbine Applications, *Metallurgical and Materials Transactions A* 51 (2020) 4902–4921.
- [32] X. Lu, Y. Ma, D. Wang, On the hydrogen embrittlement behavior of nickel-based alloys: Alloys 718 and 725, *Materials Science and Engineering A* 792 (2020) 139785.
- [33] M.C. Chaturvedi, Y. Han, Strengthening mechanisms in Inconel 718 superalloy, *Metal Science* 17 (1983) 145–149.
- [34] P.J. Felfer, T. Alam, S.P. Ringer, J.M. Cairney, A reproducible method for damage-free site-specific preparation of atom probe tips from interfaces, *Microscopy research and technique* 75 (2012) 484–491.
- [35] M.K. Miller, K.F. Russell, Atom probe specimen preparation with a dual beam SEM/FIB miller, *Ultramicroscopy* 107 (2007) 761–766.
- [36] M.K. Miller, R.G. Forbes, *Atom-Probe Tomography: The Local Electrode Atom Probe*, Springer US, Boston, MA and s.l., 2014.
- [37] K. Babinsky, R. de Kloe, H. Clemens, S. Primig, A novel approach for site-specific atom probe specimen preparation by focused ion beam and transmission electron backscatter diffraction, *Ultramicroscopy* 144 (2014) 9–18.
- [38] P. Maugis, K. Hoummada, A methodology for the measurement of the interfacial excess of solute at a grain boundary, *Scripta Mater.* 120 (2016) 90–93.
- [39] B. Gault, M.P. Moody, J.M. Cairney, S.P. Ringer, *Atom probe microscopy*, Springer, New York, NY, 2012.
- [40] P.E. Blöchl, Projector augmented-wave method, *Phys. Rev. B* 50 (1994) 17953.

- [41] G. Kresse, D. Joubert, From ultrasoft pseudopotentials to the projector augmented-wave method, *Phys. Rev. B* 59 (1999) 1758.
- [42] G. Kresse, J. Hafner, Ab initio molecular dynamics for open-shell transition metals, *Phys. Rev. B* 48 (1993) 13115–13118.
- [43] G. Kresse, J. Furthmüller, Efficiency of ab-initio total energy calculations for metals and semiconductors using a plane-wave basis set, *Computational Materials Science* 6 (1996) 15–50.
- [44] J.P. Perdew, K. Burke, M. Ernzerhof, Generalized Gradient Approximation Made Simple, *Phys. Rev. Lett.* 77 (1996) 3865–3868.
- [45] H.J. Monkhorst, J.D. Pack, Special points for Brillouin-zone integrations, *Phys. Rev. B* 13 (1976) 5188–5192.
- [46] S. He, W. Ecker, R. Pippan, V.I. Razumovskiy, Hydrogen-enhanced decohesion mechanism of the special Σ_5 (0 1 2)[1 0 0] grain boundary in Ni with Mo and C solutes, *Computational Materials Science* 167 (2019) 100–110.
- [47] D. Scheiber, T. Jechtl, J. Svoboda, F.D. Fischer, L. Romaner, On solute depletion zones along grain boundaries during segregation, *Acta Mater* (2020).
- [48] M.S. Hazarabedian, M.Z. Quadir, M. Iannuzzi, Characterization of intergranular phases in precipitation hardening Ni alloy UNS N07725, *Materials characterization* 171 (2021) 110770.
- [49] H. Gardner, S. Pedrazzini, J.O. Douglas, D. de Lille, M.P. Moody, P.A.J. Bagot, Atom Probe Tomography Investigations of Microstructural Evolution in an Aged Nickel Superalloy for Exhaust Applications, *Metallurgical and Materials Transactions A* 50 (2019) 1862–1872.
- [50] R. Lawitzki, S. Hassan, L. Karge, J. Wagner, D. Wang, J. von Kobylinski, C. Krempaszky, M. Hofmann, R. Gilles, G. Schmitz, Differentiation of γ' - and γ'' - precipitates in Inconel 718 by a complementary study with small-angle neutron scattering and analytical microscopy, *Acta Materialia* 163 (2019) 28–39.
- [51] R. Cozar, A. Pineau, Morphology of γ' and γ'' precipitates and thermal stability of inconel 718 type alloys, *MTA 4* (1973) 47–59.
- [52] A. Drexler, B. Oberwinkler, S. Primig, C. Turk, E. Povoden-Karadeniz, A. Heinemann, W. Ecker, M. Stockinger, Experimental and numerical investigations of the γ'' and γ' precipitation kinetics in Alloy 718, *Materials Science and Engineering A* 723 (2018) 314–323.
- [53] P.M. Mignanelli, N.G. Jones, E.J. Pickering, O.M.D.M. Messé, C.M.F. Rae, M.C. Hardy, H.J. Stone, Gamma-gamma prime-gamma double prime dual-superlattice superalloys, *Scripta Mater.* 136 (2017) 136–140.
- [54] D. Scheiber, L. Romaner, R. Pippan, P. Puschnig, Impact of solute-solute interactions on grain boundary segregation and cohesion in molybdenum, *Phys. Rev. Materials* 2 (2018) 93609.
- [55] D. Scheiber, O. Renk, M. Popov, L. Romaner, Temperature dependence of surface and grain boundary energies from first principles, *Phys. Rev. B* 101 (2020).

- [56] D. Aksyonov, T. Hickel, J. Neugebauer, Lipnitskii, AG, The impact of carbon and oxygen in alpha-titanium: ab initio study of solution enthalpies and grain boundary segregation, *Journal of Physics: Condensed Matter* 28 (2016) 385001.
- [57] D. Scheiber, K. Prabitz, L. Romaner, W. Ecker, The influence of alloying on Zn liquid metal embrittlement in steels, *Acta Materialia* (2020).